DTIC FILE COPY

(1)

AD-A217 068

Numerical Simulation of Acoustic Scatter from Subsurface Bubble Clouds

by
Charles L. Rino and Hoc D. Ngo

Technical Report

Vista Project No. 1010

Prepared for:

Defense Advanced Research Projects Agency
1400 Wilson Boulevard
Arlington, Virginia 22209

DTIC
ELECTE
JAN 22 1990
S B D

Contract No. N00014-87-C-0473 – ONR
A04462
Attention: Dr. Alan Ellinthorpe

October 18, 1989

VISTA RESEARCH, INC.
100 View Street • P.O. Box 998
Mountain View, CA 94042 • (415) 966-1171

DISTRIBUTION STATEMENT A
Approved for public release;
Distribution Unlimited

~~89 10 27 082~~

REPORT DOCUMENTATION PAGE

Form Approved
OMB No. 0704-0188

Public reporting burden for this collection of information is estimated to average 1 hour per response, including the time for reviewing instructions, searching existing data sources, gathering and maintaining the data needed, and completing and reviewing the collection of information. Send comments regarding this burden estimate or any other aspect of this collection of information, including suggestions for reducing this burden, to Washington Headquarters Services, Directorate for Information Operations and Reports, 1215 Jefferson Davis Highway, Suite 1204, Arlington, VA 22202-4302, and to the Office of Management and Budget, Paperwork Reduction Project (0704-0188), Washington, DC 20503.

1. AGENCY USE ONLY *(Leave blank)*

2. REPORT DATE
Oct. 18, 1989

3. REPORT TYPE AND DATES COVERED
Technical
June 15 - October 31, 1989

4. TITLE AND SUBTITLE
Numerical Simulation of Acoustic Scatter from Subsurface Bubble Clouds

5. FUNDING NUMBERS

6. AUTHOR(S)
Charles L. Rino and Hoc D. Ngo

7. PERFORMING ORGANIZATION NAME(S) AND ADDRESS(ES)
Vista Research, Inc.
100 View St., P.O. Box 998
Mountain View, CA 94042

8. PERFORMING ORGANIZATION REPORT NUMBER

9. SPONSORING/MONITORING AGENCY NAME(S) AND ADDRESS(ES)
Defense Research Projects Agency
1400 Wilson Blvd.
Arlington, VA 22209

10. SPONSORING/MONITORING AGENCY REPORT NUMBER

11. SUPPLEMENTARY NOTES

12a. DISTRIBUTION/AVAILABILITY STATEMENT
Approved for Public Release
Distribution Unlimited

12b. DISTRIBUTION CODE

13. ABSTRACT *(Maximum 200 words)*

A new technique is described that allows computation of the scattering characteristics of an object near a rough surface in terms of the free-space scattering characteristics of the rough surface and the scattering object. The method is applied to the problem of acoustic scatter from a small bubble cloud below the ocean surface. The results show that under most conditions of interest the backscatter from the bubble cloud is enhanced over its free-space level. The ramifications for acoustic reverberation noise are discussed.

14. SUBJECT TERMS
Acoustics, numerical simulation, rough surface scatter,

15. NUMBER OF PAGES
77

16. PRICE CODE

17. SECURITY CLASSIFICATION OF REPORT	18. SECURITY CLASSIFICATION OF THIS PAGE	19. SECURITY CLASSIFICATION OF ABSTRACT	20. LIMITATION OF ABSTRACT
Unclassified	Unclassified	Unclassified	

NSN 7540-01-280-5500

Standard Form 298 (Rev. 2-89)
Prescribed by ANSI Std. Z39-18
298-102

90 01 22 002

Executive Summary

This report describes the results of applying a new numerical simulation technique to the problem of scattering from subsurface bubble clouds generated by spilling or breaking waves. To the extent that these bubble clouds can be modeled by homogeneous voids or weakly permeable objects, the scattering characteristics are amenable to exact analysis by our method. The results extend previous work in which we developed numerical simulation techniques to compute detailed scattering characteristics of ocean-surface realizations that preserve the essential hydrodynamic nonlinearities. It is known that at high sea states the measured surface reverberation noise cannot be explained by surface scatter alone, and subsurface bubble clouds have been hypothesized as the source of the enhanced backscatter. In its simplest form, the model invokes a meter-sized impermeable object, which can have a low-frequency acoustic backscatter cross section that is more than 30 dB higher than the corresponding surface backscatter level at high sea states. The proximity of the highly irregular surface that spawned the bubble cloud, however, can significantly alter the scattering characteristics of the bubble in isolation.

The bubble scattering problem is solved herein as a special case of a more general formulation we developed for calculating the multiple scattering from a collection of objects whose free-space scattering characteristics are known. Each scatterer is confined to a region bounded by a pair of planes over which the total scattered fields are characterized by their spatial two-dimensional Fourier spectra. At each boundary plane these wave fields see only the two adjacent scatterers. If there are only two scatterers, the interaction equations for the coupled Fourier modes can be solved as a system of linear equations. The technique is sufficiently general that one of the particles can be replaced by a plane or rough surface. Thus, the mutual interaction between an object and a rough surface can be solved in terms of the known scattering functions for the surface and the particle. For the ocean surface, we use our previously developed numerical method to calculate the surface scattering function. At the present time, the bubble cloud is modeled by a simple geometrical shape whose scattering characteristics are known. More refined bubble scattering models can be incorporated as they are developed.

Our simulations are presently restricted to two dimensions. This constraint comes mainly from the need to characterize ocean surface scatter at high sea states. No currently available computational method gives the two-dimensional surface scattering function with sufficient accuracy to perform the mutual-interaction computations. However, both cylinders and spheres near plane impenetrable surfaces can be solved by the mutual-interaction method. Indeed, for small objects that scatter isotropically, the mutual-interaction equations admit algebraic solutions. We find that as a small scattering object is moved away from a plane impenetrable surface, the backscatter coefficient,

n For
\&I
:ed
:tion
Distribution/
Availability Codes
Dist | Avail and/or Special
A-1
DTIC COPY INSPECTED 1

which is initially suppressed to the surface backscatter value if the roughness is small, increases very rapidly to its free-space value and then exceeds that value by at least 12 dB before it peaks. Thus, a small object in close proximity to an impenetrable surface can display very rapid changes in its overall scatter coefficient, and large enhancements over the free backscatter coefficient can be achieved. The backscatter enhancement is generally maximized for isotropic scatterers. The exact solutions for meter-sized objects show peak enhancements 2 to 7 dB lower than the isotropic value depending on the incidence angle.

While the plane surface and/or isotropic results are useful for illustrating some key features of the scattering interaction, they do not admit a direct dependence on sea-state. Acoustic scatter data show that the onset of anomalous surface backscatter occurs at a wind speed of approximately 20 knots. Our simulations show that at 20 knots the scattering characteristics are qualitatively similar to those of a plane reflecting surface, but at the depth of the deepest wave trough the 60° backscatter enhancement is already near its peak level. At 30 knots there are significant differences between the flat and rough-surface models, but the lobing pattern with increasing distance persists. As the wind speed is increased further, the characteristic interference patterns may disappear altogether. In all cases, however, at high sea states (at or above 15 knots), the presence of a meter-sized void acts to substantially enhance the low-frequency acoustic surface reverberation noise at the level of the the deepest wave trough.

The mutual interaction method presently does not allow the bubble cloud and the surface to overlap. Thus, the bubble cloud must be at or below the depth of the deepest trough in the surface realization. Somewhat fortuitously, this feature provides a qualitative explanation of the wind-speed dependence of the Chapman-Harris curves. The bubble backscatter coefficient at a distance corresponding to the deepest wave trough has the correct incidence-angle dependence, but it rises too steeply for a fixed bubble size independent of wind speed. The present bubble model does not include dynamic or wind-speed dependent characteristics. Thus, we have not computed the Doppler spectrum because the static model will automatically concentrate the excess backscattered intensity near zero Doppler shift. It is more appropriate to perform the more expensive Doppler computations when bubble dynamics can be included.

The main purpose of this report is to provide a thorough exposé of the mutual-interaction method. The preliminary results do not yet establish all the details of the backscatter enhancement caused by subsurface bubble clouds, but the missing features can be incorporated as the bubble-cloud dynamics and wind-speed dependence are better understood. The rationale for the bubble model is reviewed in Section I. Section II presents some background material, including cross section definitions. In Section III.1 the theory is developed in its most general vector form and then specialized to the scalar problem of interest here. Because the scattering interactions are exact, it is necessary

to accommodate evanescent waves. Analytic continuation is used to extend the usual definition of the scattering functions, but the necessary results, which are not readily available in papers or text books, are developed in the appendix. The formulation that is used for numerical computation is summarized in Section III.2. Illustrative examples are presented in Section III.3, where two-cylinder results are compared to computations performed with full method of moments. Comparisons are also made with analytic formulas valid for isotropic scatterers.

Our preliminary results for ocean surfaces are presented in Section IV. Conclusions and recommendations are presented in Section V. An overview of the report can be obtained by reading Sections I and V.

Contents

I Introduction 1

II Background 5

III The Mutual Interaction Method 8

III.1 Theory 8

III.2 Numerical Simulations 15

III.3 Examples 22

IV Scattering from Near-Surface Bubble Clouds 35

V Conclusions and Recommendations 56

Appendix

The Scattering Function of a Single Scatterer 59

References 76

List of Figures

1 Comparison of first-order perturbation theory with 130-Hz acoustic backscatter data. 2

2 Geometry for two-object computation with definition of symbols. 10

3 Magnitude of the scattering function of an infinitely long cylinder 15 m in diameter illuminated by an axially polarized 7.5-m wavelength wave incident along the z axis for two cases: (a) perfect conductor, (b) dielectric with refractive index of 1.5. 17

4 Magnitude of the scattering function of an infinitely long cylinder 15 m in diameter illuminated by an axially polarized 7.5-m wavelength wave incident along the z axis for two cases: (a) perfect conductor, (b) dielectric with refractive index of 1.5. 18

5 Backscatter conversion factor σ_0/γ_0 for $\lambda = 7.5$ m as a function of incidence angle for different values of the normalized beamwidth parameter k_w/k. 21

6 Differential scatter coefficient for (a) a single cylinder and (b) two identical cylinders separated by 5 m. 23

7 Backscatter cross section for two identical cylinders as a function of their separation ΔL. 24

8 Comparison of NEC and MIM calculations for a wave incident along the axis of the cylinders. 25

9 Comparison of NEC and MIM calculations for a wave incident broadside to the axis of the cylinders. 26

10 Differential scatter coefficient for a cylinder and a flat surface for three values of the distance ΔL (4, 5, and 6 m). 27

11 Differential scatter coefficient for a cylinder and a flat surface for three values of the incidence angle θ_i (60°, 70°, and 80°). 28

12 Backscatter cross section for cylinder near plane as a function of distance ΔL at 60° incidence. 30

13 Backscatter cross section for cylinder near plane as a function of distance ΔL at 70° incidence. 31

14 Backscatter cross section for cylinder near plane as a function of distance ΔL at 80° incidence. 32

15 (*a*) A realization of a zero-mean one-dimensional linear ocean surface. (*b*) Differential scatter coefficient (1) for this surface alone, (2) for a PC cylinder 5 m below this surface, and (3) for a PC cylinder 5 m below a planar surface. 34

16 Differential scattering coefficients for $U = 10$ m/s at 60° incidence. 38

17 Backscatter cross section as a function of distance for $U = 10$ m/s at 60° incidence. 39

18 Differential scattering coefficients for $U = 10$ m/s at 70° incidence. 40

19 Backscatter cross section as a function of distance for $U = 10$ m/s at 70° incidence. 41

20 Differential scattering coefficients for $U = 10$ m/s at 80° incidence. 42

21 Backscatter cross section as a function of distance for $U = 10$ m/s at 80° incidence. 43

22 Differential scattering coefficients for $U = 15$ m/s at 60° incidence. 44

23 Backscatter cross section as a function of distance for $U = 15$ m/s at 60° incidence. 45

24 Differential scattering coefficients for $U = 15$ m/s at 70° incidence. 46

25 Backscatter cross section as a function of distance for $U = 15$ m/s at 70° incidence. 47

26 Differential scattering coefficients for $U = 15$ m/s at 80° incidence. 48

27 Backscatter cross section as a function of distance for $U = 15$ m/s at 80° incidence. 49

28 Differential scattering coefficients for $U = 20$ m/s at 60° incidence. 50

29 Backscatter cross section as a function of distance for $U = 20$ m/s at 60° incidence. 51

30 Backscatter cross section as a function of distance for $U = 20$ m/s at 70° incidence. 53

31 Differential scattering coefficients for $U = 20$ m/s at 80° incidence. 54

32 Backscatter cross section as a function of distance for $U = 20$ m/s at 80° incidence. 55

33 Comparison of Chapman-Harris curves (solid) with wind-independent cloud model (dotted). 57

I Introduction

In a previous report [1] we described numerical simulations of acoustic and electromagnetic (EM) scatter from evolving nonlinear ocean-surface realizations. The work was undertaken to verify and extend theories that attempt to explain acoustic scatter from ocean surfaces. Of particular interest is an anomalous enhanced backscatter component observed at high sea states. Because ocean surfaces comprise a power-law continuum of spatial wave number components, neither the small perturbation theory of rough surfaces nor the Kirchoff approximation can be used to predict the characteristics of scattered wave fields. The two-scale model for rough-surface scattering effectively combines these two approximations; however, it is not entirely satisfactory because the two-scale partitioning and the subsequent analysis of the scattering regimes are ad hoc. More recent theoretical work based on higher-order perturbation theory [2] and a T-matrix approach [3] has largely removed the immediate problems with the two-scale model, and a well-founded theory has emerged that is applicable to the wavelengths and sea states relevant to the anomalous acoustic backscatter phenomenon. In principle, the new theory can accommodate nonlinear hydrodynamics and will ultimately yield average Doppler spectra, but this has not yet been achieved.

Our previous work demonstrated that practical schemes exist for generating surface realizations that accommodate the dominant nonlinear surface hydrodynamics. Numerical simulations that use these realizations as inputs are effectively computer experiments, whereby any characteristic of the scattered signal, such as its Doppler spectrum, is readily computed. At the present time, however, computation and storage requirements restrict the diffraction computations to two dimensions. That is, the surface height can vary in only one direction. This restricts the fidelity of the surface hydrodynamic and scattering phenomena that can be modeled, but the two-dimensional simulations can be used effectively to test hypotheses and to guide experiment planning. Thus, to generate timely intermediate results, we have extended our two-dimensional simulations to accommodate near-surface bubble clouds, which have been hypothesized to explain the anomalous acoustic backscatter.

From first-order perturbation theory, it follows that the acoustic surface backscatter level is proportional to the spatial wave number spectrum of the surface-height fluctuations evaluated at the Bragg wave number, which is given as $k_b = 2k \sin\theta_i$, where $k = 2\pi/\lambda$, λ is the wavelength of the acoustic signal, and θ_i is the incidence angle. For a simple spectral model, for example, the Phillips and Moskowitz spectrum discussed in Section IV of [1], the Bragg level saturates at a threshold wind speed. The more detailed scatter calculations predict a nearly linear increase in the logarithm of the backscatter cross section with wind speed. The excess backscatter over the Bragg level is attributed to large-scale tilts upon which the *Bragg carpet* lies. Ocean-surface scatter measured

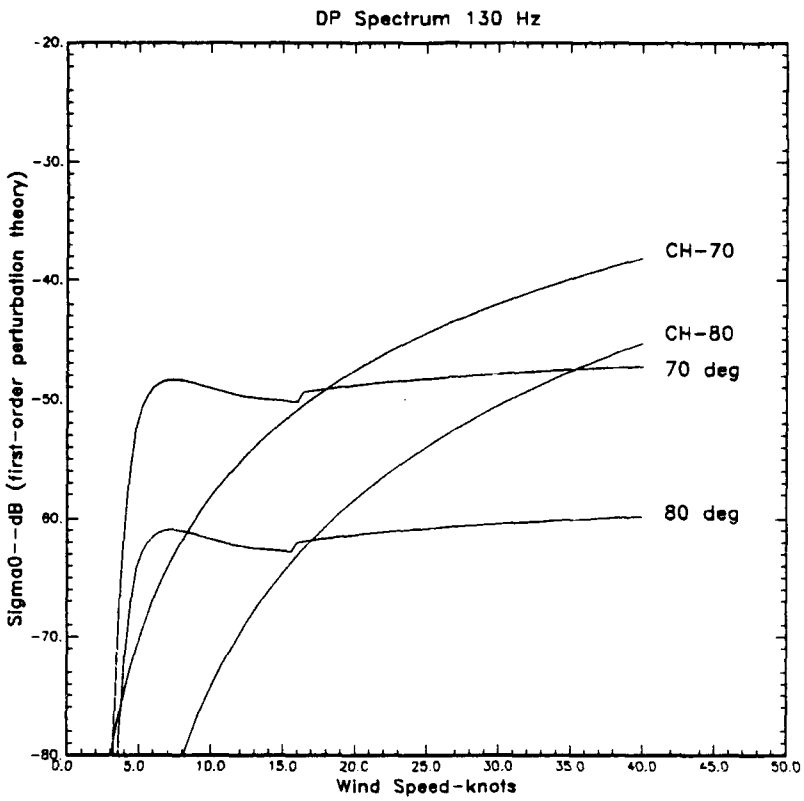

Figure 1: Comparison of first-order perturbation theory with 130-Hz acoustic backscatter data.

with microwave radars is generally in agreement with these predictions, but at high wind speeds the acoustic backscatter cross section increases more nearly as the fourth power of wind speed. When this anomalous backscatter occurs, the Doppler spectra show a pronounced enhancement near zero Doppler shift.

Figure 1 shows the 130-Hz Bragg acoustic backscatter level at 70° and 80° incidence angles as predicted by first-order perturbation theory with the Donelan-Pierson spectral model for an upwind propagation direction. The two curves marked CH-70 and CH-80 are derived from analytic approximations to the Chapman-Harris curves [4], which are commonly used to estimate the acoustic surface reverberation noise. As noted above, more detailed calculations give higher surface backscatter levels, but for winds above approximately 20 knots, surface roughness alone cannot account for the observed scatter levels. Because of the wind-speed dependence, it has been hypothesized that the anomalous backscatter is caused by subsurface bubble clouds generated by breaking or spilling waves.

The support for this hypothesis has been summarized by Ellinthorpe [5]. From laboratory measurements by Baldy [6], we know that breaking waves generate clouds of small bubbles in which the largest-size constituents extend to a depth of approximately one half the rms wave height of the breaking waves. Below this depth there is a sharp cutoff, and only very small bubbles survive. If we use significant wave height as deduced from the Pierson-Neumann theory in place of the rms wave height, the cloud of larger bubbles extends to the depth

$$d_{\max} \approx 1.5 \times 10^{-2} U^2, \tag{1}$$

where U is the wind speed in meters per second (cf. Chapter 8.3 of Kinsman [7]). Baldy also observed that the bubbles tend to occur in clusters or clouds at one per dominant wave period, with a definite position relative to the wave phase. If we use the peak of the Pierson-Moskowitz spectrum as a measure of the dominant wavelength, the bubble clouds should have a lateral dimension bounded by

$$l_{\max} \leq U^2/(10g), \tag{2}$$

where g is the acceleration due to gravity. From 119-kHz surface acoustic backscatter measurements in deep ocean, Crawford and Farmer [8] deduced plume-like clouds of bubbles that support the general features of Baldy's laboratory measurements.

The structure and dynamics of subsurface bubble clouds are poorly understood, but we can deduce likely scattering characteristics. In a sparse distribution of scatterers, the coherent wave field propagates with the *effective* wave number

$$k_{\text{eff}} \approx k + \frac{2\pi}{k} <f(\mathbf{a}_i, \mathbf{a}_i)> , \tag{3}$$

where $f(\mathbf{a}_s, \mathbf{a}_i)$ is the complex scattering function for the particle, and the angle brackets denote an ensemble average over the particle attributes–mainly size [9]. For a small bubble the scattering is nearly isotropic, and it is shown in [9] that

$$f \approx \frac{-a\omega^2}{\omega^2 - \Omega^2 + i\omega\Gamma}, \tag{4}$$

where a is the bubble radius, ω is the acoustic angular frequency,

$$\Omega = \sqrt{3\rho_a c_a^2/(a\rho_w c_w)} \tag{5}$$

is the corresponding resonant frequency, and Γ is the thermal loss factor. The parameters ρ and c denote density and speed, respectively, with the subscripts indicating the medium (air or water). For low acoustic frequencies the expected bubble radii are such

that $\omega \ll \Omega$, and thermal losses are negligible. Indeed, the scattering losses as inferred from the extinction of the coherent wave field are themselves very small, which indicates that scattering by individual bubbles is not a viable mechanism to account for anomalous scatter.

On the other hand, for frequencies well below Ω, it can be shown from (3), (4), and (5) that the effective sound speed inside the bubble cloud is given by the relation

$$c \approx c_w(1 + 8000VF), \tag{6}$$

where c_w is the speed of sound in water and VF is the void fraction. For void fractions in the expected range $2 \times 10^{-4} \leq VF \leq 2 \times 10^{-3}$, the speed discontinuity at an abrupt boundary can be significant. Thus, to the extent that the bubble clouds have well-defined boundaries, they can be modeled by homogeneous irregularities with an internal sound speed given by (6). One finds that the 200-Hz cross section of a meter-sized object can be ≈ 20 dB higher than the corresponding surface backscatter level at low grazing angles. For example, a 1-m cylindrical void has a 200-Hz backscatter cross section of ~ -30 dB, whereas the surface backscatter level in consistent units (see Section II) is less than -40 dB at grazing angles below 20°. Allowing for finite permeability does not change this picture significantly.

Thus, if one accepts a homogeneous void or a weakly permeable object as a reasonable first approximation to a subsurface bubble cloud, the problem becomes one of determining the scattering characteristics of such an object near an irregular surface. Although highly idealized, this model can identify the most important characteristics of scattering by near-surface scattering objects. It is possible to treat this composite scattering problem by generating multiple surface boundary integrals that enclose each object; however, this approach is inefficient. For example, a method-of-moments (MOM) computation of the mutual interaction between two objects of comparable size requires an eight-fold increase in computation time over that required for a single object. At Vista Research, Inc., we have developed a novel method that allows us to use the known scattering characteristics of the individual scatterers in an exact calculation of the mutual interaction (multiple scattering) between the two objects. The mutual-interaction computation requires less time than the computation of the scattering characteristics of the rough surface itself.

The method is completely general in that it can be used to calculate the mutual interaction between any pair of scattering objects. To validate the method, we have performed scatter calculations for pairs of cylinders, a cylinder near a smooth surface, and a cylinder near a rough surface (Section III.3). In all cases, we observe backscatter enhancements in excess of 12 dB over the isolated backscatter level of the single cylinder as the cylinder is moved away from the second object. The coherent superposition of the backscatter from two identical objects or an object and its image can account for a 6-dB

enhancement, but there is an additional pair of reciprocal backscatter paths involving multiple scatter between the two objects. The enhancement is somewhat larger for a cylinder adjacent to a planar or rough surface. When the cylinder is in contact with a plane, the scatter cross section is reduced well below the isolated backscatter level of the cylinder, as is expected from image theory. Thus, as a particle breaks away from a surface, there is a very steep rise ($\approx$ 30 dB over the rough surface level) in the backscatter cross section.

To the extent that this mechanism is active for bubble clouds generated by breaking or spilling waves, it clearly supports the bubble-cloud hypothesis as an explanation of the observed anomalous acoustic backscatter. The large backscatter enhancement associated with a scattering object near a reflecting surface is not in itself a new result, but there are many ramifications of this phenomenon that have not been thoroughly investigated. The analytical complexity of the problem has been the principal barrier, but the new method we have developed reduces the computational burden to a manageable level.

II Background

A time-honored problem in scattering theory is the computation of the mutual interaction among disjoint scattering bodies. Examples of this type of problem that are important in active acoustics include the interaction of a large transducer array on the ocean bottom and the scatter from near-surface bubble clouds. The problem admits a rigorous formulation in terms of multiple surface integrals over the scattering objects that can be evaluated numerically. This approach, however, makes no use of the known free-space scattering characteristics of the individual scatterers, and the resulting numerical methods are generally inefficient in that the same results can be obtained with less computation even if the scattering characteristics of the individual objects are unknown a priori and must be computed numerically.

Because considerable effort is typically expended to determine the scattering characteristics of complex bodies, it is clearly desirable to use this information when the scattering characteristics are modified by the presence of terrain, water, or other scattering objects. Traditionally, this multiple-scatter problem has been treated by diagram methods, which can give good approximations to the average field moments for random distributions of large numbers of scatterers, but the basic equations are very difficult to evaluate exactly. As a simple illustration of the principle involved, recall that standing acoustic waves in a pipe with discontinuities obey the transmission-line equations as do waves that obey the more general equations of EM theory. One can solve the standing wave problem by summing the multiplicity of reflected waves, but the transmission-line

equations are more efficiently solved directly.

It is not widely recognized that essentially the same method can be applied to waves scattered by multiple objects. The modes on the transmission line are replaced by spatial Fourier modes propagating forward and backward relative to imaginary planes separating the objects, which are themselves replaced by scattering planes. A pair of coupled first-order difference equations that characterize the interaction of the fields crossing the planes can be solved for the multiply-scattered wave fields crossing the reference planes in terms of the wave-wave scattering functions that formally replace the objects. Once these fields are known, the backscattered and/or transmitted waves are easily computed. For a single object pair, the solution is particularly simple. In effect, an equation of about the same complexity as the equations that characterize the individual scatterers must be solved. Because the computation time varies with the cube of the number of unknowns, the direct approach will require $(2N)^3$, whereas solving the mutual-interaction equation requires only N^3 additional computations once the two scattering functions are known. For m independent objects, the computation time varies linearly with m versus $(mN)^3$ for the direct method.

The mutual interaction equations are exact to the extent that we have an exact expression for the wave-wave scattering function for each object. For an incident plane wave with wave normal vector $\mathbf{k}^{\pm}(\mathbf{K}')$, the dyadic scattering function $\underline{\widehat{\mathbf{H}}}_n(\mathbf{k}^{\pm}(\mathbf{K}), \mathbf{k}^{\pm}(\mathbf{K}'))$ characterizes the spectrum of scattered plane-wave components indexed by their wave normal $\mathbf{k}^{\pm}(\mathbf{K})$. The notation emphasizes the fact that each wave vector is constrained to have amplitude $k = 2\pi/\lambda$, where λ is the wavelength in the surrounding medium. Thus, the z component of the wave normal vector is related to the magnitude of the transverse component $\mathbf{K}$ by the relation

$$k_z(K) = \pm\sqrt{k^2 - K^2}. \tag{7}$$

When $K > k$, (7) is purely imaginary, and the corresponding wave is said to be evanescent. These evanescent waves must be properly accommodated in the dyadic scattering function. The method of defining the scattering functions over all wave numbers is developed in the appendix. The numerical simulations themselves, which are described in detail in Section III, yield the two-dimensional Fourier spectrum of the total wave field near the scattering surfaces. The scattered wave field is the difference between the total wave field and the wave field that would exist in the absence of scatterers. The far-zone limit of any propagating wave field is simply related to the two-dimensional Fourier transform of the corresponding wave field evaluated on a plane near the scattering object. Thus, all quantities of importance are readily obtained from the numerical simulations.

It is impractical to perform numerical simulations with incident plane waves for large objects. To minimize truncation errors from edge discontinuities, it is necessary

to use a narrow beam. Let $\mathbf{E}_i(\mathbf{r})$ represent the field of the beam. In our calculations we normalize the beam so that the total integrated far-zone intensity is unity. The normalization factor has the units of length or area. We define the unitless differential scattering coefficients

$$\gamma(\mathbf{k}_s, \mathbf{k}_i) = \begin{cases} r|\mathbf{E}(\mathbf{r})|^2/(L|\mathbf{E}_i|^2) & \text{two-dimensional} \\ r^2|\mathbf{E}(\mathbf{r})|^2/(A|\mathbf{E}_i|^2) & \text{three-dimensional.} \end{cases} \tag{8}$$

Note that $\gamma(\mathbf{k}_s, \mathbf{k}_i)$ is defined in terms of the total wave field and integrates over all solid angles to unity for a lossless scatterer. These definitions are commonly used for surface scatter, although the surface cross-sectional area is often used in place of the cross-sectional area normal to the beam. In [1], we distinguish the differential scattering coefficient γ from the differential scattering cross section by using the notation $\sigma = \gamma \sin\theta_i$, where θ_i is the incidence angle. For particles, however, an unnormalized cross section with units of area or length is defined in terms of the scattered field for an incident plane wave. The standard particle cross section integrates to the total scattered intensity.

The highly dissimilar cross-section measures create a dilemma for data presentation. We have chosen to resolve it by retaining the definition (8) for particles as well as surfaces. In effect, we illuminate the particle with the same finite beam that necessarily illuminates the surface. When presented this way, the particle backscatter coefficient is in units that can be compared directly to the surface scatter coefficient or the cross section per unit area if the scattering coefficient is multiplied by the cosine of the incidence angle. We develop formulas to convert to particle cross-section units in Section III.2, but it should be kept in mind that the ideal plane-wave cross section is a limiting form that can, in a numerical simulation or a real measurement, only be approached.

Finally, we have developed our analysis in its most general form for vector EM fields. The scalar wave fields appropriate to the acoustic scatter problem are easily extracted. Indeed, for pressure release surfaces, the horizontally polarized EM problem and the acoustic problem are mathematically identical, as we showed in Appendix A of [1]. One need only interpret the square root of the relative permittivity as a velocity ratio. The parameters chosen for all our examples were motivated by low-frequency active acoustics. We take the velocity of sound in sea water as 1500 m/s.

III The Mutual Interaction Method

III.1 Theory

In a recent paper [10], we showed that the mutual interaction among many scattering objects can be characterized exactly by a pair of vector wave transport equations. This formulism assumes that the projections of these scatters onto the z axis do not overlap, whereby the medium can be divided into slabs bounded by planes at $z = z_n$ such that the nth object lies entirely within the slab $z_{n-1} \leq z \leq z_n$. Each discrete object is characterized by a dyadic scattering functions $\underline{\widehat{\mathbf{H}}}_n(\mathbf{k}^{\pm}, \mathbf{k}'^{\pm})$, where the first wave normal vector refers to the scattered wave, the second wave normal vector to the incident wave, and the sign to the z direction of propagation for real k_z or attenuation for imaginary k_z. Each object interacts only with the wave fields that enter the slab containing it. The *exact* difference equations for the total wave fields are given by the difference equations

$$\widehat{\mathbf{E}}_n^+ = \widehat{\mathbf{E}}_{n-1}^+ \exp\{ikg(K)L_n\} + \underline{\widehat{\mathbf{H}}}_n^{++} @ \widehat{\mathbf{E}}_{n-1}^+ + \underline{\widehat{\mathbf{H}}}_n^{+-} @ \widehat{\mathbf{E}}_n^-, \tag{9}$$

and

$$\widehat{\mathbf{E}}_{n-1}^- = \widehat{\mathbf{E}}_n^- \exp\{ikg(K)L_n\} + \underline{\widehat{\mathbf{H}}}_n^{--} @ \widehat{\mathbf{E}}_n^- + \underline{\widehat{\mathbf{H}}}_n^{-+} @ \widehat{\mathbf{E}}_{n-1}^+, \tag{10}$$

where $K = |\mathbf{K}|$ is the transverse wave number, $L_n = |z_n - z_{n-1}|$ is the width of the slab containing the nth object,

$$\widehat{\mathbf{E}}_n^{\pm} \equiv \widehat{\mathbf{E}}^{\pm}(\mathbf{K}; z_n), \tag{11}$$

and

$$g(K) = \begin{cases} [1 - K^2/k^2]^{1/2} & \text{for } K \leq k, \\ i[K^2/k^2 - 1]^{1/2} & \text{otherwise.} \end{cases} \tag{12}$$

The dyadic scattering functions that appear in (9) and (10) are the natural product of integral equation computation methods. Formally, they represent the spectra of plane waves scattered by each incident vector plane wave. The operator @ is defined as

$$\begin{aligned} \underline{\widehat{\mathbf{H}}}_n^{u\pm} @ \widehat{\mathbf{E}}_{\substack{n-1\\n}}^{\pm} \equiv\ & \exp\{ikg(K)\ell_n^u\} \iint \frac{d\mathbf{K}'}{(2\pi)^2} \\ & \times \frac{ik \exp\{-i(\mathbf{K} - \mathbf{K}')\cdot\rho_n\}}{2g(K)} \underline{\kappa}^u(\mathbf{K})\cdot\underline{\widehat{\mathbf{H}}}_n^{\circ}(\mathbf{k}^u(\mathbf{K}), \mathbf{k}^{\pm}(\mathbf{K}')) \\ & \cdot \widehat{\mathbf{E}}_{\substack{n-1\\n}}^{\pm}(\mathbf{K}') \exp\{ikg(K')\ell_n^{\mp}\}. \end{aligned} \tag{13}$$

The notation $\widehat{\mathbf{E}}_{\substack{n-1\\n}}^{\pm}$ stands for $\widehat{\mathbf{E}}_{n-1}^+$ or $\widehat{\mathbf{E}}_n^-$, the superscript u stands for $+$ or $-$, $\ell_n^{\pm}$ is the distance from the object to the right $(+)$ or the left $(-)$ bounding plane (see Figure 2), ρ_n is the tranverse position vector of the object, and $\underline{\kappa}^u(\mathbf{K}) = \underline{\mathbf{I}} - k^{-2}\mathbf{k}^u\mathbf{k}^u$ where $\underline{\mathbf{I}}$

is a unit dyadic. The dyadic $\underline{\kappa}$ is a projection function that accounts for the spatial dispersion of the scattered waves. The dyadic $\widehat{\mathbf{H}}_n^o$ is the scattering function of the nth object when it is located at the origin. The factor $\exp\{-i(\mathbf{K} - \mathbf{K}')\cdot\boldsymbol{\rho}_n\}$ accounts for the transverse translation from the origin.

The terms on the right-hand sides of (9) and (10) admit physical interpretations. For example, there are three contributions to the total forward-traveling wave at the plane $z = z_n$. From (9), we see that the first term represents the direct propagation of the forward wave from the plane $z = z_{n-1}$ to $z = z_n$ as though the medium were homogeneous. The second term represents the incremental contribution due to scattering of the forward wave in the forward direction. The last term represents the incremental contribution from the backward wave, which propagates from the plane $z = z_n$ to the object and scatters in the forward direction. A similar interpretation applies to the corresponding terms in (10).

Equation (13) also admits a physical interpretation. The last two factors in the integrand represent the incoming wave as it would be seen at the plane passing through the center of the object if it were to propagate freely from the appropriate boundary plane. The object, now acting only on the field at the center plane, scatters the incoming wave, which produces the incremental scattered waves represented by the dot product between the incoming wave and the scattering function weighted by $ik/2g(K)$. These scattered waves then propagate freely to the slab boundary. The integral operation accounts for the cumulative scattering from all Fourier components of the incoming wave. Thus, in the spectral-domain formulism the scattering objects are effectively replaced by scattering planes. The appendix discusses in detail how to calculate the scattering function in a coordinate system centered on the object from the spectrum of waves scattered by an incident vector plane wave.

The utility of equations (9) and (10) for solving complex problems can be illustrated by considering their application to the computation of the exact mutual interaction between two arbitrary scattering objects. Solving the two-object problem using MOM requires an eight-fold increase in computation time and twice the storage as is needed for a single object. Twersky [11] has formulated the two-object multiple-scatter problem as an infinite multiple-scatter series, each term of which uses the asymptotic scattering dyadic for one or more of the particles. His method yields some useful approximations for random particle configurations, but the multiple-scatter series cannot be solved exactly. On the other hand, by simply writing (9) and (10) for a two-particle system, we obtain an exact linear equation for the fields crossing the plane separating the two scatterers. Once these *excitation* fields are computed, the complete problem can be solved with a few simple manipulations; moreover, one scatterer can be replaced with a reflecting plane or a rough surface.

For two objects separated by a distance ΔL as shown in Figure 2, a straightforward

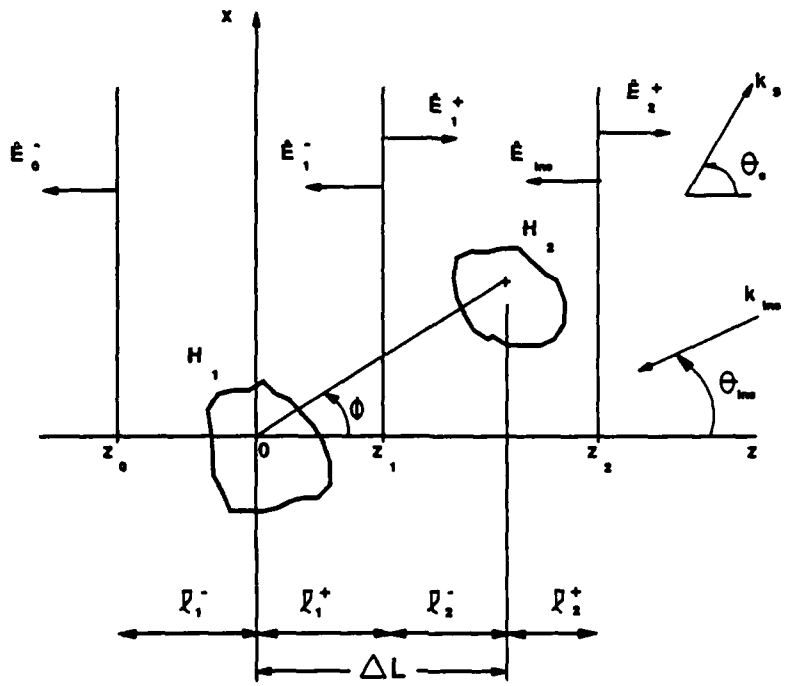

Figure 2: Geometry for two-object computation with definition of symbols.

application of (9) and (10) leads to the following equation for $\widehat{\mathbf{E}}_1^-$:

$$\widehat{\mathbf{E}}_1^- - \widehat{\mathbf{H}}_2^{-+}@(\widehat{\mathbf{H}}_1^{+-}@\widehat{\mathbf{E}}_1^-) = \widehat{\mathbf{E}}_{inc}\exp\{ikgL_2\} + \widehat{\mathbf{H}}_2^{--}@\widehat{\mathbf{E}}_{inc}, \tag{14}$$

where $\widehat{\mathbf{E}}_{inc}$ is evaluated at the plane $z = z_2$. This equation can be solved numerically solved for $\widehat{\mathbf{E}}_1^-$. The remaining fields are then determined from the following equations:

$$\begin{aligned}
\widehat{\mathbf{E}}_1^+ &= \widehat{\mathbf{H}}_1^{+-}@\widehat{\mathbf{E}}_1^- && (15)\\
\widehat{\mathbf{E}}_0^- &= \widehat{\mathbf{E}}_1^-\exp\{ikgL_1\} + \widehat{\mathbf{H}}_1^{--}@\widehat{\mathbf{E}}_1^- && (16)\\
\widehat{\mathbf{E}}_2^+ &= \widehat{\mathbf{E}}_1^+\exp\{ikgL_2\} + \widehat{\mathbf{H}}_2^{++}@\widehat{\mathbf{E}}_1^+ + \widehat{\mathbf{H}}_2^{+-}@\widehat{\mathbf{E}}_{inc} && (17)
\end{aligned}$$

These results are valid for any pair of objects, although some care must be taken in defining the appropriate scattering function for a conducting surface of infinite extent.

Suppose, for example, that the first object is a perfectly conducting infinite planar surface. An arbitrary surface can be generated by adding higher-order spatial Fourier components to the zeroth-order term representing the mean surface height. This component scatters the incident wave in the specular direction and cancels the incident wave in the forward direction on the other side of the surface. Thus, the scattering function for an infinite, perfectly conducting surface contains a delta function. The scattering function for a conducting plane is given by (A75, A76) in the appendix. It is convenient to decompose the scattering function into a regular part, $\widehat{\mathbf{H}}^{\dagger}$, and a singular part. The

singular part consists only of a delta function, which can be integrated analytically. The four scattering functions for a perfectly conducting surface can be written formally as

$$\underline{\kappa}^{\pm}\cdot\widehat{\underline{\mathbf{H}}}_1^{\pm\mp}(\mathbf{K},\mathbf{K}') \equiv \underline{\kappa}^{\pm}\cdot\widehat{\underline{\mathbf{H}}}_1^{\pm\mp\dagger}(\mathbf{K},\mathbf{K}') - \frac{8\pi^2 g(K_s)}{ik}\delta(\mathbf{K}-\mathbf{K}')(\underline{\mathbf{I}} - 2\mathbf{a}_z\mathbf{a}_z), \tag{18}$$

and

$$\underline{\kappa}^{\pm}\cdot\widehat{\underline{\mathbf{H}}}_1^{\pm\pm}(\mathbf{K},\mathbf{K}') \equiv \underline{\kappa}^{\pm}\cdot\widehat{\underline{\mathbf{H}}}_1^{\pm\pm\dagger}(\mathbf{K},\mathbf{K}') - \frac{8\pi^2 g(K_s)}{ik}\delta(\mathbf{K}-\mathbf{K}')\underline{\mathbf{I}}, \tag{19}$$

where $\mathbf{a}_z$ is the unit vector along the z direction. Upon substituting the above scattering functions into equations (14) through (17), we obtain the following results for a surface-particle aggregate:

$$\begin{aligned}\widehat{\mathbf{E}}_1^- &- \widehat{\underline{\mathbf{H}}}_2^{-+}@(\widehat{\underline{\mathbf{H}}}_1^{+-\dagger}@\widehat{\mathbf{E}}_1^-) - \widehat{\underline{\mathbf{H}}}_2^{-+}@\left[(2\mathbf{a}_z\mathbf{a}_z - \underline{\mathbf{I}})\cdot\widehat{\mathbf{E}}_1^-(\mathbf{K}')\exp\{i2kg(\mathbf{K}')\ell_1^+\}\right] \\ &= \widehat{\mathbf{E}}_{inc}\exp\{ikgL_2\} + \widehat{\underline{\mathbf{H}}}_2^{--}@\widehat{\mathbf{E}}_{inc}\end{aligned} \tag{20}$$

$$\widehat{\mathbf{E}}_1^+(\mathbf{K}) = (2\mathbf{a}_z\mathbf{a}_z - \underline{\mathbf{I}})\cdot\widehat{\mathbf{E}}_1^-(\mathbf{K})\exp\{i2kg(\mathbf{K})\ell_1^+\} + \widehat{\underline{\mathbf{H}}}_1^{+-\dagger}(\mathbf{K},\mathbf{K}')@\widehat{\mathbf{E}}_1^-(\mathbf{K}') \tag{21}$$

$$\widehat{\mathbf{E}}_0^-(\mathbf{K}) = 0 \tag{22}$$

$$\widehat{\mathbf{E}}_2^+(\mathbf{K}) = \widehat{\mathbf{E}}_1^+(\mathbf{K})\exp\{ikg(\mathbf{K})L_2\} + \widehat{\underline{\mathbf{H}}}_2^{++}@\widehat{\mathbf{E}}_1^+ + \widehat{\underline{\mathbf{H}}}_2^{+-}@\widehat{\mathbf{E}}_{inc} \tag{23}$$

To convert the forward and backward wave fields to physical observables, we note that at distances well removed from the reference plane, the Helmholtz integral can be approximated by the method of stationary phase to yield

$$\mathbf{E}^{\pm}(\mathbf{r}) \approx \begin{cases} ikg(K_r)\widehat{\mathbf{E}}^{\pm}(\mathbf{K}_r)\exp\{ikr\}/(2\pi r) & \text{three-dimensional} \\ \sqrt{-ik}\,g(K_r)\widehat{\mathbf{E}}^{\pm}(\mathbf{K}_r)\exp\{ikr\}/\sqrt{2\pi r} & \text{two-dimensional}\end{cases} \tag{24}$$

where $\mathbf{K}_r$ is a wave vector directed along $\mathbf{r}$. The physical observable of particular interest to us is the angular power density in the direction $\mathbf{k}$ for a given incidence $\mathbf{k}_i$. It is given by

$$P^{\pm}(\mathbf{k}(\mathbf{K}),\mathbf{k}_i) = \begin{cases} K^2|g(K)|^2|\widehat{\mathbf{E}}^{\pm}(\mathbf{K})|^2/(4\pi^2) & \text{three-dimensional} \\ k|g(K)|^2|\widehat{\mathbf{E}}^{\pm}(\mathbf{K})|^2/(2\pi) & \text{two-dimensional}\end{cases} \tag{25}$$

In the next section we shall relate the angular power density to the dimensionless differential cross section $\gamma(\mathbf{k}(\mathbf{K}),\mathbf{k}_i)$.

It is instructive to specialize the above results for the case of parallel polarization. In this case the wave fields become scalar and equations (14) through (17) or (20)

through (23) can be converted to their equivalent scalar forms by making the following substitutions:

$$\begin{aligned} \hat{\mathbf{E}}_n^{\pm} &\leftarrow \hat{\psi}_n^{\pm} \\ \underline{\kappa}^u(\mathbf{K})\cdot\underline{\widehat{\mathbf{H}}}_n^{\circ}(\mathbf{k}^u(\mathbf{K}),\mathbf{k}^v(\mathbf{K}'))\cdot\hat{\mathbf{E}}_{n-1}^v(\mathbf{K}') &\leftarrow \hat{H}_n^{\circ}(\mathbf{k}^u(\mathbf{K}),\mathbf{k}^v(\mathbf{K}'))\hat{\psi}_{n-1}^v(\mathbf{K}') \\ (2\mathbf{a}_z\mathbf{a}_z - \underline{\mathbf{I}})\cdot\hat{\mathbf{E}}_1^-(\mathbf{K}) &\leftarrow -\hat{\psi}_1^-(\mathbf{K}) \end{aligned}$$

The equations are greatly simplified for isotropic scatterers, in which case

$$\underline{\kappa}^u(\mathbf{K})\cdot\underline{\widehat{\mathbf{H}}}_n^{\circ}(\mathbf{k}^u(\mathbf{K}),\mathbf{k}^v(\mathbf{K}')) \leftarrow h_n, \tag{26}$$

where h_n is a constant. When (26) holds, the @ operator can be evaluated numerically. For example, (13) becomes

$$\underline{\widehat{\mathbf{H}}}_n^{uv}@\hat{\mathbf{E}}_{n-1}^v \leftarrow \frac{ik}{2g(K)}h_n \exp\{-i[\mathbf{K}\cdot\boldsymbol{\rho}_n - kg(K)\ell_n^u]\}\,\psi_{n-1}^v(\boldsymbol{\rho}_n, z_{pn}), \tag{27}$$

where z_{pn} is the z coordinate of the nth particle and ψ_{n-1}^v is the *free-space* propagation of the wave field from the slab boundary z_{n-1} or z_n, i.e.,

$$\psi_{n-1}^v(\boldsymbol{\rho}_n, z_{pn}) = \iint \frac{d\mathbf{K}}{(2\pi)^2}\ \hat{\psi}_{n-1}^v(\mathbf{K})\exp\{i[\mathbf{K}\cdot\boldsymbol{\rho}_n + kg(\mathbf{K})|z_{pn} - z_{n-1}|]\} \tag{28}$$

With these simplifications, the spatial-domain forms of (14) or (20) can be computed analytically. To accommodate both the two- and three-dimensional forms, we let

$$\begin{aligned} G(r) &\equiv \iint \frac{d\mathbf{K}}{(2\pi)^2}\,\frac{i\exp\{i[\mathbf{K}\cdot\boldsymbol{\rho} + kg(K)|z|]\}}{2kg(K)} \\ &= \begin{cases} \exp\{ikr\}/(4\pi r) & \text{three-dimensional} \\ iH_0^{(1)}(kr)/4 & \text{two-dimensional} \end{cases} \end{aligned} \tag{29}$$

Note that the three-dimensional form has the units m^{-1}, whereas the two-dimensional form has no units.

By using (27) and (29), the scalar isotropic form of (14) can be solved for $\psi_1^-(\boldsymbol{\rho}_1, z_{p1})$. To this end, we multiply both sides of (14) by $\exp\{ikg(K)\ell_1^+\}$, take the inverse Fourier transform, and evaluate the result at $\boldsymbol{\rho} = \boldsymbol{\rho}_1$ to obtain

$$\psi_1^-(\boldsymbol{\rho}_1, z_{p1}) = \frac{\psi_{inc}(\boldsymbol{\rho}_1, z_{p1}) + h_2k^2G_{12}\,\psi_{inc}(\boldsymbol{\rho}_1, z_{p2})}{1 - h_1h_2(k^2G_{12})^2}, \tag{30}$$

where

$$G_{12} = G(|\boldsymbol{\rho}_1 - \boldsymbol{\rho}_2 + \Delta L\mathbf{a}_z|) \tag{31}$$

is the spherical-wave propagation factor for the distance between the particles. The denominator of (30) accounts for the mutual interaction of the particles. From (17), the backscattered wave spectrum can be computed as

$$\begin{aligned}\widehat{\psi}_2^+(\mathbf{K}) &= ik[2g(K)]^{-1}h_1 \exp\{-i[\mathbf{K}\cdot\boldsymbol{\rho}_1 - kg(K)(\Delta L + \ell_2^+)]\}\, \psi_1^-(\boldsymbol{\rho}_1, z_{p1}) \\ &\quad + ik^3[2g(K)]^{-1}h_1 h_2 G_{12} \exp\{-i[\mathbf{K}\cdot\boldsymbol{\rho}_2 - kg(K)\ell_2^+]\}\, \psi_1^-(\boldsymbol{\rho}_1, z_{p1}) \\ &\quad + ik[2g(K)]^{-1}h_2 \exp\{-i[\mathbf{K}\cdot\boldsymbol{\rho}_2 - kg(K)\ell_2^+]\}\, \psi_{inc}(\boldsymbol{\rho}_2, z_{p2}). \qquad (32)\end{aligned}$$

The three terms in (32) represent the direct propagation of $\widehat{\psi}_1^-$, the forward scattering of $\widehat{\psi}_1^-$ by the second object, and finally the incident wave backscattered by the second object.

To compute the forward-scattered wave field spectrum $\widehat{\psi}_0^-(\mathbf{K})$, however, we must proceed in two steps. From (14),

$$\begin{aligned}\widehat{\psi}_1^-(\mathbf{K}) &= \widehat{\psi}_{inc}(\mathbf{K}) \exp\{ikg(K)L_2\} + ik[2g(K)]^{-1}h_2 \exp\{-i[\mathbf{K}\cdot\boldsymbol{\rho}_2 - kg(K)\ell_2^-]\} \\ &\quad \times \left[\psi_{inc}(\boldsymbol{\rho}_2, z_{p2}) + h_1 k^2 G_{12} \psi_1^-(\boldsymbol{\rho}_1, z_{p1})\right]. \qquad (33)\end{aligned}$$

Now $\widehat{\psi}_0^-(\mathbf{K})$ can be computed from (16) as

$$\begin{aligned}\widehat{\psi}_0^-(\mathbf{K}) &= \widehat{\psi}_1^-(\mathbf{K}) \exp\{ikg(\mathbf{K})L_1\} + ik[2g(K)]^{-1}h_1 \\ &\quad \times \exp\{-i[\mathbf{K}\cdot\boldsymbol{\rho}_1 - kg(K)\ell_1^-]\}\, \psi_1^-(\boldsymbol{\rho}_1, z_{p1}). \qquad (34)\end{aligned}$$

Following the same procedure, equation (20) can be solved for $\psi_1^-(\boldsymbol{\rho}_2, -\Delta L)$ for the case of an isotropic cylinder above a perfectly conducting plane. However, the factor used is $\exp\{ikg(K)(\Delta L + \ell_1^+)\}$ and the inverse Fourier transform is evaluated at $\boldsymbol{\rho} = \boldsymbol{\rho}_2$. Explicitly,

$$\psi_1^-(\boldsymbol{\rho}_2, -\Delta L) = \frac{\psi_{inc}(\boldsymbol{\rho}_2, -\Delta L) + h_2 k^2\, G(2\Delta L)\, \psi_{inc}(\boldsymbol{\rho}_2, z_{p2})}{1 + h_2 k^2\, G(2\Delta L)}. \qquad (35)$$

The backscattered wave field is given by

$$\begin{aligned}\widehat{\psi}_2^+(\mathbf{K}) &= -\widehat{\psi}_1^-(\mathbf{K}) \exp\{ikg(K)(2\ell_1^+ + L_2)\} + ik[2g(K)]^{-1}h_2 \\ &\quad \times \exp\{-i[\mathbf{K}\cdot\boldsymbol{\rho}_2 - kg(K)\ell_2^+]\} \left[\psi_{inc}(\boldsymbol{\rho}_2, z_{p2}) - \psi_1^-(\boldsymbol{\rho}_2, -\Delta L)\right], \qquad (36)\end{aligned}$$

where $\widehat{\psi}_1^-(\mathbf{K})$ is found from (20) to be

$$\begin{aligned}\widehat{\psi}_1^-(\mathbf{K}) &= \widehat{\psi}_{inc}(\mathbf{K}) \exp\{ikg(K)L_2\} + ik[2g(K)]^{-1}h_2 \\ &\quad \times \exp\{-i[\mathbf{K}\cdot\boldsymbol{\rho}_2 - kg(K)\ell_2^-]\} \left[\psi_{inc}(\boldsymbol{\rho}_2, z_{p2}) - \psi_1^-(\boldsymbol{\rho}_2, -\Delta L)\right]. \qquad (37)\end{aligned}$$

We shall see that the two terms in (30) or (35) combined with the leading two terms in (32) or (36) can add coherently to produce a four-fold amplitude enhancement or 12 dB. For irregular surfaces, which cannot be accommodated analytically, the enhancement is potentially larger.

In conclusion let us note that if the scattering functions are known, (14) or (20) can be put in the form of a system of linear equations by performing a matrix multiply to evaluate the left-hand sides and a vector multiply to evaluate the right-hand sides. The system of equations can then be solved numerically to determine $\widehat{\mathbf{E}}_1^-$. The computation time is dominated by the matrix multiply ($\sim N_r^3$ computations if $\widehat{\underline{\mathbf{H}}}(\mathbf{k}_s^\pm, \mathbf{k}_i^\pm)$ is an $N_r \times N_r$ matrix), and the solution of the resulting matrix equation (an additional $\sim N_r^3$ computations). The computation time for the remaining fields, which involve only matrix-vector multiplies, is negligible. Thus, the total number of computations for solving the two-scatterer problem varies like $2N_r^3$ with the mutual-interaction-method (MIM) versus $(2N_r)^3$ for MOM.

III.2 Numerical Simulations

For the numerical simulations, we will only consider problems that admit variations in two dimensions (x, z). The above equations are essentially unchanged except that $\mathbf{K}$ is replaced by k_x. For example, equation (13) becomes

$$\underline{\widehat{\mathbf{H}}}_n^{u\pm} @ \widehat{\mathbf{E}}_{\substack{n-1\\n}}^{\pm} \equiv \exp\{ikg(k_x)\ell_n^u\} \int \frac{dk_x'}{2\pi} \frac{ik \exp\{-i(k_x - k_x')x_n\}}{2g(k_x)} \times \underline{\kappa}^u(k_x) \cdot \underline{\widehat{\mathbf{H}}}_n^o(\mathbf{k}^u(k_x), \mathbf{k}^{\pm}(k_x')) \cdot \widehat{\mathbf{E}}_{\substack{n-1\\n}}^{\pm}(k_x') \exp\{ikg(k_x')\ell_n^{\mp}\}. \quad (38)$$

To solve for the mutual interaction between two objects, we need to know their individual scattering functions. The appendix presents a complete derivation of the scattering function of a single object with explicit results for an infinite cylinder, an infinite conducting plane, and a planar conducting surface. The scattering function of all but the rough conducting surface can be obtained in analytic form.

To illustrate the mutual interaction method, we will perform computations for (1) a pair of parallel cylinders and (2) a cylinder above an infinite conducting surface. The z axis is vertical, with the axis of cylindrical symmetry lying along the y axis. Thus, the surface height varies only in the x direction. The incident wave normal vector is assumed to lie entirely in the xz plane with two principal polarizations. For axial or parallel polarization, the incident electric field vector is perpendicular to the incidence plane (i.e., parallel to the cylinder axis). For transverse or vertical polarization it lies in the plane of incidence (i.e., perpendicular to the y axis). The projection of the scattering dyadic onto the direction of the incident wave can be written in the general form

$$\underline{\kappa} \cdot \underline{\widehat{\mathbf{H}}}(k_{sx}, k_{ix}) \cdot \mathbf{a}_i(k_{ix}) = \mathbf{a}_s(k_{sx}) H_{\|,\perp}(k_{sx}, k_{ix}), \quad (39)$$

where $\mathbf{a}_{i,s}(k_x)$ is a unit vector along the k_x Fourier component of the incident or scattered wave field. In general, $\mathbf{a}_s$ depends on the object's geometry and the incident wave polarization.

For an infinite cylinder with refractive index m and radius a, lying along the y axis, the scattering functions are given as follows:

$$H_{\|}(\mathbf{k}_s, \mathbf{k}_i) = 4ik^{-2} \sum_{n=-\infty}^{\infty} c_n \exp(in\alpha), \quad (40)$$

and

$$H_{\perp}(\mathbf{k}_s, \mathbf{k}_i) = 4ik^{-2} \sum_{n=-\infty}^{\infty} d_n \exp(in\alpha), \quad (41)$$

where c_n, d_n, and α are given by (A63) to (A72) in the appendix. These equations define the scattering functions for all values of k_{sx} and k_{ix}. When $|k_{sx}| > k$ or $|k_{ix}| > k$, α is complex.

Figure 3 shows the magnitude of the scattering functions of a perfectly conducting cylinder and a dielectric cylinder with refractive index $m = 1.5$ illuminated by an axially polarized, 7.5-m free-space wavelength wave. Both cylinders have the same 1-m diameter. The plot shows the magnitude as a function of the normalized scattered wave number k_{sx} for a fixed incidence $k_{ix} = 0$. The scattering functions are essentially constant over the range of $|k_{sx}/k| \leq 1$, i.e., all real azimuthal angles. This is the scattering behavior of the zeroth-order cylindrical normal mode, which is azimuthally independent. Thus, the zeroth-order cylindrical normal mode dominates the scattering for this cylinder.

In general, a small cylinder ($a/\lambda \ll 1$) scatters essentially uniformly in azimuth, and the scattering function can be approximated by the zeroth-order term only, whereby

$$\left\{ \begin{array}{c} H_{\|} \\ H_{\perp} \end{array} \right\} = 4ik^{-2} \left\{ \begin{array}{c} c_0 \\ d_0 \end{array} \right\} \equiv h, \tag{42}$$

which can be used in (30) and (32) or (35) and (36). If the cylinder diameter is large compared to the incidence wavelength, however, the scattering function is no longer axially symmetric. This behavior can be seen in Figure 4, which is the corresponding scattering function for a large cylinder. In this case the higher-order cylindrical normal modes are significant, and the integral equation (14) lends itself to numerical solution only. For rough surfaces, numerical solutions must be used in all cases.

The scattering functions for an infinite conducting plane are given by ($A75$) and ($A76$), which are reproduced here for reference purposes:

$$\underline{\kappa}^{\pm} \cdot \underline{\widehat{\mathbf{H}}}^{\pm\mp}(k_{sx}, k_{ix}) = -\frac{4\pi g(k_{sx})}{ik} \delta(k_{sx} - k_{ix})(\mathbf{a}_x \mathbf{a}_x - \mathbf{a}_z \mathbf{a}_z) \tag{43}$$

$$\underline{\kappa}^{\pm} \cdot \underline{\widehat{\mathbf{H}}}^{\pm\pm}(k_{sx}, k_{ix}) = -\frac{4\pi g(k_{sx})}{ik} \delta(k_{sx} - k_{ix})(\mathbf{a}_x \mathbf{a}_x + \mathbf{a}_z \mathbf{a}_z) \tag{44}$$

Thus, the scattering function for a conducting plane consists only of a delta function. The backward scattering functions $\underline{\widehat{\mathbf{H}}}^{+-}$ and $\underline{\widehat{\mathbf{H}}}^{-+}$ describe the specular reflection of the incident wave. The forward scattering functions $\underline{\widehat{\mathbf{H}}}^{++}$ and $\underline{\widehat{\mathbf{H}}}^{--}$ represent the direct propagation of the incident wave with a phase shift of 180° so that the total wave vanishes identically behind the plane. The scattered wave behind a flat or rough conducting surface always exactly cancels the incident wave. Hence, the forward scattering function always contains a delta function. The scattering function can have additional delta functions, however, because the scattering of a wave from a surface is a wave-wave scattering process where the second wave comes from the surface itself. The spectrum of a rough surface can contain one or more discrete Fourier components. The discrete component at zero spatial frequency corresponds to the zero-mean surface component. These discrete Fourier components are responsible for the specular reflection of the incident wave.

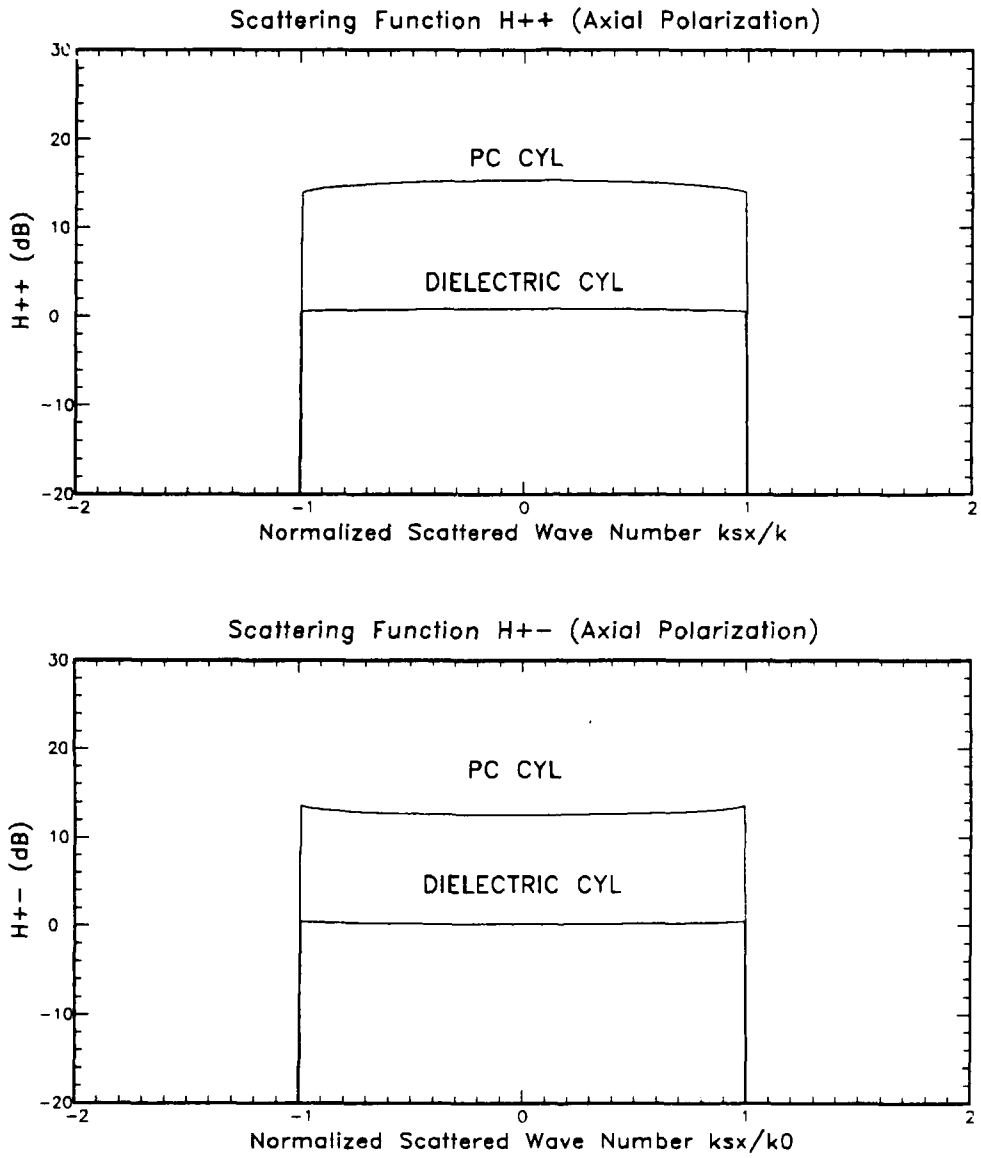

Figure 3: Magnitude of the scattering function of an infinitely long cylinder 15 m in diameter illuminated by an axially polarized 7.5-m wavelength wave incident along the z axis for two cases: (a) perfect conductor, (b) dielectric with refractive index of 1.5.

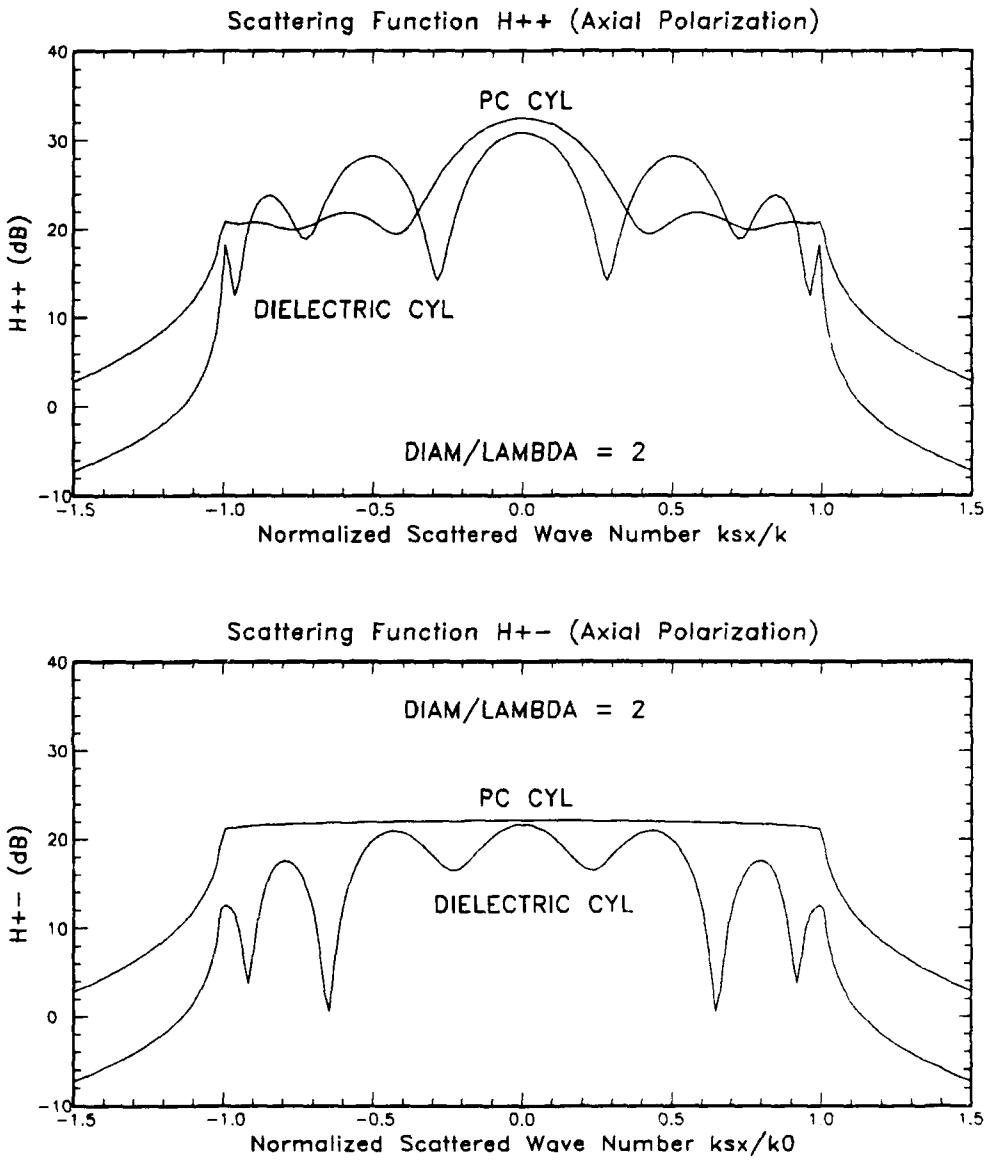

Figure 4: Magnitude of the scattering function of an infinitely long cylinder 15 m in diameter illuminated by an axially polarized 7.5-m wavelength wave incident along the z axis for two cases: (a) perfect conductor, (b) dielectric with refractive index of 1.5.

Because each specular reflection is characterized by a delta function, it is desirable to separate the scattering function into a regular part, $\widehat{\mathbf{H}}^{\dagger}$, and a singular part consisting of all the delta functions. Thus, the scattering dyadic can be written formally as

$$\widehat{\mathbf{H}}(k_{sx}, k_{ix}) = \widehat{\mathbf{H}}^{\dagger}(k_{sx}, k_{ix}) + \sum_{p,q} \mathbf{a}_p \mathbf{a}_q h_{pq} \delta(k_{sx} - k_{x,pq}), \tag{45}$$

where h_{pq} is the appropriate amplitude, $\mathbf{a}_p$ or $\mathbf{a}_q$ is a unit vector, and the summation runs over all three orthogonal directions. The singular part can then be integrated analytically in the above difference equations before any numerical solutions are attempted.

The above decomposition is always applied to the surface scattering functions in our numerical solutions. For a conducting surface the regular part is identically zero. It is not obvious, however, how to identify the singular part for a rough surface since it is implicitly contained in the numerical solutions. In fact, the results from ($A80$) to ($A95$) in the appendix can be summarized as follows:

$$H_{\|}^{+-}(k_{sx}, k_{ix}) = \frac{2g(k_{sx})}{ik} \widehat{E}_{sy}(k_{sx}) \tag{46}$$

$$H_{\perp}^{+-}(k_{sx}, k_{ix}) = \frac{2g(k_{sx})}{ik} \widehat{E}_{s}(k_{s}) \tag{47}$$

$$H_{\|}^{--}(k_{sx}, k_{ix}) = H_{\perp}^{--}(k_{sx}, k_{ix}) = -\frac{4\pi g(k_{sx})}{ik} \delta(k_{sx} - k_{ix}) \tag{48}$$

To extract the singular part, note that the backward-scattering function H^{+-} is always singular because the zero-mean component of an infinite rough surface always scatters the incident wave in the specular reflection direction. Assuming that the surface has no other discrete harmonics, we can identify the regular part of the backward scattering functions by subtracting the flat-surface component as follows:

$$H_{\|,\perp}^{+-\dagger} = H_{\|,\perp}^{+-} + \frac{4\pi g(k_{sx})}{ik} \delta(k_{sx} - k_{ix}) \tag{49}$$

The above results are given in terms of the scattered wave fields $\widehat{E}_s$ and $\widehat{E}_{sy}$, but these fields cannot be derived analytically for a rough surface. In principle, they can be obtained by solving numerically the problem of a *unit-amplitude* incident plane wave scattering from the surface. Unfortunately, the incident wave spectrum is a delta function and therefore cannot be implemented numerically; however, the delta function can be approximated by a finite-amplitude function to as high a degree of accuracy as desired. A convenient choice is a narrow gaussian incident beam of the form

$$\widehat{E}_i(k_x; z) = \frac{2\sqrt{\pi}}{k_w} \exp\{-(k_x - k_{xi})^2 / k_w^2\} \exp\{ik_z(k_{xi})z\}. \tag{50}$$

where $k_{xi} = k \sin\theta_i$ and $k_w = \text{const.}$ (This gaussian beam is also used in the appendix in the discussion of analytic continuation of the scattering function.) Note that the k_x-integrated magnitude is unity, i.e.,

$$\int_{-\infty}^{\infty} \frac{dk_x}{2\pi} \left|\widehat{E}_i(k_x; z)\right| = 1, \tag{51}$$

and the incident beam approaches a unit-amplitude plane wave, $2\pi\delta(k_x - k_{xi})$, as $k_w \to 0$. The scattering function is very sensitive to the beamwidth parameter k_w. This parameter is chosen such that the numerically discretized gaussian beam has only one overwhelmingly dominant component at the central frequency $k_x = k_{xi}$. We typically choose $k_w = 8/L$ where L is the length of the discretized surface.

The mutual interaction integral equation (14) is readily solved after the scattering function of each scatterer is completely determined, either numerically or analytically. The scattered wave field $\widehat{\mathbf{E}}_1^-$ can be solved numerically for an arbitrary incident wave field, from which $\widehat{\mathbf{E}}_2^+$ and all the backscatter attributes can be computed (see Figure 2); however, these backscatter attributes are usually defined for an incident plane wave. For numerical computation, we can approximate a plane wave by a narrow gaussian beam of the form

$$\widehat{E}_i(k_x; z) = A \exp\{-(k_x - k_{xi})^2/k_w^2\} \exp\{ik_z(k_{xi})z\}, \tag{52}$$

where A is the amplitude to be chosen. The choices were discussed in Section II.

For sufficiently small values of k_w/k, which approximates a plane wave, it can be shown that if A is chosen so that the amplitude of the narrow gaussian beam integrates to unity, then the angular power density $P(\mathbf{k}_s, \mathbf{k}_i)$ of the scattered wave field in the direction $\mathbf{k}_s$ [cf. Eq. (25)] is numerically equal to the *cross section* $\sigma(\mathbf{k}_s, \mathbf{k}_i)$ of the two-object aggregate. If A is chosen so that the power in the beam integrates to unity, then $P(\mathbf{k}_s, \mathbf{k}_i)$ is equal to the differential scattering coefficient $\gamma(\mathbf{k}_s, \mathbf{k}_i)$. In the former case, the scaling factor A is equal to $2\sqrt{\pi}/k_w$ [cf. Eq. (50)], whereas in the latter case A is determined by the condition that the total power integrated over all directions is unity, i.e.,

$$\int_0^{2\pi} |\mathbf{E}_i(r, \theta)|^2 r \, d\theta = \int_{-k}^{k} \frac{dk_x}{2\pi} \, g(k_x) |\widehat{\mathbf{E}}_i(k_x; z)|^2 = 1. \tag{53}$$

Thus, the conversion factor in two-dimensional problems is given by

$$\frac{\sigma(\mathbf{k}_s, \mathbf{k}_i)}{\gamma(\mathbf{k}_s, \mathbf{k}_i)} = \frac{4\pi}{k_w^2} \int_{-k}^{k} \frac{dk_x}{2\pi} g(k_x) \exp\{-(k_x - k_{xi})^4/k_w^4\}. \tag{54}$$

For higher-than-grazing incidence this integral can be evaluated in a power series as follows:

$$\frac{\sigma(\mathbf{k}_s, \mathbf{k}_i)}{\gamma(\mathbf{k}_s, \mathbf{k}_i)} = \frac{g(k_{xi})}{k_w} \sum_{n=0}^{\infty} a_{2n} \Gamma\left(\frac{2n+1}{4}\right) k_w^{2n}. \tag{55}$$

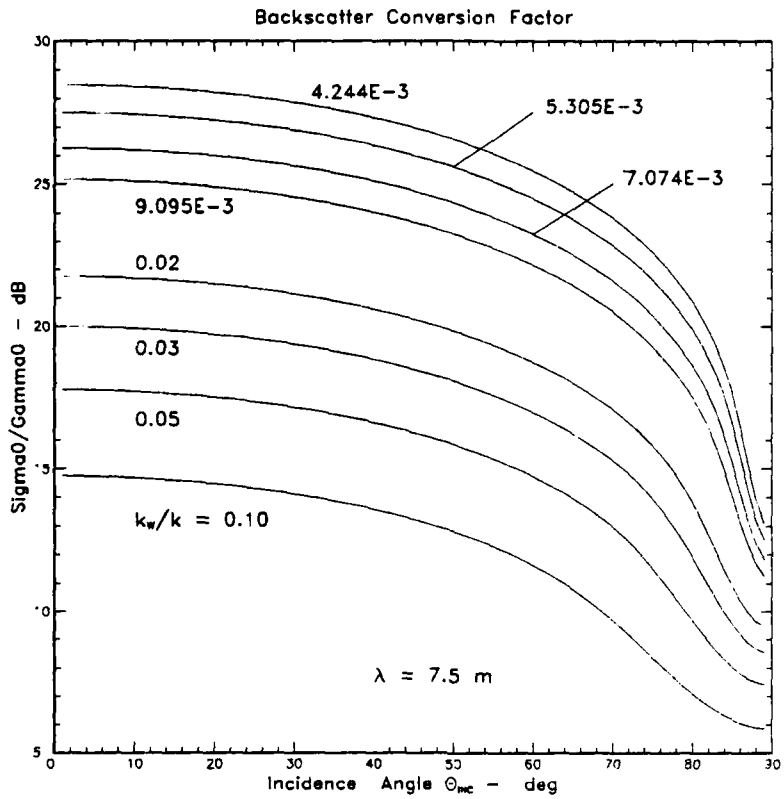

Figure 5: Backscatter conversion factor σ_0/γ_0 for $\lambda = 7.5$ m as a function of incidence angle for different values of the normalized beamwidth parameter k_w/k.

$$a_0 = 1, \tag{56}$$

$$a_2 = -1/[2k^2g^2(k_{xi})], \tag{57}$$

$$a_4 = -\frac{1 + 4k_{xi}^2/k^2}{8k^4g^4(k_{xi})}, \tag{58}$$

$$a_6 = -\frac{1 + 12k^{-2}k_{xi}^2 + 8k^{-4}k_{xi}^4}{16k^6g^6(k_{xi})}. \tag{59}$$

Note that σ has the dimension of length, whereas γ is dimensionless, which is consistent with (54). Equation (54) was calculated numerically for $\lambda = 7.5$ m and is plotted in Figure 5 as a function of the incidence angle for different values of the normalized beamwidth k_w/k. It can be seen that for the same beamwidth k_w, the conversion factor

depends on the angle of incidence. All of the examples in this report use $\lambda = 7.5$ m and $k_w/k = 9.095 \times 10^{-3}$ (which corresponds to $L/\lambda = 140$) so that the conversion factor is 22.16 dB at 60° incidence, 20.51 dB at 70°, and 17.51 dB at 80°. Since σ/γ is proportional to λ^2, Figure 5 can also be used to infer the conversion factor for wavelengths other than 7.5 m.

III.3 Examples

To illustrate the flexibility of MIM for different objects, the calculation procedure described in Section III.2 has been applied to the following scattering problems: (a) two identical closely spaced cylinders, (b) an infinite cylinder near a conducting plane, and (c) an infinite cylinder near a conducting rough surface with a power-law spatial wave number distribution. The cylinders are 1 m in diameter and perfectly conducting (PC). The wavelength for all our computations is 7.5 m, corresponding to an acoustic frequency of 200 Hz. We use the scalar/acoustic model, which is equivalent to parallel EM polarization for the two-dimensional problem. For the initial calculations, we use an incidence angle of 60° with respect to the two-particle vertical axis or the surface normal. The small incidence angle is the least demanding from a computational point of view. Thus, it is a convenient starting point.

We first show the effects of the strong mutual interaction between two cylinders—example (a). Figures 6 shows the bistatic scattering coefficient for $\Delta L = 5$ m superimposed on the scattering cross section for a single cylinder. The scattered field from the single cylinder is nearly isotropic at a level -29.78 dB in the normalized cross section units we are using. The 60° incidence angle with respect to the two-cylinder axis corresponds to $\phi = -45°$ and $\theta_{inc} = 15°$ in Figure 2. Figure 7 shows the backscatter variation as the cylinder is moved away from the surface. The backscatter is alternately enhanced and reduced relative to the free-space level; however, the peak backscatter enhancements exceed the 6-dB level that would result from a simple coherent superposition of the individual backscattered fields. Thus, multiple scattering is important here. The solid curve is the analytic result for isotropic scatterers—(30) and (32). The dominant features are preserved, but there are significant differences even though the departures from isotropy are slight. We shall see that these effects are more pronounced for plane surfaces.

To validate the MIM computations, the two-cylinder MIM results have been compared to computations made with the NEC generalized electromagnetics code. The NEC code performs three-dimensional computations using MOM. Figure 8 shows the backscatter level as a function of separation for a wave incident along the axis of the cylinders ($\phi = 0°; \theta_{inc} = 0°$), which tends to miminimize the backscatter enhancement. Figure 9 shows the same computation for an incident wave broadside to the axis of the

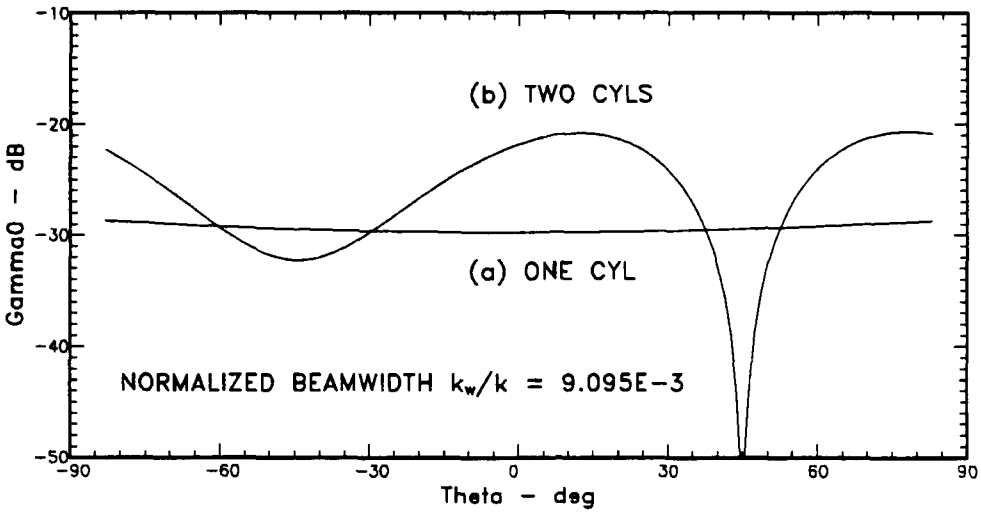

Figure 6: Differential scatter coefficient for (a) a single cylinder and (b) two identical cylinders separated by 5 m.

cylinders ($\phi = -45°; \theta_{inc} = 45°$), which tends to maximize the backscatter enhancement. As discussed in Section III.1, the 12-dB enhancement over the free-space backscatter level is attributed to the fact that the small cylinders are nearly isotropic radiators and there is a reciprocal pair of paths involving multiple reflections that can contribute an additional doubling of the backscatter amplitude. We shall see that this effect is even more prominent for small cylinders near a plane or rough surface. The small discrepancies between the MOM and MIM results are attributable to the three- and two-dimensional geometries and the finite beamwidth used in the mutual-interaction computations. In the NEC code, an incident plane wave and long but finite cylinders were used. The MIM calculations ran more than three times faster than the NEC code, but the comparison is not definitive because of the generality of the NEC code and the fact that the MIM computation was initiated with known scattering functions.

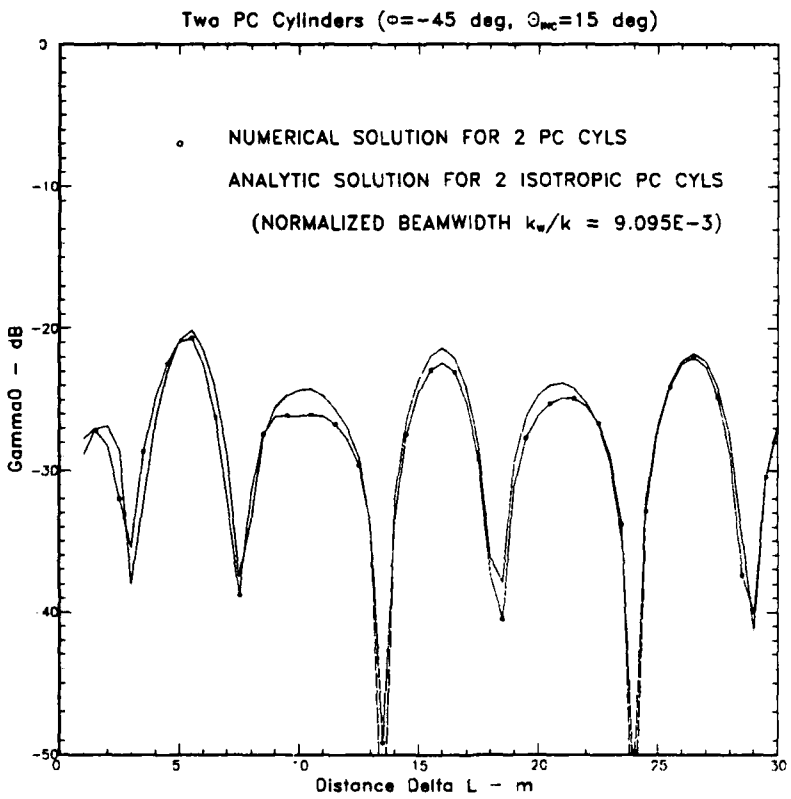

Figure 7: Backscatter cross section for two identical cylinders as a function of their separation ΔL.

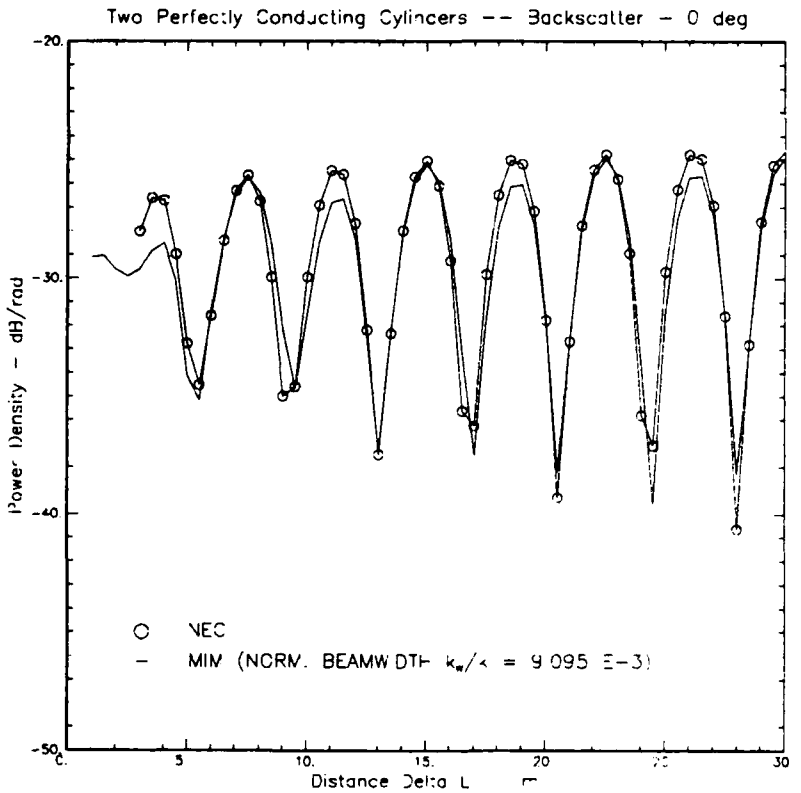

Figure 8: Comparison of NEC and MIM calculations for a wave incident along the axis of the cylinders.

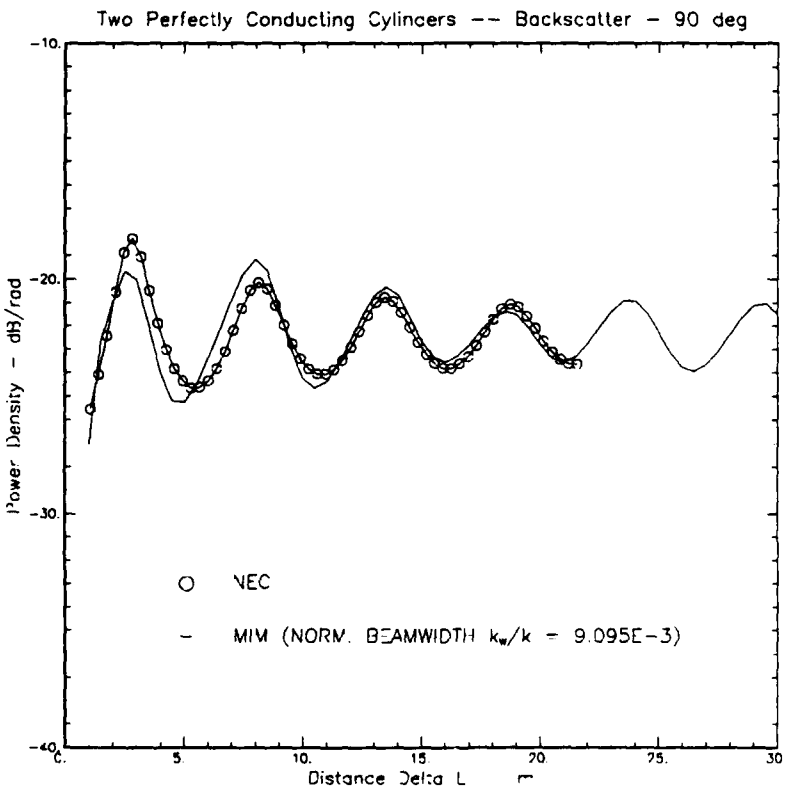

Figure 9: Comparison of NEC and MIM calculations for a wave incident broadside to the axis of the cylinders.

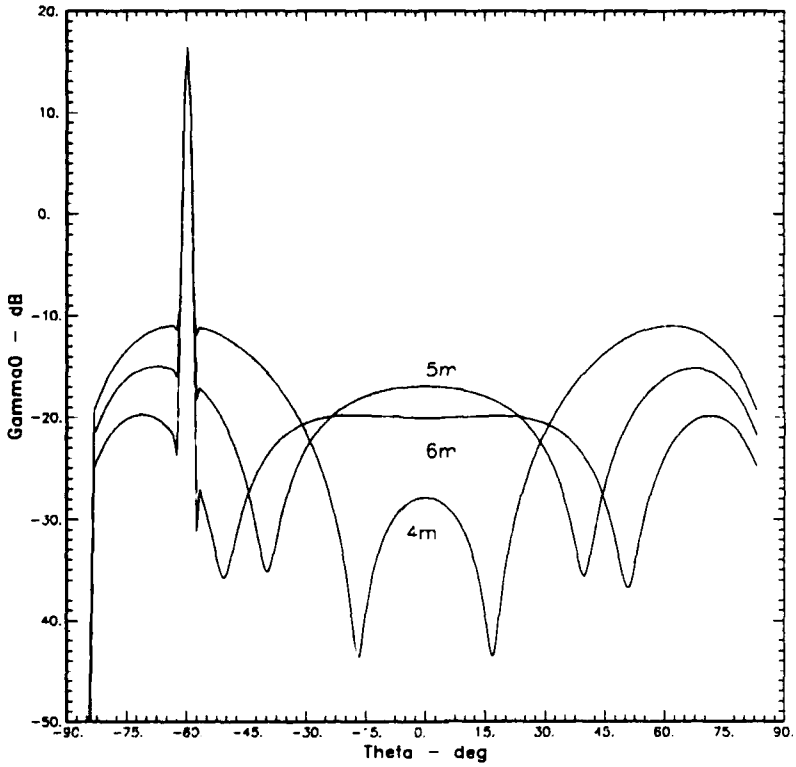

Figure 10: Differential scatter coefficient for a cylinder and a flat surface for three values of the distance ΔL (4, 5, and 6 m).

We now turn to example (b), effectively by replacing the first object in Figure 2 with a flat surface at $z = 0$. Figure 10 shows the differential scatter coefficient as a function of scattering angle for an incidence angle of 60° with respect to the surface normal and for three values of ΔL (4, 5, and 6 m). The peaks at $\theta = -60°$ are due to the specular reflection from the surface. In the backscatter directions, the scatter is much stronger than the corresponding level from a single cylinder; moreover, the backscatter at $\Delta L = 4$ m exceeds the maximum level achieved for two cylinders—see Figure 7. Figure 11 shows the variation in the differential scatter at $\Delta L = 5$ m for incidence angles of 60°, 70°, and 80°. For this particular separation, the backscatter level is nearly constant for the three incidence angles shown, but the incidence-angle dependence of the backscatter level is strongly dependent on the distance of the cylinder from the surface.

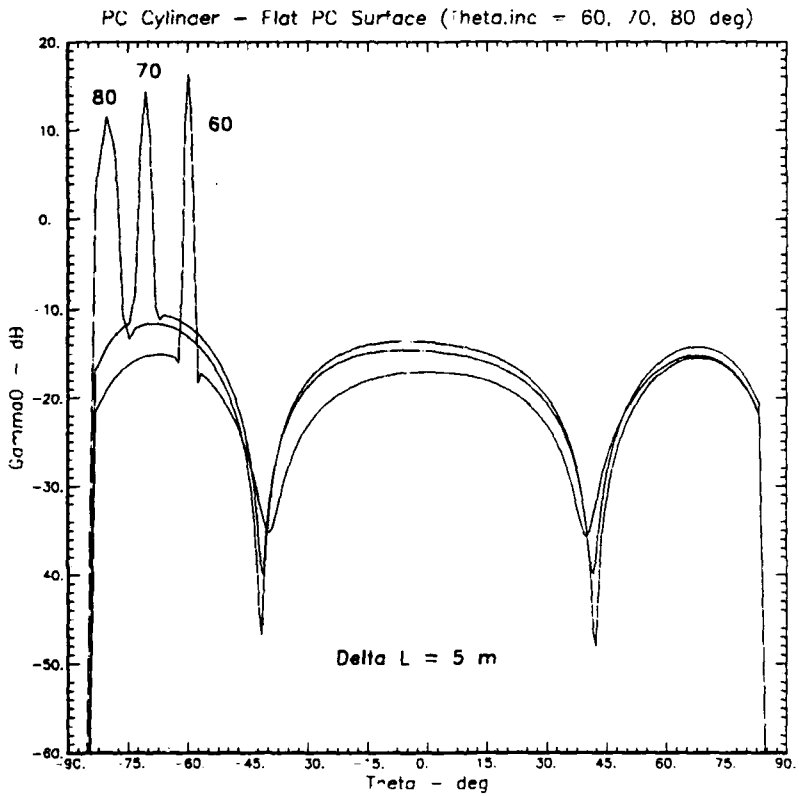

Figure 11: Differential scatter coefficient for a cylinder and a flat surface for three values of the incidence angle θ_i (60°, 70°, and 80°).

Figures 12, 13, and 14 show the backscatter variation as a function of distance for the 60°, 70°, and 80° incidence angles used in Figure 11. The backscatter enhancement peak is insensitive to incidence angle, but its location moves progressively away from the surface as the incidence angle is increased. For comparison purposes we have also plotted the analytic isotropic formula (36) where the cylinder's scattering function is approximated by the azimuthally independent term only. If we use strictly isotropic scattering functions in the numerical computations, the analytic and numerical results are identical. Thus, the differences between the two sets of computations shown in Figures 12, 13, and 14, are due entirely to the small departure from isotropy of the scattering from the 1-m cylinder. We see that the isotropic formula predicts higher peaks and deeper nulls, with the differences increasing with increasing incidence angle. Both the analytic and numerical results show the effects of higher-order interaction terms as the incidence angle increases. Both results also show that the backscatter enhancement peak increases with increasing incidence angle. At 80°, it exceeds 12 dB for both the exact and isotropic curves.

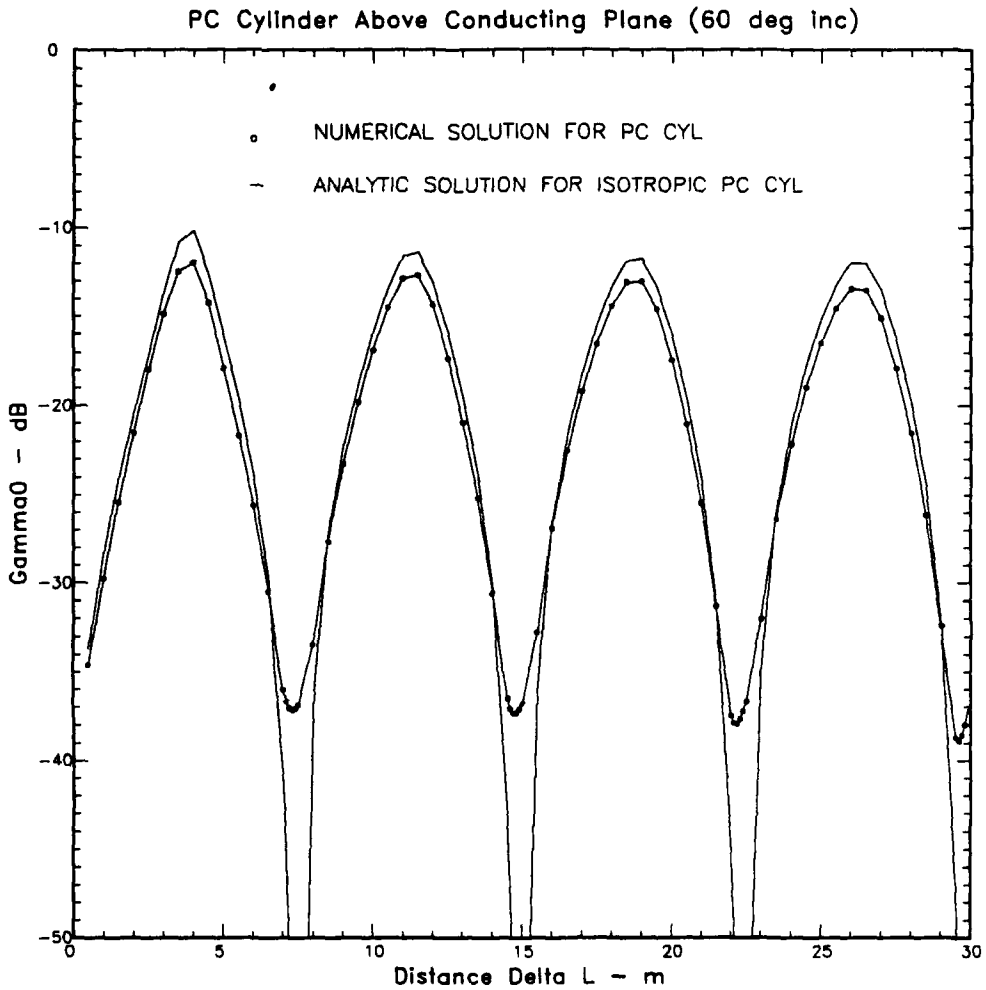

Figure 12: Backscatter cross section for cylinder near plane as a function of distance ΔL at 60° incidence.

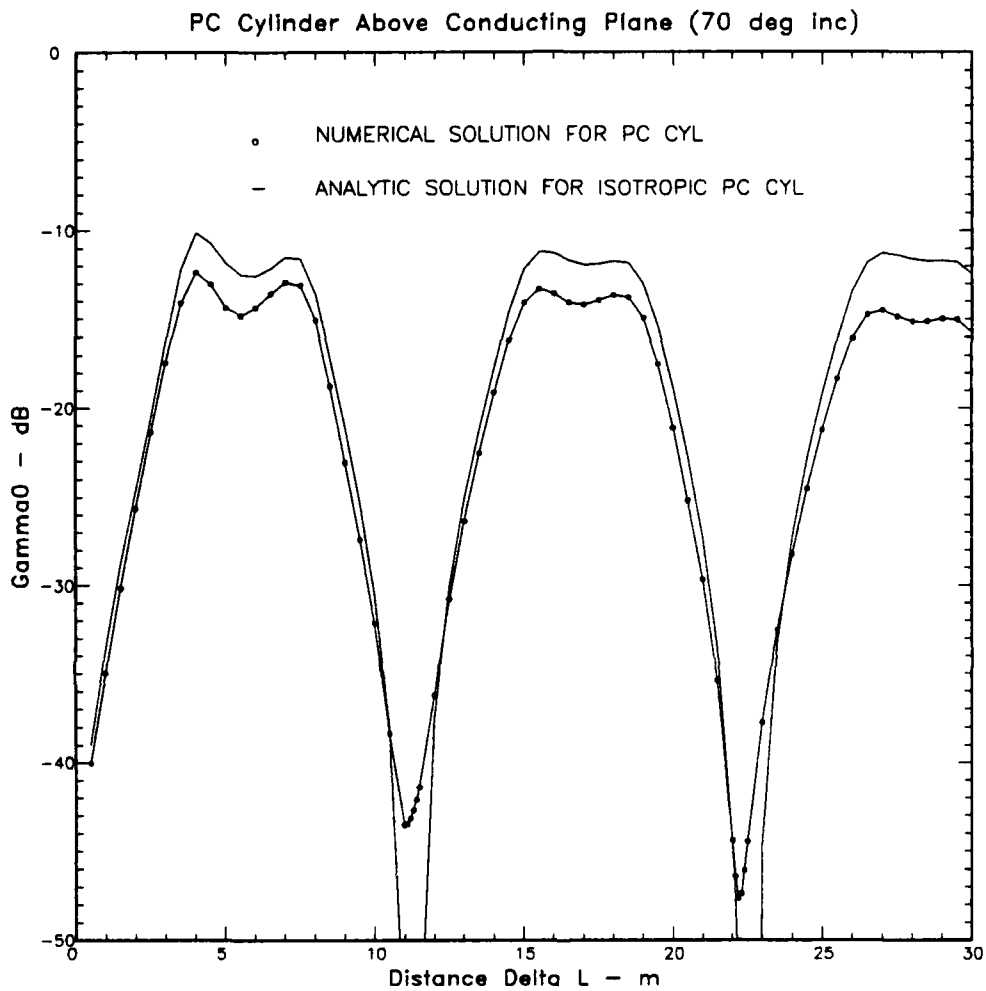

Figure 13: Backscatter cross section for cylinder near plane as a function of distance ΔL at 70° incidence.

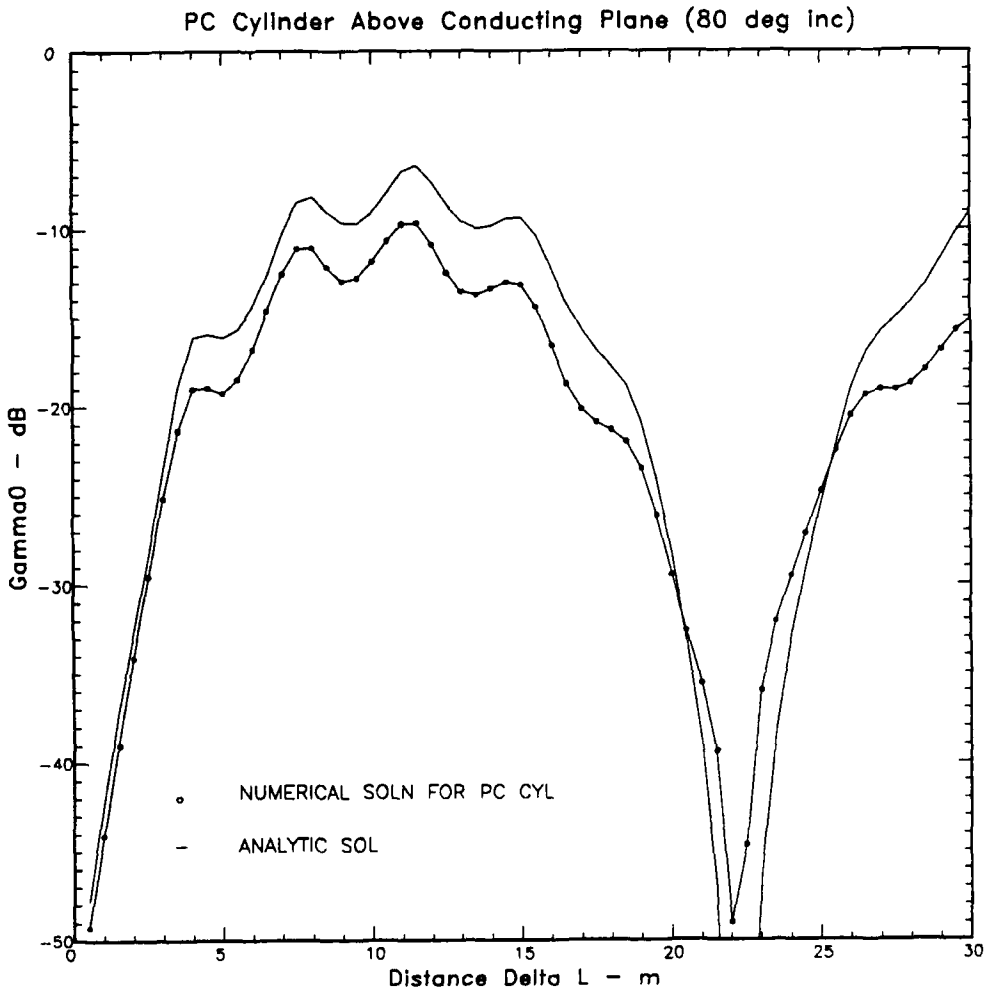

Figure 14: Backscatter cross section for cylinder near plane as a function of distance ΔL at 80° incidence.

To introduce the results of primary interest, we now turn to example (c). A flat surface alone scatters energy only in the specular reflection direction; however, if the surface is made slightly rough, the energy of the incident wave will be scattered potentially in all upward directions. The scattering characteristics of such a rough surface are shown in Figure 15. Panel (a) shows the realization of a linear ocean surface at wind speed $U = 10$ m/s. Panel (b) shows the differential scattering coefficient for a wave (1) incident on this linear ocean surface alone, (2) incident on the linear ocean surface with a cylinder 5 m below the zero-mean surface level, and (3) a PC cylinder 5 m below a planar surface. The scattering characteristics of the linear ocean surface alone were computed numerically using MOM, which illustrates the technique of combining objects whose individual scattering characteristics are more easily managed.

Several points should be noted. The effects of the cylinder interacting with the rough surface exceed the rough-surface level at essentially all scattering angles greater than $-20°$. In the backscatter region, the scatter from the cylinder dominates, but the rough-surface level is several dB higher than the exact computation for the flat surface. It should also be noted that the bistatic scatter mimima between 40° and 50° for the rough and flat surfaces are significantly displaced from one another. The actual surface realization is shown in Figure 15 (a). One can see that even when the surface height is still a small fraction of a wavelength there it exerts a significant effect on the scattering characteristics of a nearby object. For small levels of roughness the interaction tends to systematically increase the backscatter enhancement.

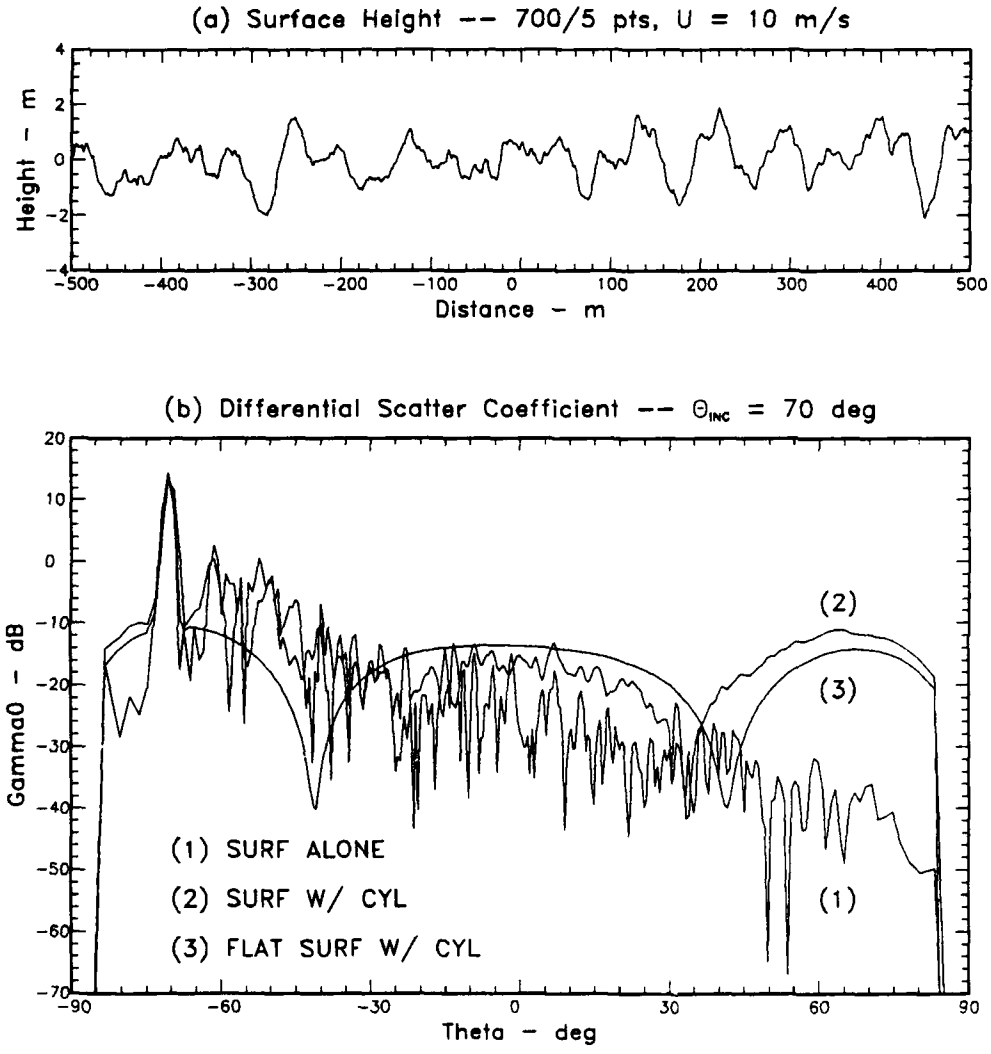

Figure 15: (*a*) A realization of a zero-mean one-dimensional linear ocean surface. (*b*) Differential scatter coefficient (1) for this surface alone, (2) for a PC cylinder 5 m below this surface, and (3) for a PC cylinder 5 m below a planar surface.

IV Scattering from Near-Surface Bubble Clouds

As discussed in Section I, the bubble clouds are modeled as static impermeable objects with known scattering characteristics. At this level of idealization, there is no serious compromise in assuming the bubbles to be perfect voids; moreover, to accommodate the surface interaction under the high sea state conditions that cause the bubble clouds, we are constrained to two dimensions. Thus, we will perform our model computations for an impermeable cylinder near an irregular surface. Because the low-frequency cutoff of the anomalous scatter is likely to be dependent on detailed bubble characteristics, we have used the single intermediate frequency of 200 Hz for all the simulations. We have also used only one representative bubble diameter of 1 m. The variable parameters are wind speed, incidence angle, and the distance of the bubble cloud from the surface height reference level. As the mutual interaction equations are formulated herein, we must have a plane separating the surface from the adjacent scattering object representing the bubble cloud. Thus, the minimum distance at which we can compute bubble cloud scattering is the depth of the deepest trough for the particular surface realization.

The surface realizations are generated by applying the improved linear representation method described in [1], which allows us to efficiently convert linear Donelan-Pierson ocean-surface realizations to their nonlinear counterparts. The acoustic scatter simulations are formally equivalent to horizontally polarized EM scattering, but the scattered signals are reflected from the bottom side of the surface realizations. In [1] we showed that the top-bottom asymmetry of nonlinear surfaces can change the cross section by as much as 5 dB at high sea states. For ocean-surface realizations, sea state is the principal parameter. The simulations were run for three wind conditions: $U = 10$, 15, and 20 m/s, or 20, 30, and 40 knots. Although some accommodation must be made for the one-dimensional surface realizations, these correspond roughly to Beaufort sea states 5, 7, and 9, respectively. Sea state 9 is a strong gale. The reference surface bistatic scatter coefficient is computed for each wind speed, with typical values lying between -50 and -60 dB–see Figure 1. All the results are presented as unitless differential scatter coefficients. The conversion to cross section units is discussed in Section III.2.

As a reference for each wind speed and incidence angle combination, we plot (1) the surface realization for the first rough surface, (2) the bistatic scatter coefficient for the surface alone, (3) the analytic bistatic scatter coefficient for an isotropic scatterer below a plane surface, and (4) the bistatic scatter coefficient at the distance near the first maxima. The cylinder is located along the z axis, with the depth of the maximum trough indicated on the reference plot. To complete each set, we plot the backscatter coefficient for each realization as a function of distance from the common reference level and the corresponding analytic result for isotropic scatterers. The reference level for the rough surfaces is the constant height level that results from linearly detrending the

surface segment as described in [1]. This reference level is close to (within 10%) but not equal to the mean surface height.

The computations are performed for incidence angles of 60°, 70°, and 80°. For positive incidence angles, wave motion is toward the observer. This mainly affects the symmetry of the surface Doppler spectra, which are not computed for this preliminary static bubble cloud model. Two independent surface realizations were used for each computation to show the sensitivity to the detailed surface structure. The plots are presented in order of increasing wind speed at the end of this section. The top-bottom asymmetry of the nonlinear surface realizations is evident in the reference plots.

All the simulations presented here were run at the NASA-Ames NAS supercomputer center on a CRAY Y-MP computer. The computation time is driven by the two matrix inversions required. For a given surface realization, a single impedance-matrix inversion provides the information needed to compute the surface scattering function for all incidence angles. Computation of the nonlinear surface realization requires only Fourier transformations and efficient vector manipulations. Solution of the mutual interaction equations requires another matrix inversion. The primary check on the integrity of the computations is energy conservation. Because the surface and the cylinder are impenetrable and lossless, all the acoustic energy that is directed toward the surface and cylinder must be accounted for in backscatter. Depending on wind speed, to achieve better than 10% and ideally better than 1% overall energy conservation required 700 to 1200 unknowns. Tapering the incident field is also necessary to control spurious edge effects, but as with a real experiment the beam effects on the cross section can be removed. For the data presentation here, however, we work in relative rather than absolute units. The individual data runs required between 8 and 15 minutes of CRAY Y-MP time, although the independent processors were not used in parallel. Parallel processing could be used for more efficient throughput for future Doppler computations where more than 30 computations per surface are needed.

The $U = 10$ m/s data show the same general features as the flat-surface isotropic model; moreover, the differences between the two surface realizations is small within 10 m of the surface reference level, which is the region of interest. The main feature to note is that at the location of the deepest trough where the computation is initiated, the backscatter coefficient is generally near or above the free particle level of ~ -30 dB. Thus, once the bubble cloud is at the depth of the deepest wave trough, it can cause a significant backscatter enhancement over its free-surface value. The incidence-angle dependence acts to lower the cross section at the level of the deepest trough as the incidence angle is increased. Large incidence angles are most relevant to acoustic surface reverberation.

The $U = 15$ m/s data show significantly different details but qualitatively similar behavior. The 60° data evidently are already beyond the first maxima for a flat surface

at the depth of the deepest trough. Because of this, the first rough surface maxima occurs at 10 m below the reference level. At the higher incidence angles, however, the initial surface backscatter point occurs within the envelope of the first maxima of the analytic curve. Once the incidence angle reaches 70°, the principal characteristics of the backscatter enhancement are established.

The $U = 20$ m/s surface realizations have crest-to-trough excursions that exceed the incident wavelength, as can be seen from the surface realization in the reference plots. Such large surface roughness provides a severe test of both the surface-scatter and mutual-interaction codes. We found that we could maintain good energy conservation for the computation of the scattering function representing the surface, but in the ensuing mutual-interaction computation, energy conservation was degraded significantly depending on individual surface realizations. For the $U = 20$ m/s surface realizations shown in this report these errors may be as high as 23%. Surprisingly, however, these errors were confined to the 60° and 70° incidence angles. At 80°, energy was conserved to better than 8%. The relative error of the ratio of the total scattered energy to the incident energy is summarized in Table 1.

Table 1: Relative Energy Conservation Error

	$U = 10$ m/s	$U = 15$ m/s	$U = 20$ m/s
60° incidence	0.03-0.04	0.10–0.13	0.18–0.23
70° incidence	0.01-0.03	0.05–0.08	0.12–0.18
80° incidence	0.01-0.03	0.01–0.05	0.00–0.08

While the $U = 20$ m/s results are somewhat poorer in terms of overall energy conservation, we believe that the main features are correctly represented. We observe much larger variations from realization to realization and significant departures from the simple lobing pattern predicted by the analytic curves we have used for reference. A complete characterization of a small object scattering near such a rough surface clearly demands a statistical characterization, which is beyond the scope of our current effort.

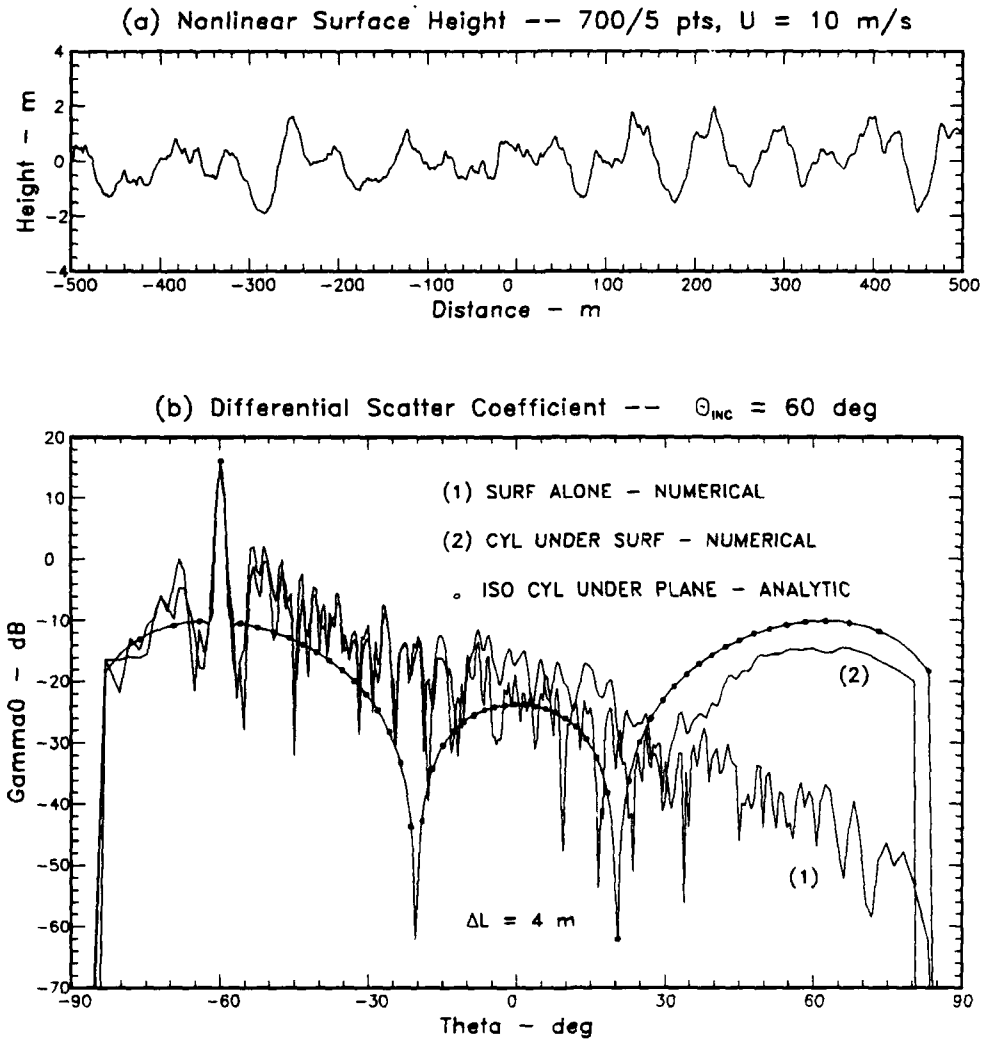

Figure 16: Differential scattering coefficients for $U = 10$ m/s at 60° incidence.

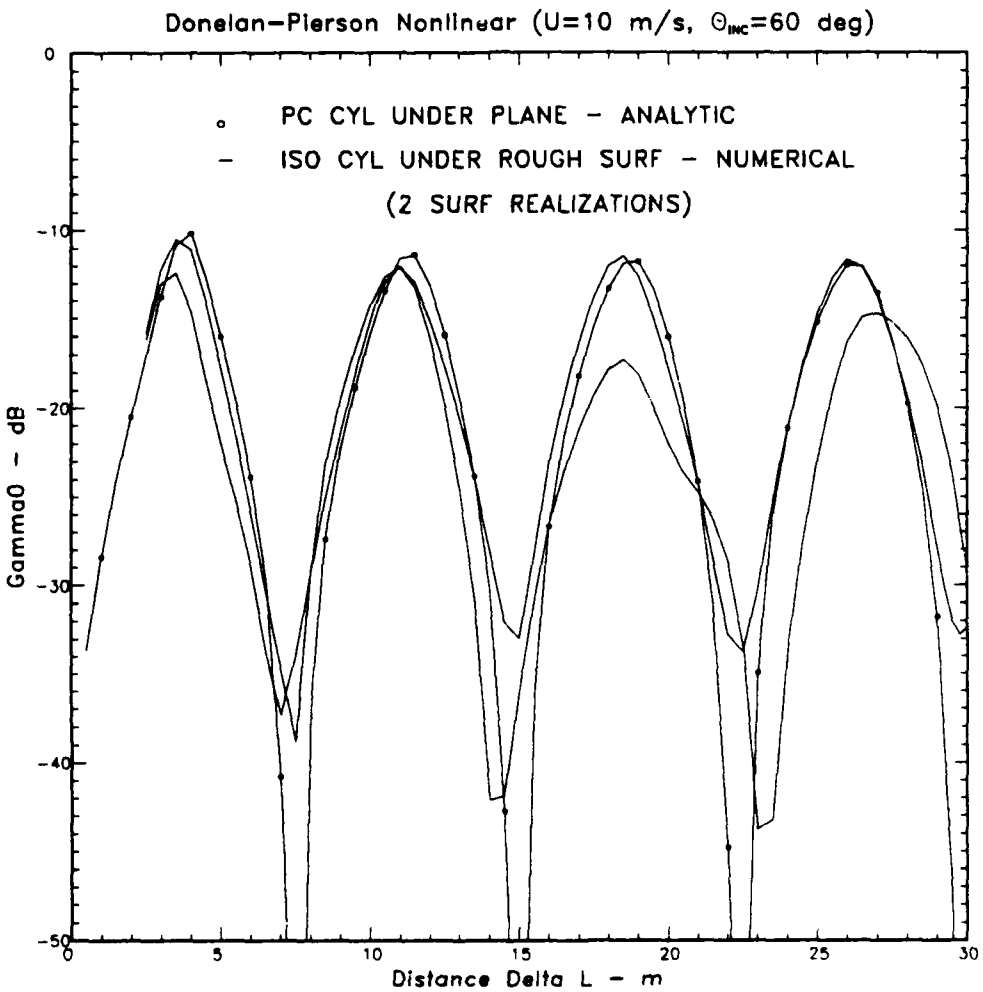

Figure 17: Backscatter cross section as a function of distance for $U = 10$ m/s at 60° incidence.

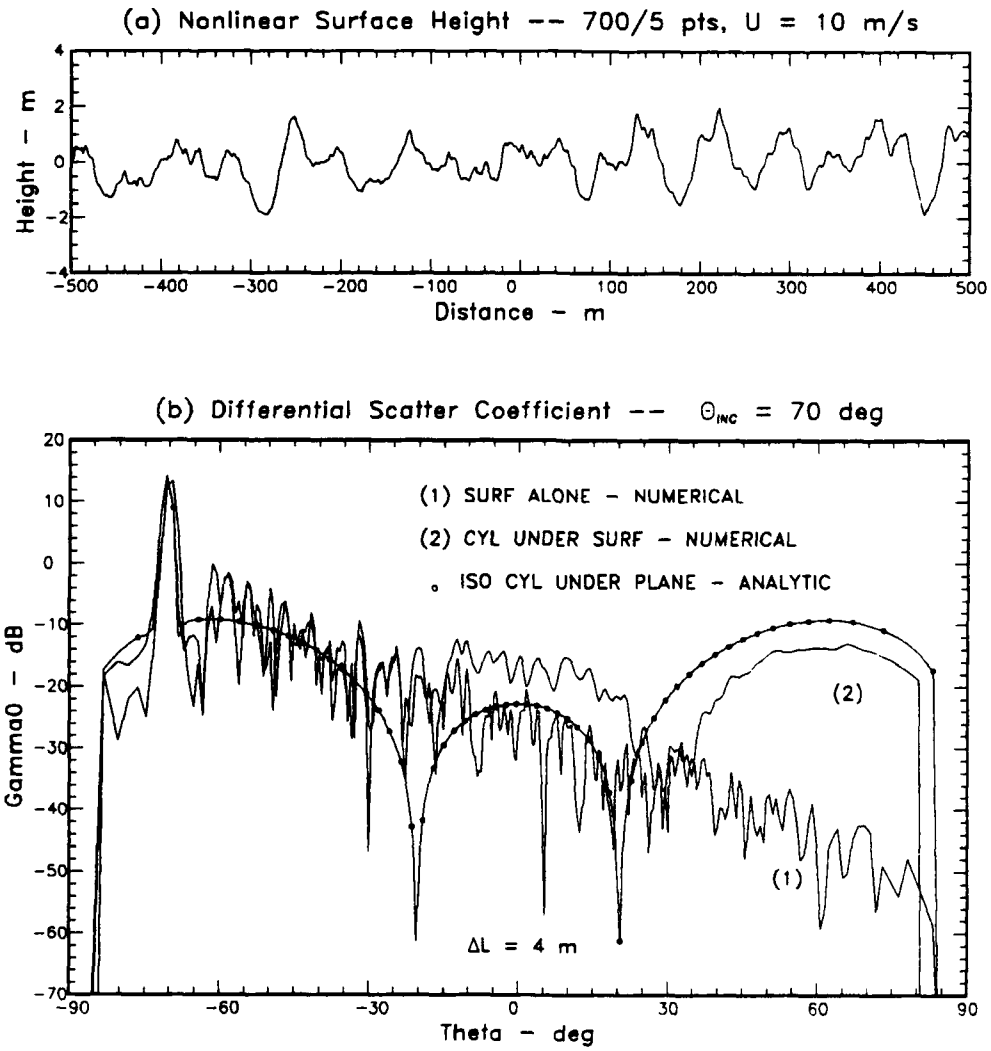

Figure 18: Differential scattering coefficients for $U = 10$ m/s at 70° incidence.

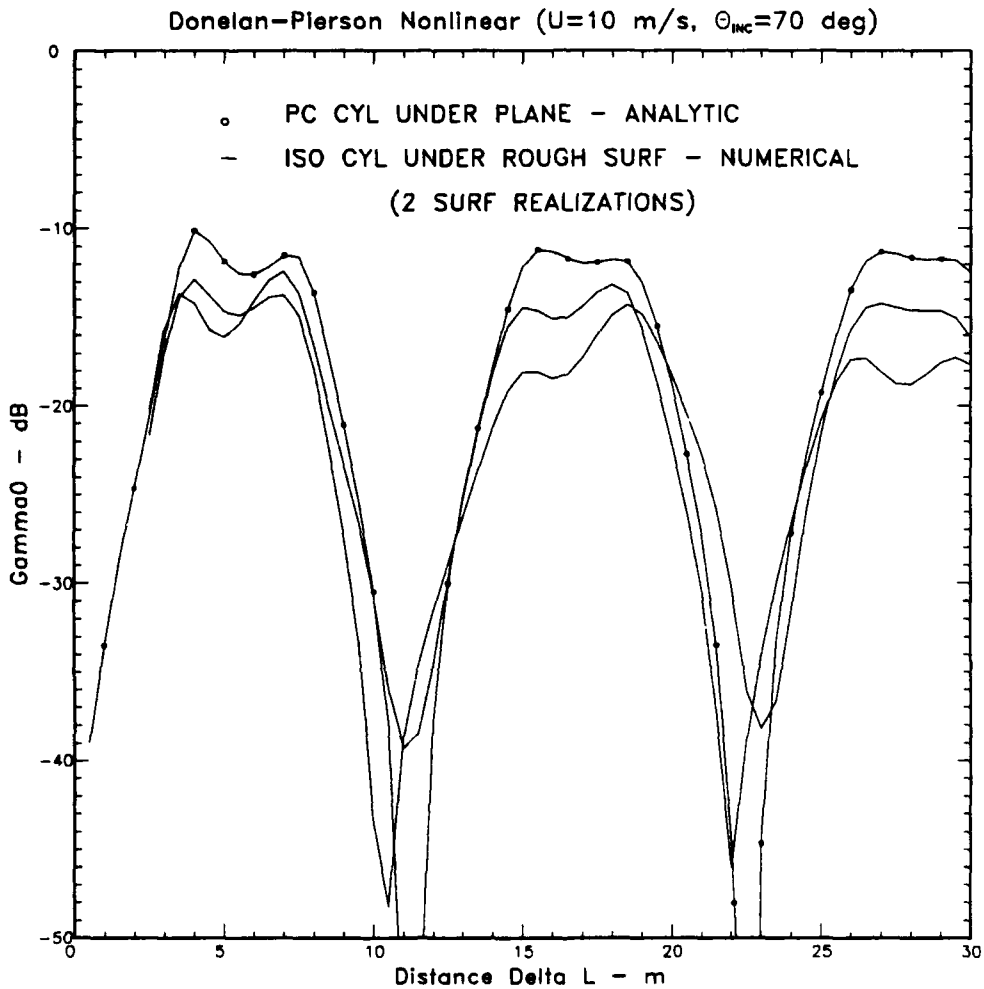

Figure 19: Backscatter cross section as a function of distance for $U = 10$ m/s at 70° incidence.

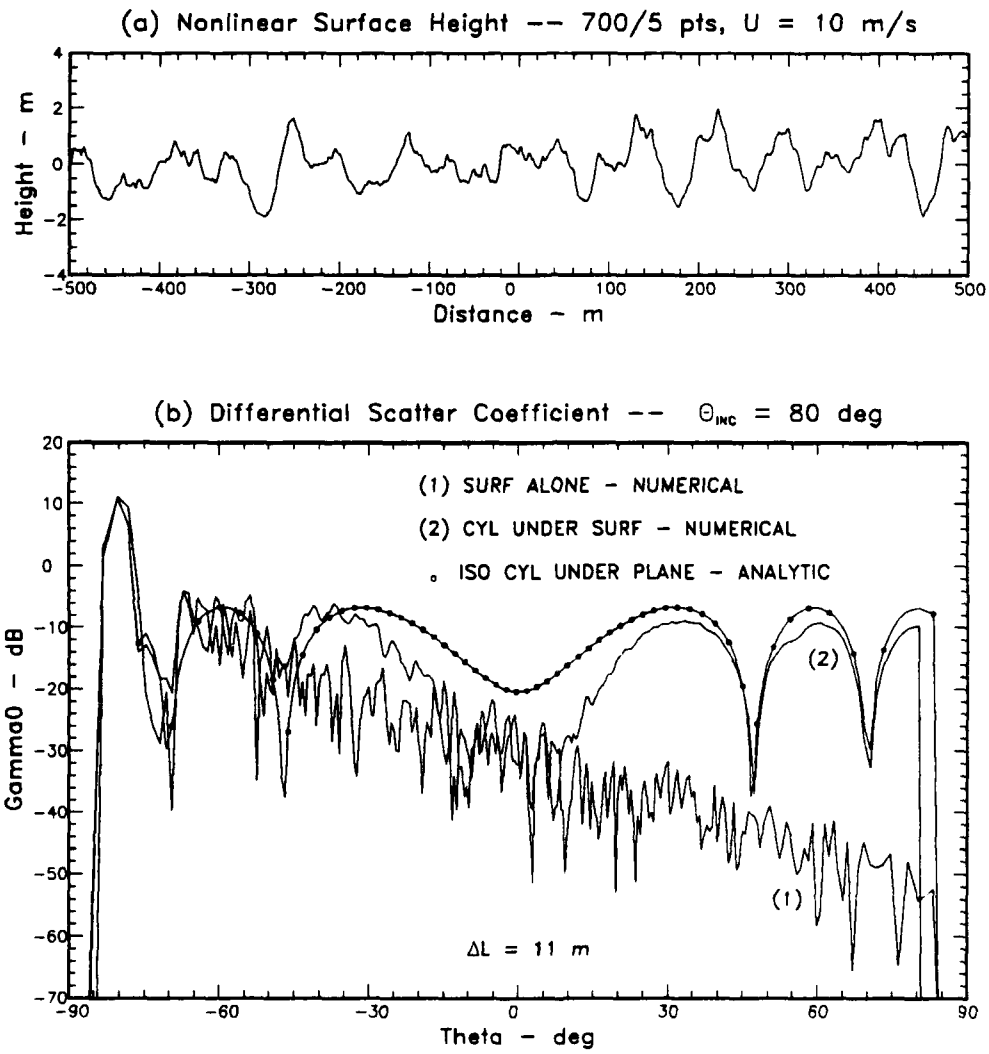

Figure 20: Differential scattering coefficients for $U = 10$ m/s at 80° incidence.

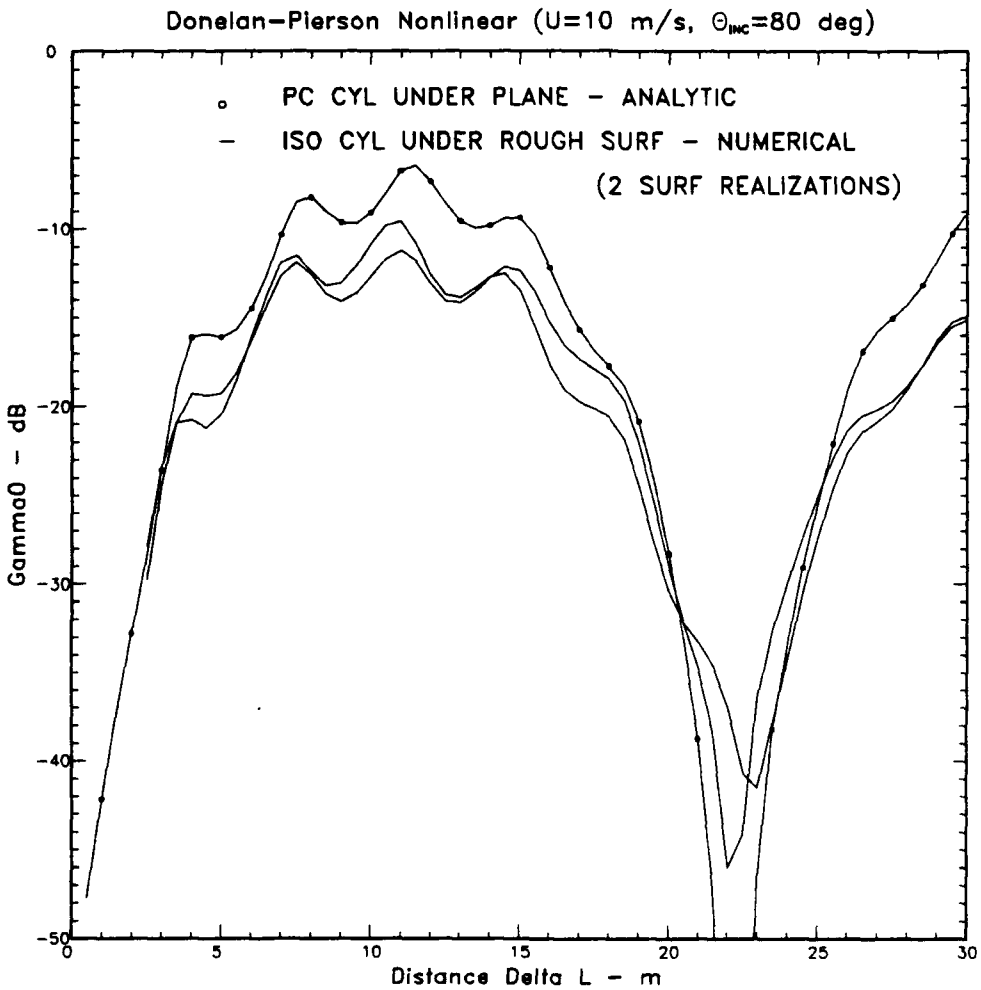

Figure 21: Backscatter cross section as a function of distance for $U = 10$ m/s at 80° incidence.

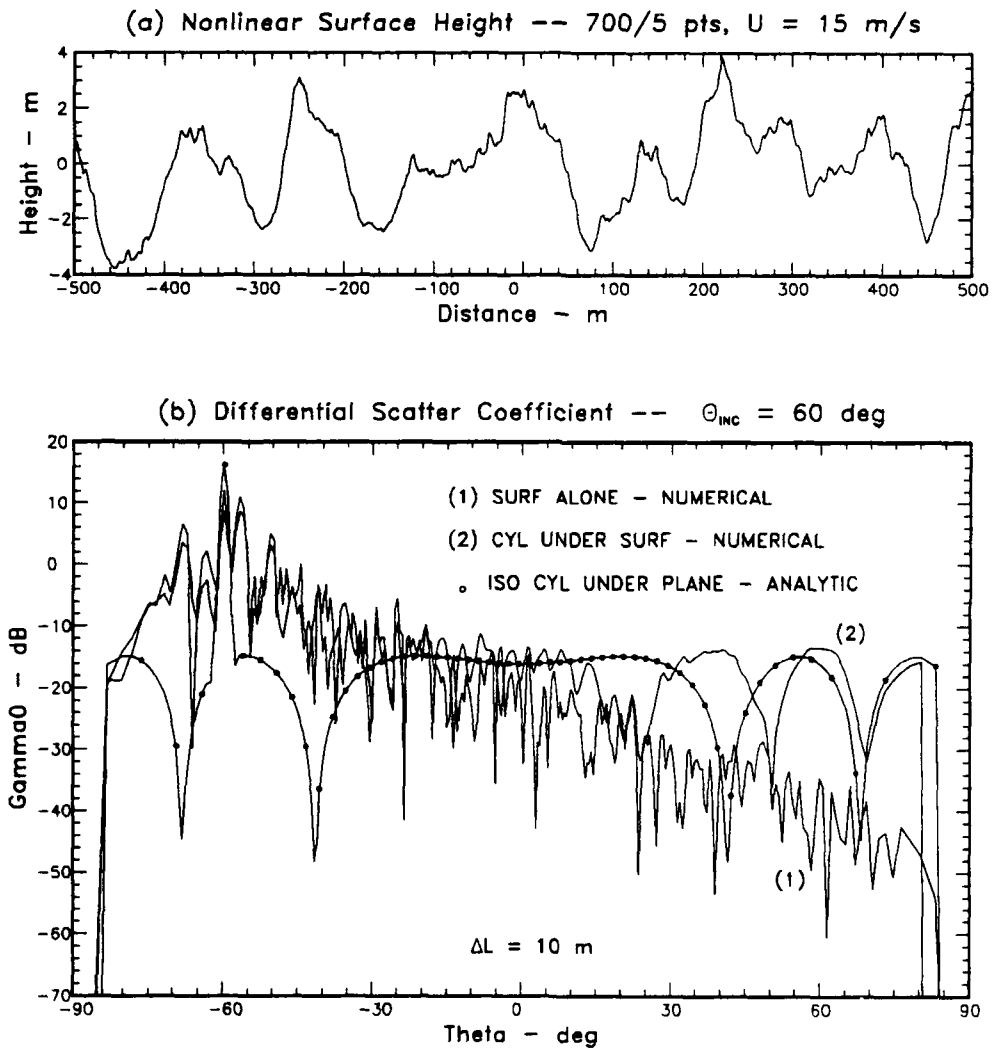

Figure 22: Differential scattering coefficients for $U = 15$ m/s at 60° incidence.

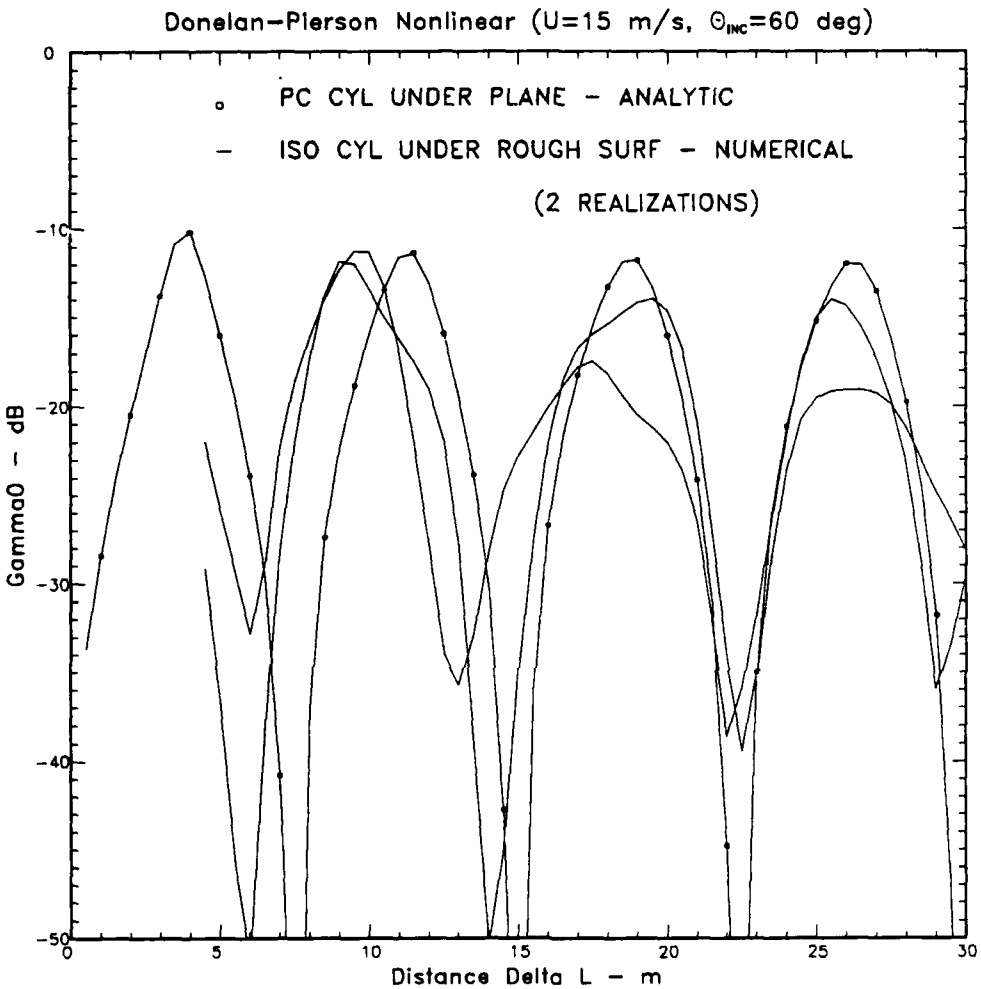

Figure 23: Backscatter cross section as a function of distance for $U = 15$ m/s at 60° incidence.

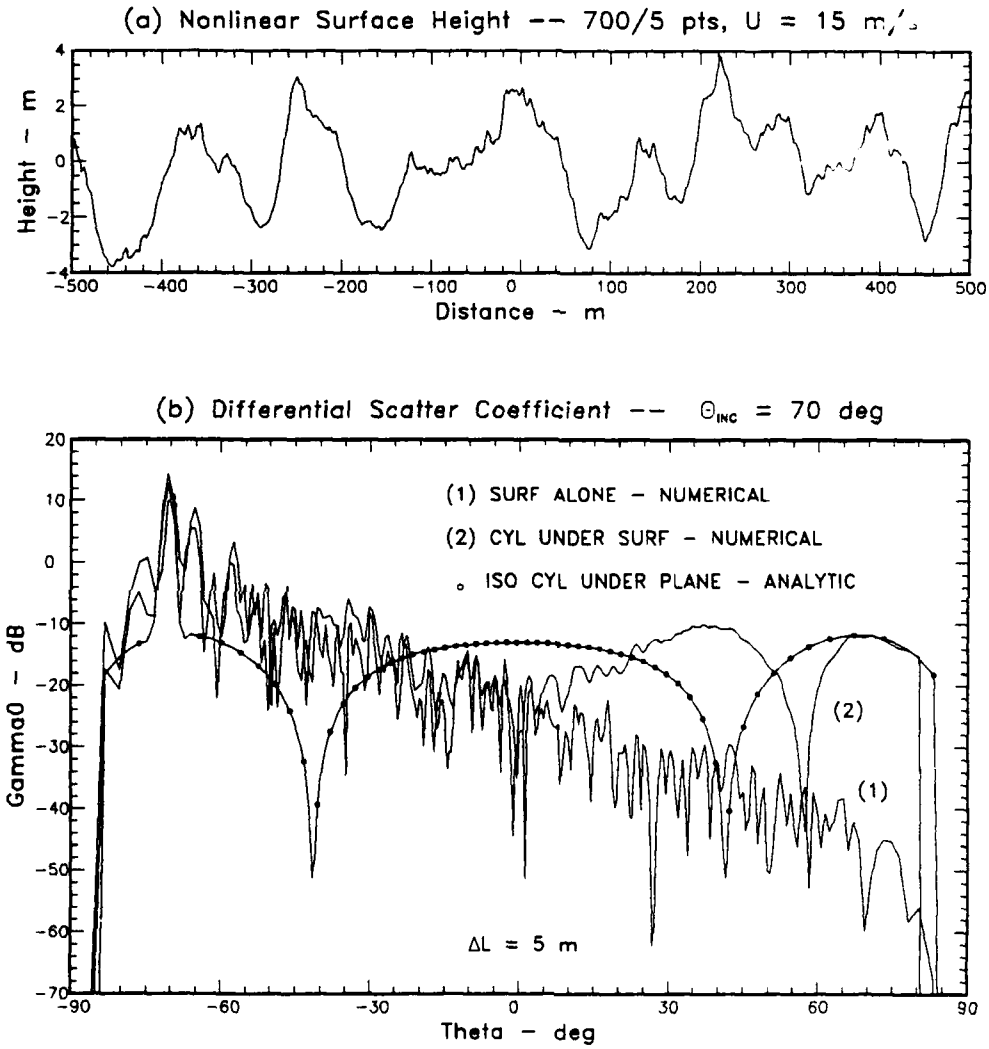

Figure 24: Differential scattering coefficients for $U = 15$ m/s at 70° incidence.

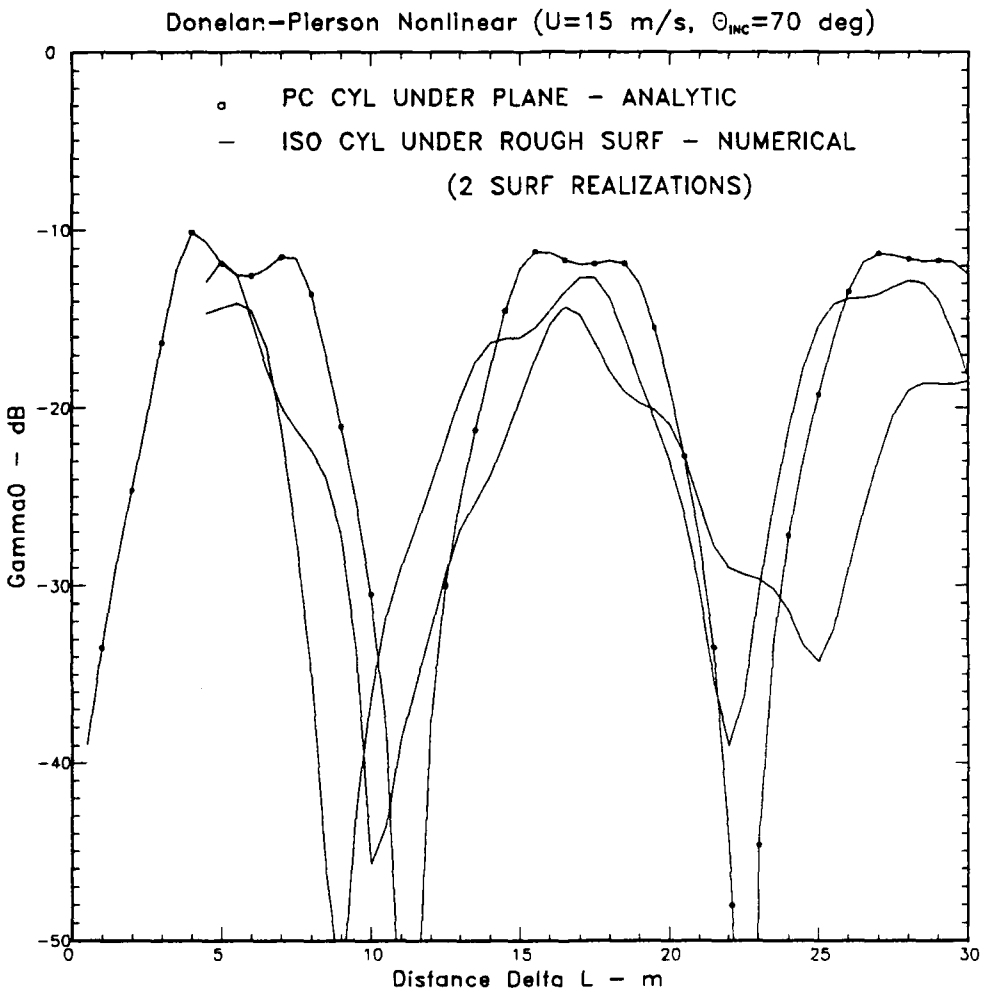

Figure 25: Backscatter cross section as a function of distance for $U = 15$ m/s at 70° incidence.

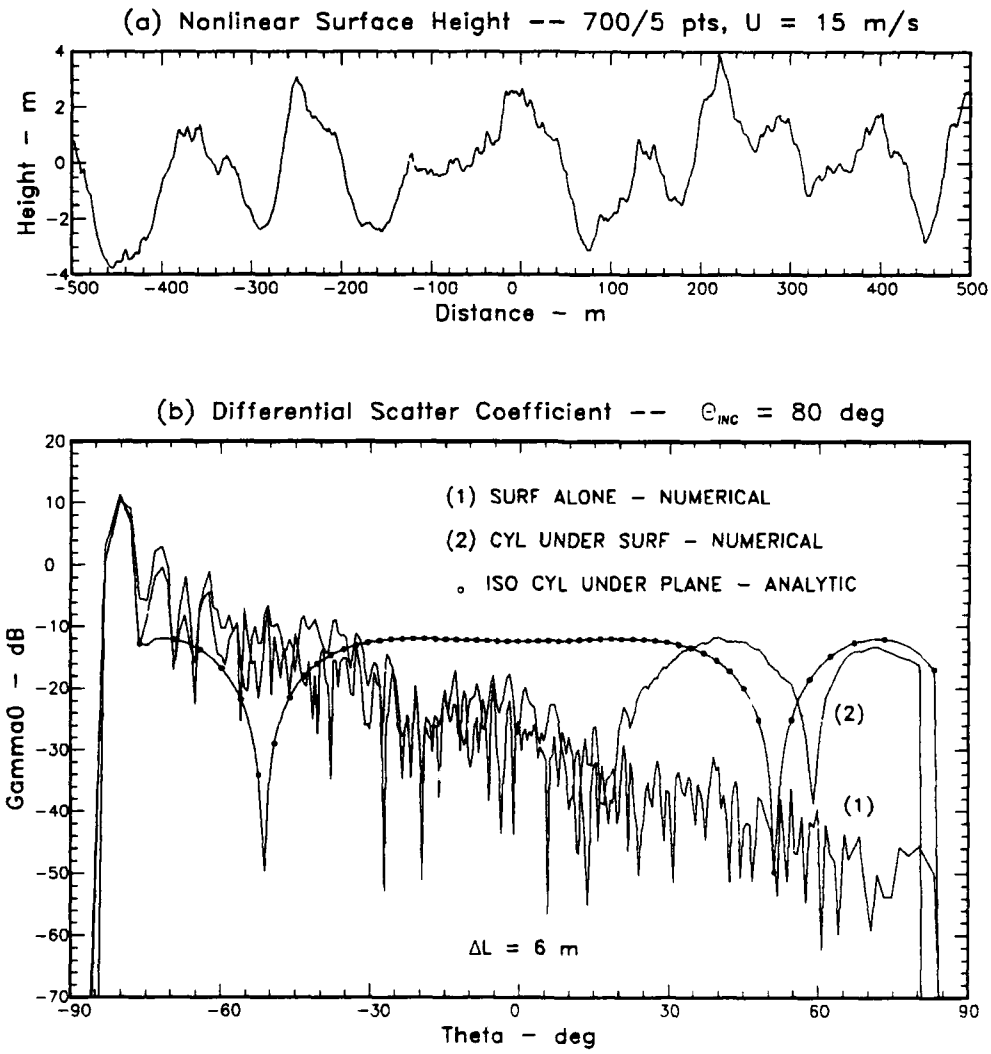

Figure 26: Differential scattering coefficients for $U = 15$ m/s at 80° incidence.

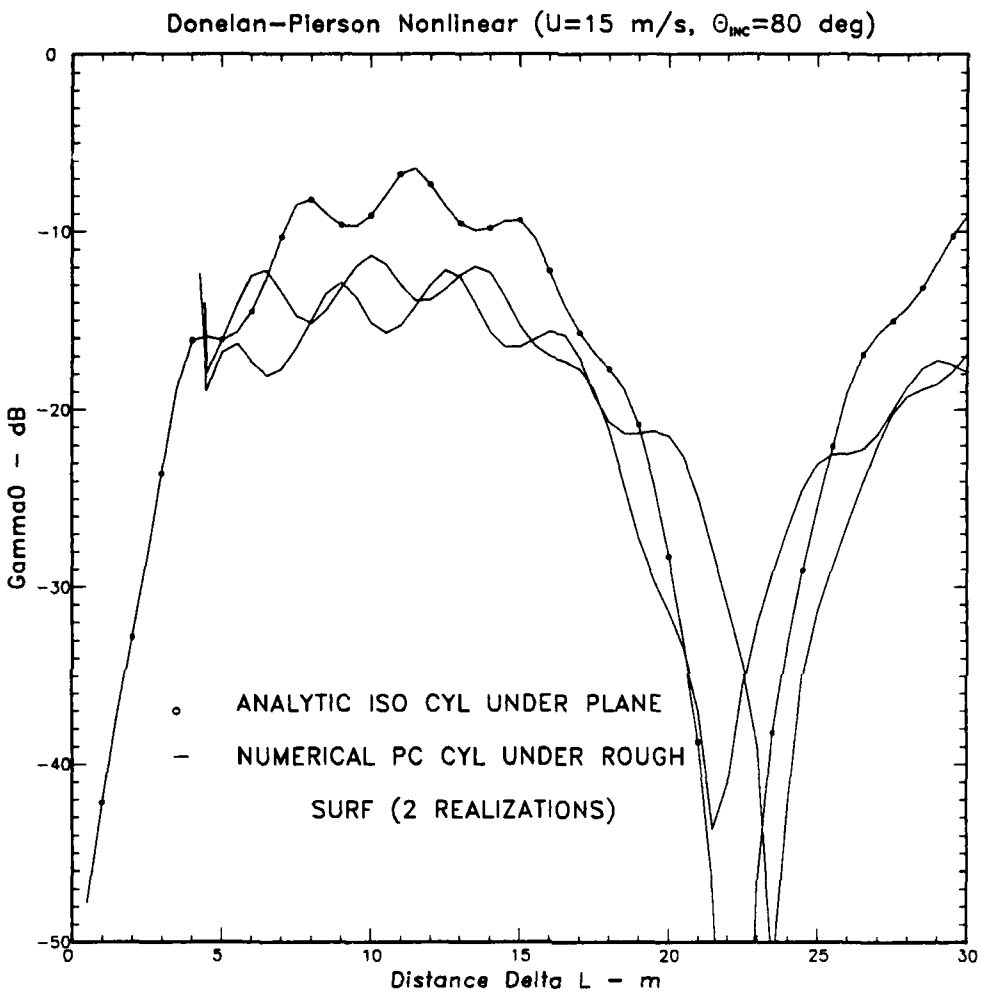

Figure 27: Backscatter cross section as a function of distance for $U = 15$ m/s at 80° incidence.

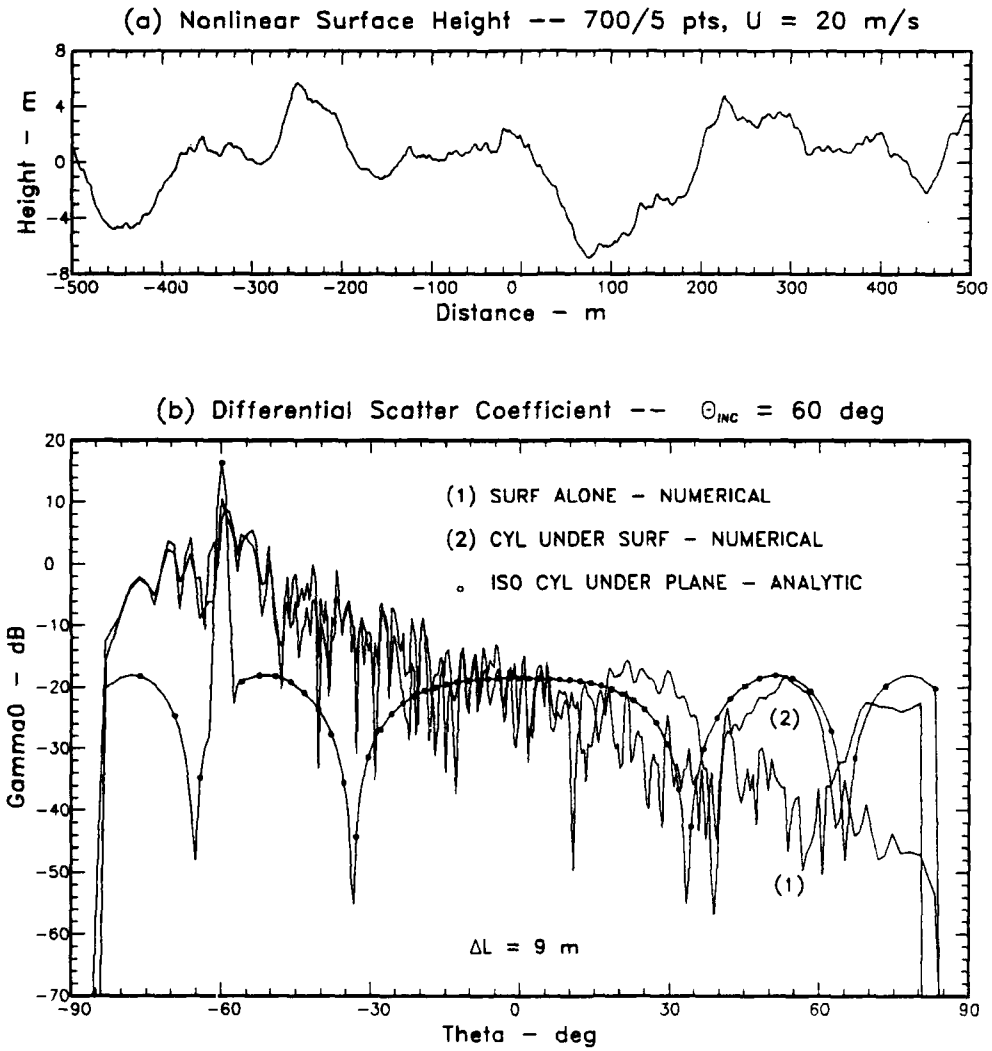

Figure 28: Differential scattering coefficients for $U = 20$ m/s at 60° incidence.

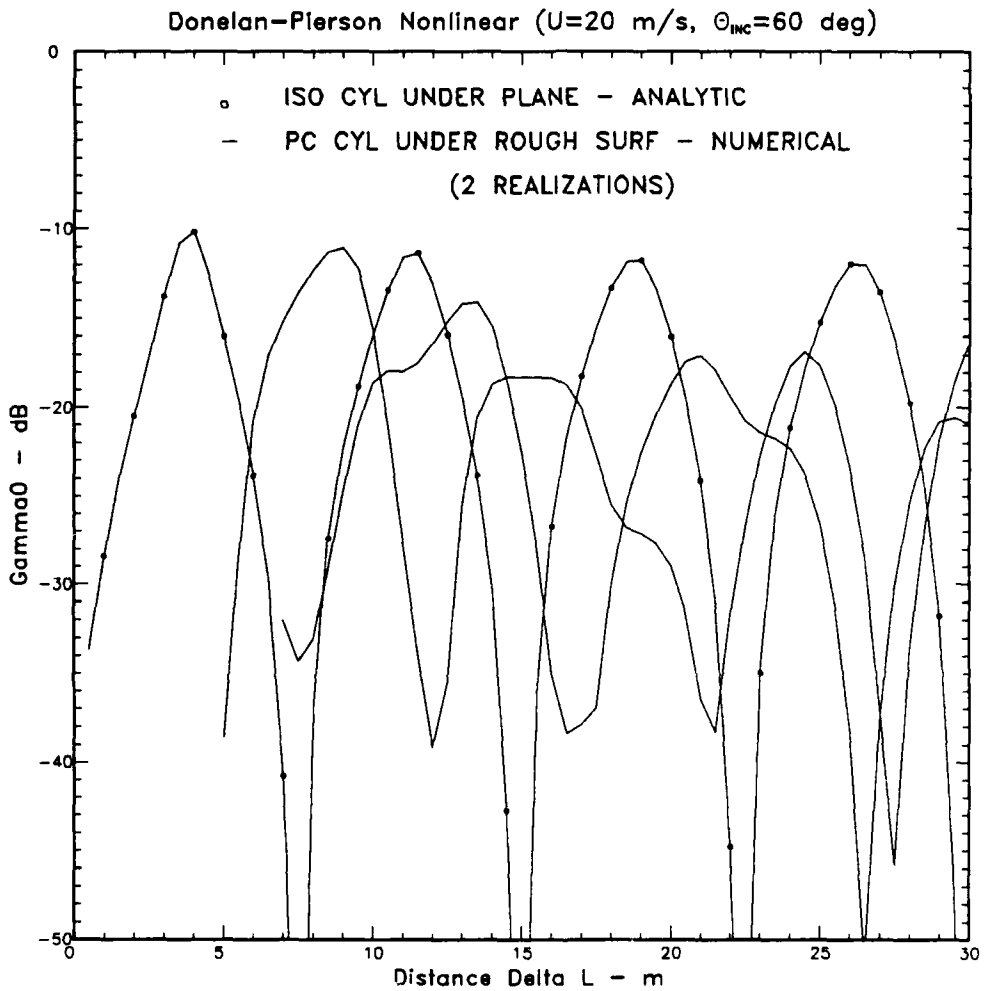

Figure 29: Backscatter cross section as a function of distance for $U = 20$ m/s at 60° incidence.

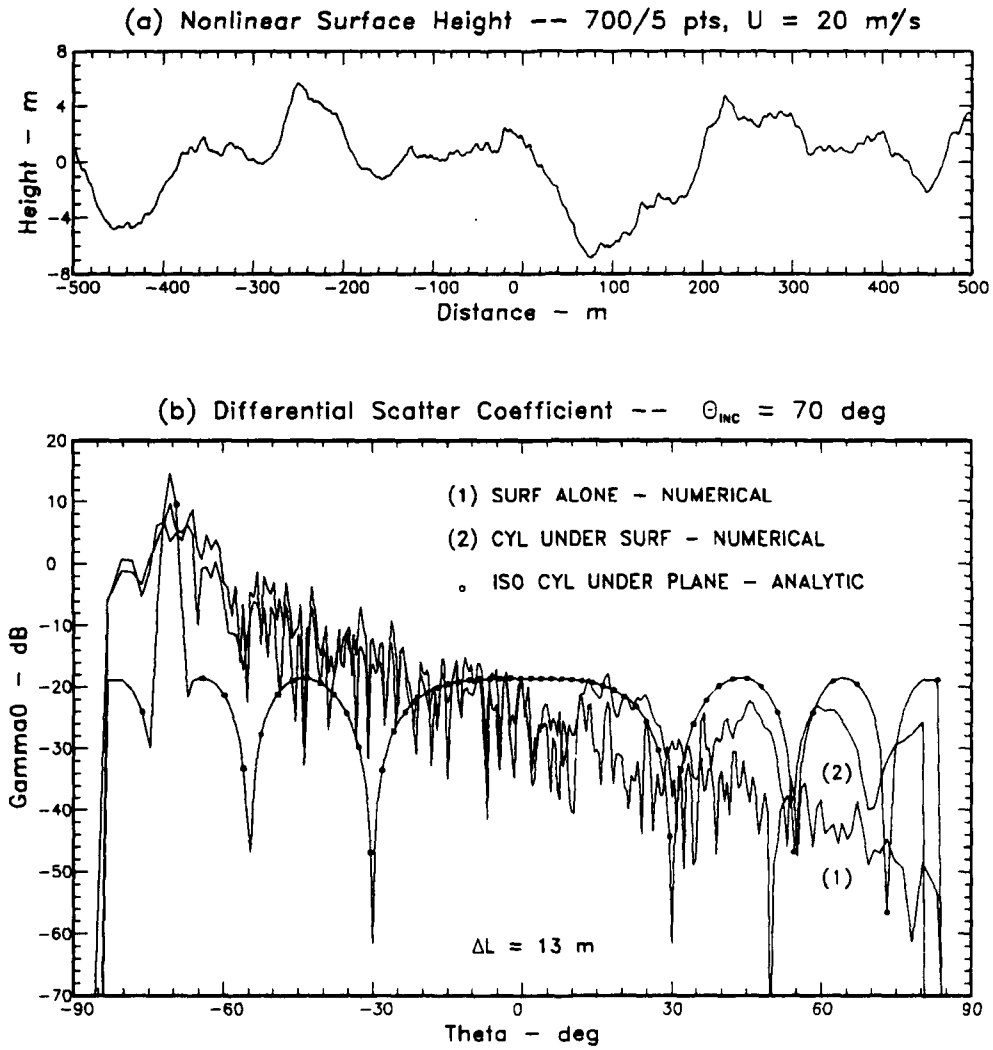

Figure 30: Differential scattering coefficients for $U = 20$ m/s at 70° incidence.

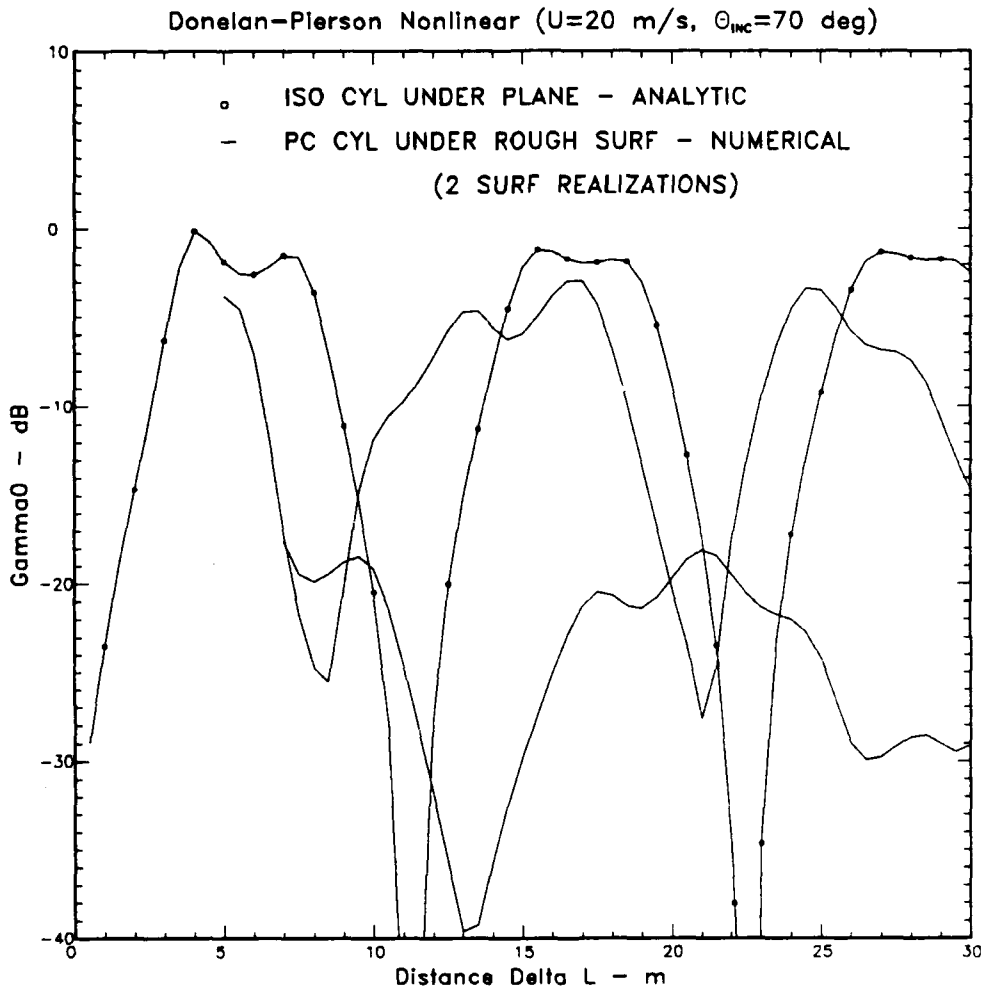

Figure 30: Backscatter cross section as a function of distance for $U = 20$ m/s at 70° incidence.

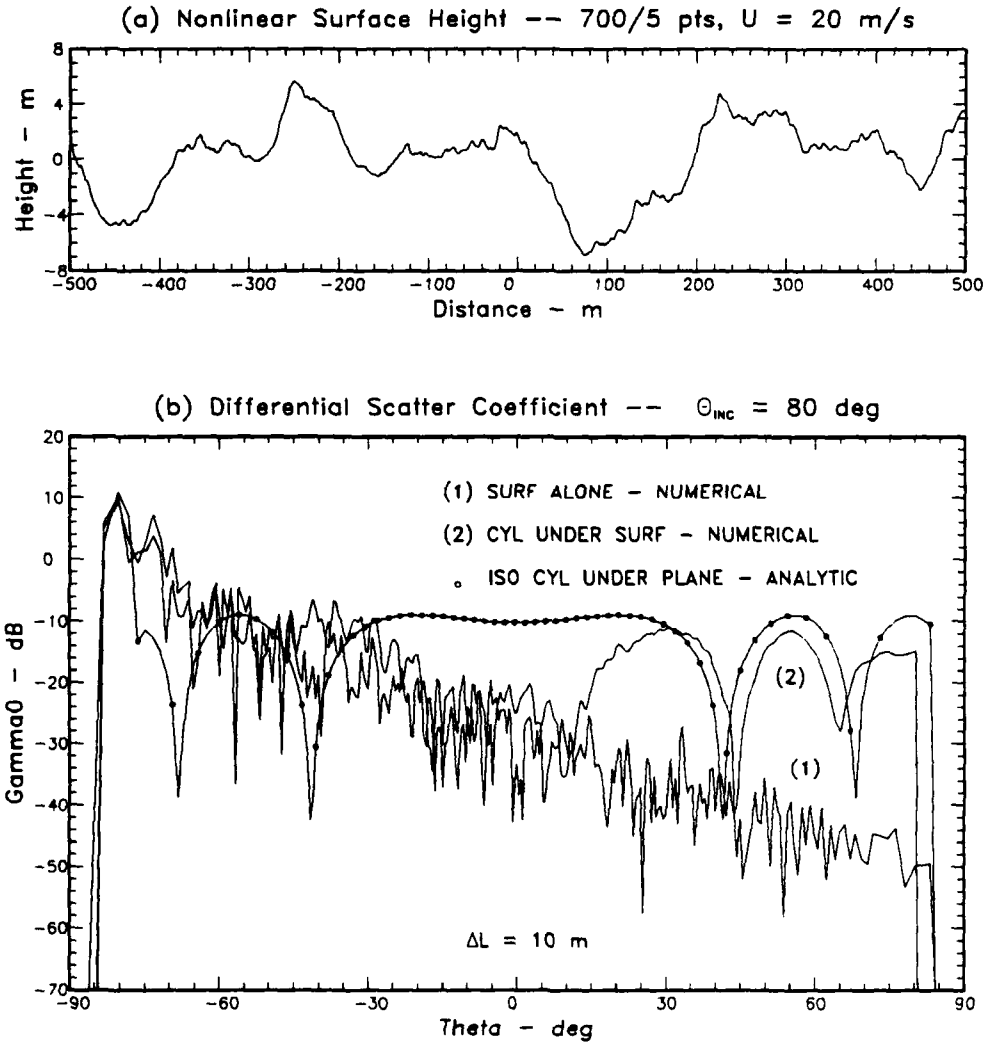

Figure 32: Differential scattering coefficients for $U = 20$ m/s at 80° incidence.

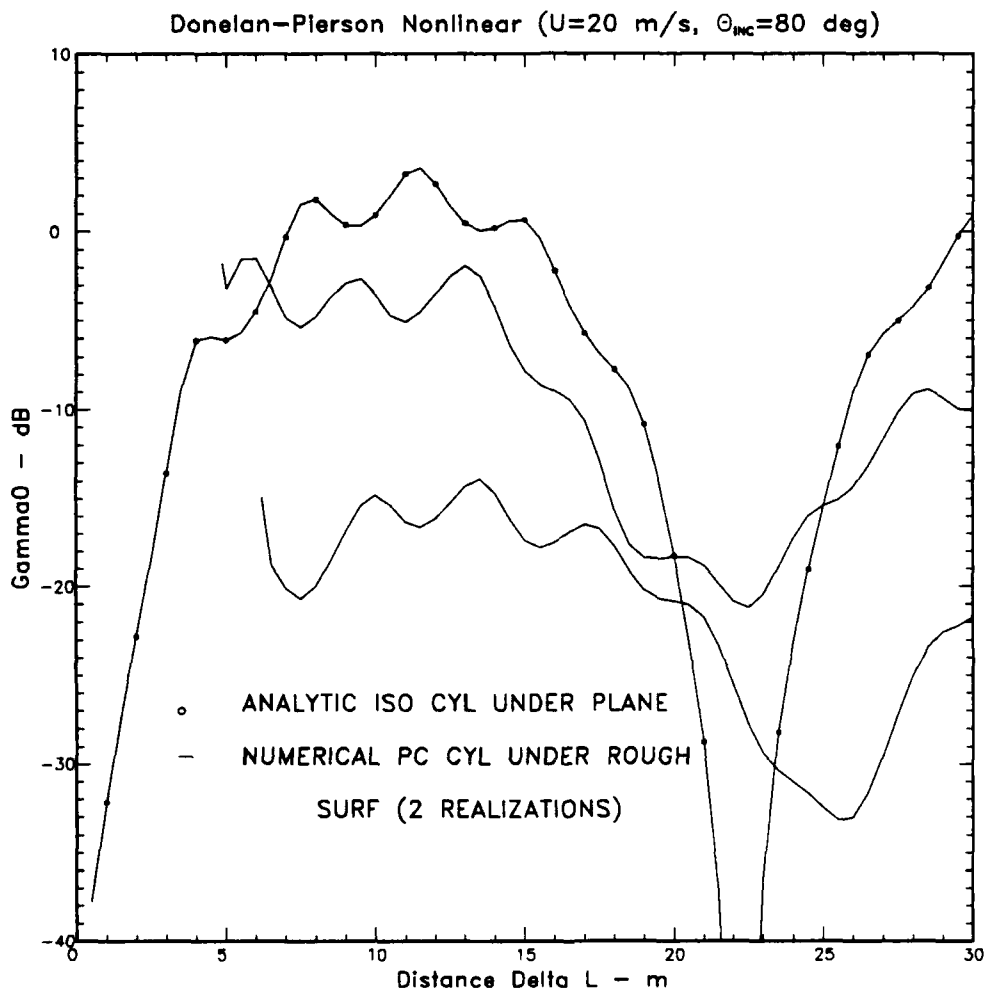

Figure 32: Backscatter cross section as a function of distance for $U = 20$ m/s at 80° incidence.

V Conclusions and Recommendations

In Section III and the appendix we developed the mutual-interac ion method in considerable detail. The solution of (14) characterizes the multiply-scattered wave fields between two arbitrary objects in terms of their wave-wave scattering functions. The equation has the same form as equation (5.3) in [12], which was used to calculate the scattering of a dielectric sphere above a substrate. If the scattering operator defined by (13) is approximated by a matrix, (14) can be solved as linear system, whereupon the scattered fields can be computed from (15), (16), and (17). These fields are identified schematically in Figure 2. To the extent that the scattering functions are known, the mutual-interaction method provides a potentially exact formalism for computing the scattered fields. For isotropic scatterers near a plane reflecting surface, the equations admit algebraic solutions, which are summarized by (35), (36), and (37). The degree to which these equations reproduce the exact solutions for the 1-m cylinder scattering at 200 Hz is shown in Figures 12, 13, and 14. The departures from the exact curves, while significant, are well within other uncertainties in the model. The principal limitation of the isotropic flat surface model is that it does not accommodate wind-induced surface roughness.

To model the scattering characteristics of subsurface bubble clouds in the presence of the highly irregular surfaces that spawn them, we have combined our previously developed techniques for scattering from dynamic nonlinear ocean surfaces with the mutual-interaction method. With the restriction to two dimensions, the simulations remain computationally intensive but within acceptable time/cost allocations of supercomputer resources. As discussed in Section I, we have extracted the simplest possible model of a subsurface bubble cloud that allows us to investigate its scattering characteristics in the presence of a rough surface. We chose a fixed bubble-cloud size independent of wind speed and calculated its scattering characteristics as a function of wind speed, incidence angle, and distance from the surface reference level. These results are summarized in Section IV.

The simulations verify that a nearly impenetrable meter-sized object scattering in the presence of a rough surface can easily account for the anomalous acoustic surface reverberations. Indeed, our backscatter coefficient estimates, relative to the free-surface backscatter coefficient, are much too high. This ratio is easily manipulated, however, by changing the bubble-cloud cross section. Thus, we attribute this discrepancy mainly to the simplicity of the bubble cloud model. The integrity of the model depends more critically on how well it explains the observed wind-speed dependence of the anomalous reverberations. In this regard, a consistent feature has emerged from the simulation summarized in Section IV.

The backscatter coefficient at the level of the deepest trough, where the scatter

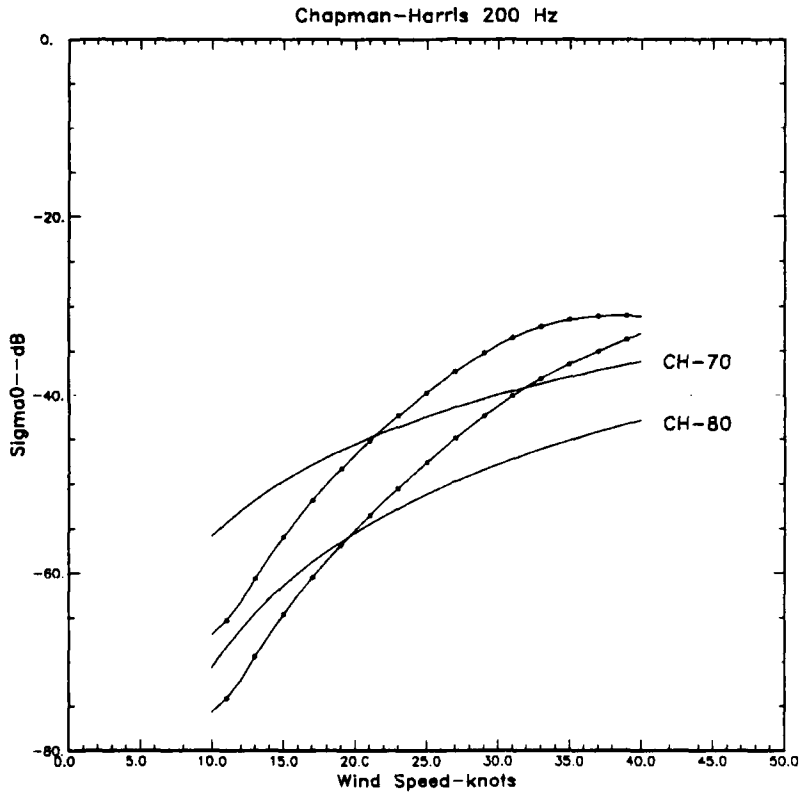

Figure 33: Comparison of Chapman-Harris curves (solid) with wind-independent cloud model (dotted).

calculation is initiated, has the essential characteristics of the Chapman-Harris curves that summarize measured acoustic surface reverberations. We can illustrate this in a simple way by using the flat surface isotropic scatter model. Backscatter strength in this simple model is controlled by a single parameter, namely h_2 in (35). The remaining variable parameters other than wave number are distance from the surface reference level and incidence angle. The two-dimensional model will not reproduce the correct wavelength dependence, but all other aspects of the model are generally consistent with the three-dimensional model. The incidence angle dependence, for example, is identical in the two models. To introduce a wind-speed dependence in the flat-surface equations, we assume that the subsurface bubble population acts in aggregate as a large void only at the depth of the deepest trough. We estimate this depth by using (1). With this hypothesis, the only free parameter in the model is scattering strength. We have adjusted this level to match the Chapman-Harris curve at a wind speed of 20 knots. The results are shown in Figure 34.

The bubble-cloud curves rise too steeply, but a constant bubble-cloud cross section independent of wind speed is certainly unrealistic. We note also that the incidence-angle dependence tends to saturate at the highest wind speed more rapidly than the Chapman-Harris curves. This is most likely due to deficiencies in the isotropic flat-surface model. We believe, however, that the bubble cloud plus rough surface model has the potential to fully explain the observed acoustic surface reverberations. What is needed is a detailed parametric study guided by more information on the observed characteristics of sub-surface bubble clouds, particularly their wind-speed dependence. The simulations can be performed efficiently with modest improvements in the scatter code. At this point in time, the restriction to two dimensions is not severe.

The numerical simulations also have the potential to simulate broad-band signal characteristics. Once appropriate parameters are established, the computations required are straightforward. Here, however, Doppler characteristics are important, and good data management will be required in order for computer resources to be used efficiently. In the course of developing the computer codes our initial effort has necessarily been concentrated overall on computational integrity. With some effort, the simulation codes could be run much more efficiently.

Appendix

The Scattering Function of a Single Scatterer

In this appendix, we describe the method of computing the scattering functions that appear in the mutual-interaction equations discussed in Section III. Consider a time-harmonic electromagnetic field with temporal variation $exp(-i\omega t)$ propagating in an unbounded medium characterized by the wave number k in the presence of a single scatterer. The scatterer is located at the origin and is assumed to be enclosed in a volume V, which is finite in the z direction. The incident wave field scatters from this object, and the total wave field $\mathbf{E}$ can be written as

$$\mathbf{E}(\mathbf{r}) = \mathbf{E}_i(\mathbf{r}) + \mathbf{E}_s(\mathbf{r}), \tag{A1}$$

where $\mathbf{E}_i$ is the incident wave and $\mathbf{E}_s$ the scattered wave. In [10] we showed that the scattered wave field is given by

$$\mathbf{E}_s(\mathbf{r}) = k^2 \iiint_V \underline{\mathbf{G}}(|\mathbf{r} - \mathbf{r}'|)\cdot\mathbf{S}(\mathbf{r}')d\mathbf{r}', \tag{A2}$$

where $\mathbf{S}$ is the equivalent source function, and $\underline{\mathbf{G}}$ is the dyadic outgoing Green's function. Hereafter, dyadics will be distinguished from ordinary vectors by an underline.

The source function is related to the total wave that is impinging on the scatterer, which is the incident wave $\mathbf{E}_i$ for the case under consideration because the medium contains only a single object. The relation is given by

$$\mathbf{S}(\mathbf{r}') = \iiint_V \underline{\mathbf{H}}(\mathbf{r}', \mathbf{r}'')\cdot\mathbf{E}_i(\mathbf{r}'')d\mathbf{r}'', \tag{A3}$$

where $\underline{\mathbf{H}}(\mathbf{r}', \mathbf{r}'')$ is a dyadic that depends on the object's scattering characteristics. It has been shown that $\underline{\mathbf{H}}$ vanishes identically for $\mathbf{r}'$ or $\mathbf{r}''$ outside the object [13].

The dyadic Green's function admits the two-dimensional Fourier decomposition

$$\underline{\mathbf{G}}(|\mathbf{r}-\mathbf{r}'|) = \iint \frac{d\mathbf{K}}{(2\pi)^2}\left\{\frac{i\exp\{ikg(K)|z-z'|\}}{2kg(K)}\underline{\boldsymbol{\kappa}}(\mathbf{K}) - \frac{\delta(z-z')}{k^2}\mathbf{a}_z\mathbf{a}_z\right\} \times \exp\{i\mathbf{K}\cdot(\boldsymbol{\rho}-\boldsymbol{\rho}')\} \qquad (A4)$$

where $\mathbf{r} = \boldsymbol{\rho} + z\mathbf{a}_z$, $\mathbf{a}_z$ is a unit vector along the z axis, $\underline{\mathbf{I}}$ is the unit dyad,

$$g(K) = \begin{cases} [1-(K/k)^2]^{1/2} & \text{if } K \le k \\ i[(K/k)^2-1]^{1/2} & \text{if } K > k \end{cases}, \qquad (A5)$$

$$\underline{\boldsymbol{\kappa}}(\mathbf{K}) = \underline{\mathbf{I}} - k^{-2}\mathbf{k}\mathbf{k}, \qquad (A6)$$

and the propagation vector $\mathbf{k}$ is decomposed as

$$\mathbf{k} = \mathbf{K} + k_z(K)\mathbf{a}_z \equiv \mathbf{K} \pm kg(K)\mathbf{a}_z \qquad (A7)$$

with the upper sign chosen for waves traveling in the positive z axis and the lower sign for waves traveling in the negative z axis. (For evanescent waves, the z direction of propagation is defined as the *attenuation direction* to be consistent with the analytic continuation, which will be discussed later.) For instance, $\underline{\boldsymbol{\kappa}}(\mathbf{K})$ in $(A4)$ is evaluated as $\underline{\boldsymbol{\kappa}}^+ = \underline{\mathbf{I}} - k^{-2}\mathbf{k}^+\mathbf{k}^+$ when the observation point $\mathbf{r}$ is completely to the right of the object, i.e, when $z \ge \max\{z'\}$. The range of integration in $(A4)$ is over all $\mathbf{K}$, and our definition of $g(K)$ insures that each Fourier component in the integrand is an evanescent wave that propagates in the transverse direction and attenuates in both the $\pm z$ directions.

The parameter $g(K)$ was introduced to reflect the fact that we are dealing only with monochromatic waves at a fixed frequency ω. The free space propagation vector $\mathbf{k}$ is thus constrained by the relation $|\mathbf{k}| = k = \omega/c$ where c is the speed of light. Since $\mathbf{k}$ can vary in two dimensions only, a physically realizable monochromatic wave field $\mathbf{E}(\mathbf{r})$ possesses only a standard two-dimensional Fourier transform. Let $\hat{\mathbf{E}}(\mathbf{K};z)$ be the two-dimensional spectrum of this wave field at the plane $z =$ const. It follows that

$$\hat{\mathbf{E}}(\mathbf{K};z) = \hat{\mathbf{E}}(\mathbf{K};z_0)\exp\{ik_z(K)(z-z_0)\} = \hat{\mathbf{E}}(\mathbf{K};z_0)\exp\{ikg(K)|z-z_0|\}, \qquad (A8)$$

where z_0 is a constant. It is helpful to introduce the generalized three-dimensional Fourier transform for the wave field with the help of the Dirac delta function. Explicitly,

$$\hat{\mathbf{E}}(\mathbf{k}^\pm) = \hat{\mathbf{E}}^\pm(\mathbf{K};z=0)\,2\pi\delta(k_z \mp kg(K)), \qquad (A9)$$

where the same notation $\hat{\mathbf{E}}$ denotes either the two- or three-dimensional Fourier transform depending on the context of its argument.

In general, the three-dimensional Fourier decompositions of $\mathbf{E}(\mathbf{r})$ and $\underline{\mathbf{H}}(\mathbf{r}',\mathbf{r}'')$ can be written as

$$\mathbf{E}_i(\mathbf{r}'') = \iiint \frac{d\mathbf{k}'''}{(2\pi)^3}\widehat{\mathbf{E}}_i(\mathbf{k}''')\exp\{i\mathbf{k}'''\cdot\mathbf{r}''\}, \tag{A10}$$

$$\underline{\mathbf{H}}(\mathbf{r}',\mathbf{r}'') = \iiint \frac{d\mathbf{k}'}{(2\pi)^3}\iiint \frac{d\mathbf{k}''}{(2\pi)^3}\widehat{\underline{\mathbf{H}}}(\mathbf{k}',\mathbf{k}'')\exp\{i(\mathbf{k}'\cdot\mathbf{r}' - \mathbf{k}''\cdot\mathbf{r}'')\}. \tag{A11}$$

In the following we are interested in the field outside the scatterer, hence the delta function in the integrand of $(A4)$ does not contribute. Substituting the above quantities into $(A2)$ yields

$$\begin{aligned}\mathbf{E}_s(\mathbf{r}) = {} & \frac{ik}{2}\iiint_V d\mathbf{r}'\iiint_V d\mathbf{r}''\iint\frac{d\mathbf{K}}{(2\pi)^2}\iiint\frac{d\mathbf{k}'}{(2\pi)^3}\iiint\frac{d\mathbf{k}''}{(2\pi)^3}\iiint\frac{d\mathbf{k}'''}{(2\pi)^3}\\ & \times \underline{\boldsymbol{\kappa}}(\mathbf{K})\cdot\widehat{\underline{\mathbf{H}}}(\mathbf{k}',\mathbf{k}'')\cdot\widehat{\mathbf{E}}_i(\mathbf{k}''')\,[g(K)]^{-1}\exp\{\pm i\mathbf{K}\cdot(\boldsymbol{\rho}-\boldsymbol{\rho}')\}\\ & \times\exp\{ikg(K)|z-z'|\}\exp\{i(\mathbf{k}'\cdot\mathbf{r}' - \mathbf{k}''\cdot\mathbf{r}'' + \mathbf{k}'''\cdot\mathbf{r}'')\}.\end{aligned} \tag{A12}$$

The components of $\mathbf{K}$, $\mathbf{k}'$, $\mathbf{k}''$, and $\mathbf{k}'''$ are independent real variables, but the z component of $\mathbf{k}$, k_z, is constrained by the relation $k_z^2 + K^2 = k^2$. In addition, the $\pm$ signs were conveniently introduced in the exponent of $\exp\{i\mathbf{K}\cdot(\boldsymbol{\rho}-\boldsymbol{\rho}')\}$ because $\underline{\mathbf{G}}$ is an even function of $(\boldsymbol{\rho}-\boldsymbol{\rho}')$. Because the integrand vanishes for $\mathbf{r}''$ outside V, we can extend the $\mathbf{r}''$ limits to infinity and perform the integration over $\mathbf{r}''$ and $\mathbf{k}'''$ to obtain

$$\begin{aligned}\mathbf{E}_s(\mathbf{r}) = {} & \frac{ik}{2}\iiint_V d\mathbf{r}'\iint\frac{d\mathbf{K}}{(2\pi)^2}\iiint\frac{d\mathbf{k}'}{(2\pi)^3}\iiint\frac{d\mathbf{k}''}{(2\pi)^3}\,\underline{\boldsymbol{\kappa}}(\mathbf{K})\cdot\widehat{\underline{\mathbf{H}}}(\mathbf{k}',\mathbf{k}'')\cdot\widehat{\mathbf{E}}_i(\mathbf{k}'')\\ & \times[g(K)]^{-1}\exp\{\pm i\mathbf{K}\cdot(\boldsymbol{\rho}-\boldsymbol{\rho}') + ikg(K)|z-z'|\}\exp\{i\mathbf{k}'\cdot\mathbf{r}'\}.\end{aligned} \tag{A13}$$

Upon resolving the absolute value sign, we obtain

$$\begin{aligned}\mathbf{E}_s(\mathbf{r}) = {} & \frac{ik}{2}\iiint_V d\mathbf{r}'\iint\frac{d\mathbf{K}}{(2\pi)^2}\iiint\frac{d\mathbf{k}'}{(2\pi)^3}\iiint\frac{d\mathbf{k}''}{(2\pi)^3}\,\underline{\boldsymbol{\kappa}}(\mathbf{K})\cdot\widehat{\underline{\mathbf{H}}}(\mathbf{k}',\mathbf{k}'')\cdot\widehat{\mathbf{E}}_i(\mathbf{k}'')\\ & \times[g(K)]^{-1}\exp\{i(\mathbf{k}'\pm\mathbf{k}(\mathbf{K}))\cdot\mathbf{r}'\}\exp\{\mp i\mathbf{k}(\mathbf{K})\cdot\mathbf{r}\},\end{aligned} \tag{A14}$$

where the upper sign applies if $z \le z'$ and $k_z \ge 0$ or if $z \ge z'$ and $k_z < 0$, and the lower sign applies if $z \le z'$ and $k_z < 0$ or if $z \ge z'$ and $k_z \ge 0$.

To perform the $\mathbf{r}'$ integration, we further restrict our observation point to the regions outside the slab $a \le z' \le b$ where a and b are the minimum and maximum of the projection of the scatterer onto the z axis. In this case, the above integral can be rewritten in a compact form as

$$\begin{aligned}\mathbf{E}_s(\mathbf{r}) = {} & \frac{ik}{2}\iiint_V d\mathbf{r}'\iint\frac{d\mathbf{K}}{(2\pi)^2}\iiint\frac{d\mathbf{k}'}{(2\pi)^3}\iiint\frac{d\mathbf{k}''}{(2\pi)^3}\,\underline{\boldsymbol{\kappa}}(\mathbf{K})\cdot\widehat{\underline{\mathbf{H}}}(\mathbf{k}',\mathbf{k}'')\cdot\widehat{\mathbf{E}}_i(\mathbf{k}'')\\ & \times\ [g(K)]^{-1}\exp\{i(\mathbf{k}'\pm\mathbf{k}(\mathbf{K}))\cdot\mathbf{r}'\}\exp\{\mp i\mathbf{k}(\mathbf{K})\cdot\mathbf{r}\},\quad z \le a \text{ or } z \ge b.\end{aligned} \tag{A15}$$

where now the choice of sign depends on whether $\mathbf{k}(\mathbf{K})$ is directed away from or toward the origin. In the former case the plus sign is chosen (outgoing waves), and in the latter case the minus sign (incoming waves). The $\mathbf{r}'$, $\mathbf{k}'$ integrations are readily evaluated after the $\mathbf{r}'$ limits are extended to infinity to yield

$$\begin{aligned}\mathbf{E}_s(\mathbf{r}) &= \frac{ik}{2}\iint\frac{d\mathbf{K}}{(2\pi)^2}\iiint\frac{d\mathbf{k}''}{(2\pi)^3}\,\underline{\kappa}(\mathbf{K})\cdot\underline{\widehat{\mathbf{H}}}(\pm\mathbf{k}(\mathbf{K}),\mathbf{k}'')\cdot\widehat{\mathbf{E}}_i(\mathbf{k}'')\\ &\quad\times[g(K)]^{-1}\exp\{\pm i\mathbf{k}(\mathbf{K})\cdot\mathbf{r}\},\qquad z\le a \text{ or } z\ge b. \qquad (A16)\end{aligned}$$

Thus the total scattered wave field at a fixed point $\mathbf{r}$ is a linear superposition of outgoing or incoming plane waves. For finite values of z, both types of waves are physically realizable for a many-scatterer configuration. In the one-scatterer problem under consideration here, only outgoing waves are possible so that the total scattered wave is given by

$$\mathbf{E}_s(\mathbf{r}) = \frac{ik}{2}\iint\frac{d\mathbf{K}}{(2\pi)^2}\iiint\frac{d\mathbf{k}''}{(2\pi)^3}\,\underline{\kappa}(\mathbf{K})\cdot\underline{\widehat{\mathbf{H}}}(\mathbf{k}(\mathbf{K}),\mathbf{k}'')\cdot\widehat{\mathbf{E}}_i(\mathbf{k}'')\frac{\exp\{i\mathbf{k}(\mathbf{K})\cdot\mathbf{r}\}}{g(K)}. \qquad (A17)$$

Since $\widehat{\mathbf{E}}_i$ is a physically realizable monochromatic wave, the relation $(A9)$ applies and the above equation becomes

$$\mathbf{E}_s(\mathbf{r}) = \frac{ik}{2}\iint\frac{d\mathbf{K}}{(2\pi)^2}\iint\frac{d\mathbf{K}''}{(2\pi)^2}\,\underline{\kappa}(\mathbf{K})\cdot\underline{\widehat{\mathbf{H}}}(\mathbf{k}(\mathbf{K}),\mathbf{k}(\mathbf{K}''))\cdot\widehat{\mathbf{E}}_i(\mathbf{K}'';z=0)\frac{\exp\{i\mathbf{k}(\mathbf{K})\cdot\mathbf{r}\}}{g(K)}. \qquad (A18)$$

This formula completely determines the scattered wave field outside the scatterer once the scattering function $\underline{\widehat{\mathbf{H}}}$ is known. The relation is simpler in the Fourier domain. In fact, taking the inverse two-dimensional Fourier transform yields the spectrum of the scattered wave at a plane $z=$ const.,

$$\widehat{\mathbf{E}}_s(\mathbf{K};z) = \frac{ik\exp\{ik_z(\mathbf{K})z\}}{2g(K)}\iint\frac{d\mathbf{K}''}{(2\pi)^2}\,\underline{\kappa}(\mathbf{K})\cdot\underline{\widehat{\mathbf{H}}}(\mathbf{k}(\mathbf{K}),\mathbf{k}(\mathbf{K}''))\cdot\widehat{\mathbf{E}}_i(\mathbf{K}'';z=0). \qquad (A19)$$

Our goal, howeve , is to solve the integral equation $(A18)$ for the scattering function $\underline{\widehat{\mathbf{H}}}$. It can be seen that the scattering function is independent of the choice of the incident wave. Thus we can choose a unit-amplitude incident plane wave of the form

$$\begin{aligned}\mathbf{E}_i(\mathbf{r}) &= \mathbf{a}_i\exp\{i\mathbf{k}_i\cdot\mathbf{r}\} &(A20)\\ \widehat{\mathbf{E}}_i(\mathbf{K}'';z) &= \mathbf{a}_i(2\pi)^2\delta(\mathbf{K}''-\mathbf{K}_i)\exp\{ik_z(K_i)z\}, &(A21)\end{aligned}$$

where $\mathbf{a}_i$ is the unit vector along the direction of $\mathbf{E}_i$, and $\mathbf{k}_i=\mathbf{K}_i+\mathbf{a}_z k_z(K_i)$. The $\mathbf{K}''$ integration in $(A18)$ then yields a simpler integral equation for $\underline{\widehat{\mathbf{H}}}$,

$$\mathbf{E}_s(\mathbf{r}) = \frac{ik}{2}\iint\frac{d\mathbf{K}}{(2\pi)^2}\,\underline{\kappa}(\mathbf{K})\cdot\underline{\widehat{\mathbf{H}}}(\mathbf{k}(\mathbf{K}),\mathbf{k}_i)\cdot\mathbf{a}_i\frac{\exp\{ik_z(\mathbf{K})z\}\exp(i\mathbf{K}\cdot\rho)}{g(K)}. \qquad (A22)$$

Since $\widehat{\underline{\mathbf{H}}}$ is independent of $\mathbf{r}$, the above equation can be solved by evaluating the integral at large r in a fixed direction. Since the condition $z \leq a$ or $z \geq b$ then becomes $|z| \to \infty$, we can evaluate this integral by the method of stationary phase to obtain

$$\mathbf{E}_s(\mathbf{r}) \sim \begin{cases} ik^2\, \underline{\boldsymbol{\kappa}}(\mathbf{K}_s)\cdot\widehat{\underline{\mathbf{H}}}(\mathbf{k}_s, \mathbf{k}_i)\cdot\mathbf{a}_i\ \exp\{i(kr - \pi/4)\}/\sqrt{8\pi kr} & \text{2-dim} \\ -k^2\, \underline{\boldsymbol{\kappa}}(\mathbf{K}_s)\cdot\widehat{\underline{\mathbf{H}}}(\mathbf{k}_s, \mathbf{k}_i)\cdot\mathbf{a}_i\ \exp(ikr)/(4\pi r) & \text{3-dim} \end{cases} \tag{A23}$$

where $\mathbf{k}_s$ denotes the scattered wave normal vector directed along $\mathbf{r}$ (i.e., $\mathbf{k}_s = k\mathbf{a}_r$), and $\mathbf{K}_s$ is its transverse.

Note that the condition $|z| \to \infty$ excludes the case $g(K_s) \neq 0$ from the above results. Although the above result was derived from the argument of physical realizability, it is valid for all cases listed in ($A15$). In fact, we can derive this result independently for each of the four cases using the method of stationary phase. Thus, the scattering function is completely determined by the far-field behavior of the scattered wave.

The scattering function is also related to the angular spectrum of the scattered waves at a reference plane $z = z_0$ outside the scatterer. To see this, we need to evaluate the diffraction integral

$$\mathbf{E}_s(\mathbf{r}) = \iint \frac{d\mathbf{K}}{(2\pi)^2} \widehat{\mathbf{E}}_s(\mathbf{K}; z_0) \exp\{ik_z(K)(z - z_0)\} \exp(i\mathbf{K}\cdot\boldsymbol{\rho}) \tag{A24}$$

by the method of stationary phase for large z. The result is

$$\mathbf{E}_s(\mathbf{r}) \sim \begin{cases} kg(K_s)\widehat{\mathbf{E}}_s(\mathbf{K}_s) \exp\{i(kr - \pi/4)\}/\sqrt{2\pi kr} & \text{2-dim} \\ ikg(K_s)\widehat{\mathbf{E}}_s(\mathbf{K}_s) \exp(ikr)/(2\pi r) & \text{3-dim} \end{cases} \tag{A25}$$

where $\widehat{\mathbf{E}}_s(\mathbf{K}_s)$ is a fictitious spectral function defined by

$$\widehat{\mathbf{E}}_s(\mathbf{K}_s) \equiv \widehat{\mathbf{E}}_s(\mathbf{K}_s; z_0) \exp\{-ik_z(\mathbf{K}_s)z_0\}. \tag{A26}$$

Thus, we obtain the following exact relationship for both two and three dimensions:

$$\underline{\boldsymbol{\kappa}}^{\pm}(\mathbf{K}_s)\cdot\widehat{\underline{\mathbf{H}}}(\mathbf{k}^{\pm}(\mathbf{K}_s), \mathbf{k}_i)\cdot\mathbf{a}_i(\mathbf{k}_i) = 2g(K_s)\widehat{\mathbf{E}}_s^{\pm}(\mathbf{K}_s)/(ik), \quad |\mathbf{K}_s| \neq k \tag{A27}$$

where for clarity the superscript $\pm$ has been appended and the dependence of $\mathbf{a}_i$ has been added. Since the above relation is in the Fourier domain, it is understood that the unit vector $\mathbf{a}_i(\mathbf{k}_i)$ characterizes the direction of polarization of one particular Fourier component $\mathbf{k}_i$.

Although $\widehat{\mathbf{E}}_s(\mathbf{K}_s)$ seems to be a two-dimensional Fourier transform of the wave field along the plane $z = 0$, it is physically not. It is obtained by propagating the

physical scattered wave $\widehat{\mathbf{E}}_s(\mathbf{K}_s; z_0)$ from the plane $z = z_0$ back to the plane $z = 0$ as if the scatterer were absent. Equivalently, the scattered wave $\widehat{\mathbf{E}}_s(\mathbf{K}_s; z_0)$ appears as if it were generated from a single scattering plane located at $z = 0$. Thus, in the two-dimensional Fourier domain an object can be replaced by a transverse plane with the same scattering characteristics. For this reason two physically different scatterers are considered identical if they produce the same spectrum of scattered waves for the same incident wave.

For numerical applications it is convenient to introduce a vector version of the scattering function defined by the relation

$$\widehat{\mathbf{W}}_{\mathbf{a}_i}(\mathbf{K}_s, \mathbf{K}_i) \equiv \frac{2g(K_s)}{ik} \underline{\kappa}(\mathbf{K}_s) \cdot \underline{\widehat{\mathbf{H}}}(\mathbf{k}(\mathbf{K}_s), \mathbf{k}(\mathbf{K}_i)) \cdot \mathbf{a}_i(\mathbf{k}(\mathbf{K}_i)), \quad |\mathbf{K}_s| \neq k. \qquad (A28)$$

The scattering vector function $\widehat{\mathbf{W}}_{\mathbf{a}_i}$ is the two-dimensional spectrum of the scattered waves produced by a unit-amplitude incident plane wave polarized in the direction $\mathbf{a}_i$. The scatterer is completely characterized by the scattering dyadic $\underline{\widehat{\mathbf{H}}}$ or, equivalently, three scattering vectors $\widehat{\mathbf{W}}$ associated with three orthogonal directions.

In summary, we have derived an expression for the scattering function which is valid for $g(K_s) \neq 0$. The case where $g(K_s) = 0$ can be handled rigorously by including the $\delta(z - z')$ term of $(A4)$ in the calculations from $(A12)$ to $(A22)$ so that the results will be valid for all z. We will, however, present a short-cut method below.

Determine the Scattering Function for Transverse Propagation

First, note that $\underline{\widehat{\mathbf{H}}}$ is strictly a function of the propagation vectors $\mathbf{k}_s$, $\mathbf{k}_i$, and is therefore coordinate-independent. To determine $\underline{\widehat{\mathbf{H}}}$ for $\mathbf{k}_s \perp \mathbf{a}_z$, we can rotate the coordinates (x, y, z) to the new coordinates $(\tilde{x}, \tilde{y}, \tilde{z})$ about the y axis through an angle θ. The projection of $\mathbf{r}$ onto the new $\tilde{z}$ axis is no longer zero, and the stationary phase result $(A23)$ applies with $\mathbf{K}_s$ replaced by $\widetilde{\mathbf{K}}_s$, i.e.,

$$\underline{\kappa}(\widetilde{\mathbf{K}}_s) \cdot \underline{\widehat{\mathbf{H}}}(\mathbf{k}_s, \mathbf{k}_i) \cdot \mathbf{a}_i \sim -k^{-2} \mathbf{E}_s(\mathbf{r}) \times \begin{cases} \sqrt{8\pi kr} \exp\{-i(kr - 3\pi/4)\} & \text{2-dim} \\ 4\pi r \exp(-ikr) & \text{3-dim} \end{cases}, \qquad (A29)$$

which is valid for $\mathbf{k}_s(\widetilde{\mathbf{K}}_s)$ not perpendicular to the $\tilde{z}$ axis. Since $\widetilde{\mathbf{K}}_s$ is related to $\mathbf{K}_s$ by a simple coordinate rotation, the scattering function at $\mathbf{k}_s(\mathbf{K}_s) \perp \mathbf{a}_z$ can be obtained when we appropriately evaluate the above equation. Since the coordinate transformation is continuous in θ and all the propagation vectors are fixed in $(A29)$, we simply take the

limit as $\theta \to 0$. This is equivalent to taking the limit of $(A23)$ as $\mathbf{r} \to r\mathbf{a}_\rho$. The result is

$$\underline{\kappa}(k\mathbf{a}_\rho)\cdot\underline{\widehat{\mathbf{H}}}(k\mathbf{a}_\rho, \mathbf{k}_i)\cdot\mathbf{a}_i \sim -k^{-2}\mathbf{E}_s(r\mathbf{a}_\rho) \times \begin{cases} \sqrt{8\pi kr}\exp\{-i(kr - 3\pi/4)\} & \text{2-dim} \\ 4\pi r\exp(-ikr) & \text{3-dim} \end{cases}, \tag{A30}$$

where $\mathbf{a}_\rho$ is a unit vector along the transverse direction.

It is important to explore the analyticity of $\underline{\widehat{\mathbf{H}}}$ in the variable $\mathbf{K}_s$. The right hand side of $(A29)$, with $\widetilde{\mathbf{K}}_s$ set to $\mathbf{K}_s$, is bounded if the scattered wave field falls off with distance no less fast than a radiation field. We will assume this is generally the case. (There are exceptions such as scattering from an infinite, perfectly conducting surface.) Since the above scattered wave field was derived for an incident *plane wave*, which is an entire function in $\mathbf{r}$, it is analytic in any homogeneous region such as the far zone. Rotating $\mathbf{r}$ through all but transverse directions, which amounts to varying $\mathbf{K}_s$, we can see that $\underline{\widehat{\mathbf{H}}}$ is analytic in $\mathbf{K}_s$ except on the circle $|\mathbf{K}_s| = k$. The behavior of $\mathbf{E}_s(\mathbf{r})$, hence $\underline{\widehat{\mathbf{H}}}$, on this circle can be inferred from $(A22)$. In fact, each point $\mathbf{K}_s$ on this circle is a pole and branch point of $\mathbf{E}_s(\mathbf{r})$. Equivalently, the point $k_{sz} = 0$ is a pole and branch point when $\mathbf{E}_s(\mathbf{r})$ is viewed as a function of k_{sz}.

The compact notation $\underline{\widehat{\mathbf{H}}}(\mathbf{k}', \mathbf{k}'')$ introduced in $(A11)$ stands for $\underline{\widehat{\mathbf{H}}}(\mathbf{K}', k_z', \mathbf{K}'', k_z'')$ where each variable was independent and was allowed to take any real value. However, what we have obtained in $(A23)$ are the function $\underline{\widehat{\mathbf{H}}}$ defined on the shell $|\mathbf{k}_s| = |\mathbf{k}_i| = k$ in the $\mathbf{k}$ space so that the second- and the fourth-slot variables are no longer independent variables. Sometimes, to emphasize this fact, we write $\underline{\widehat{\mathbf{H}}}(\mathbf{k}_s, \mathbf{k}_i)$ explicitly as $\underline{\widehat{\mathbf{H}}}(\mathbf{K}_s, k_{sz}(\mathbf{K}_s), \mathbf{K}_i, k_{iz}(\mathbf{K}_i))$. Fortunately this special form is the most frequently encountered in our applications. For simplicity, we sometimes drop the dependent variables and write $\underline{\widehat{\mathbf{H}}}(\mathbf{K}_s, \mathbf{K}_i)$. However, this notation is ambiguous since to each value $\mathbf{K}_i$ correspond two incident wave normal vectors $\mathbf{k}_i^\pm = \mathbf{K}_i \pm kg(K_i)\mathbf{a}_z$ where the $\pm$ sign refers to the $\pm z$ direction of propagation. Similarly, there are two scattered wave normal vectors $\mathbf{k}_s^\pm = \mathbf{K}_s \pm kg(K_s)\mathbf{a}_z$. Thus, the short notation $\underline{\widehat{\mathbf{H}}}^{\pm\pm}$ or $\underline{\widehat{\mathbf{H}}}(\mathbf{K}_s^\pm, \mathbf{K}_i^\pm)$ can be used to unambiguously denote the four scattering functions $\underline{\widehat{\mathbf{H}}}(\mathbf{K}_s, \pm kg(K_s), \mathbf{K}_i, \pm kg(K_i))$. The scattering functions $\underline{\widehat{\mathbf{H}}}^{++}$ and $\underline{\widehat{\mathbf{H}}}^{--}$ characterize the forward scattering behavior of the object, and are therefore called forward scattering functions. The other two scattering functions, $\underline{\widehat{\mathbf{H}}}^{+-}$ and $\underline{\widehat{\mathbf{H}}}^{-+}$, are appropriately called backward scattering functions.

In summary, we can find the scattering function of a single object by analytically or numerically solving the problem of a unit-amplitude incident plane wave, $\exp(i\mathbf{k}_i\cdot\mathbf{r})$, scattering from this object. Formula $(A23)$ or $(A27)$ then determines the scattering function in terms of the far-field behavior or the two-dimensional spectrum of the scattered wave fields. Repeating this procedure for the whole set of $\mathbf{k}_i$'s will result in a complete description of $\underline{\widehat{\mathbf{H}}}(\mathbf{k}_s, \mathbf{k}_i)$ for real vectors $\mathbf{k}_s$, $\mathbf{k}_i$, which can then be resolved

into four scattering functions $\widehat{\underline{\mathbf{H}}}^{\pm\pm}$.

Thus far we have assumed that both $\mathbf{k}_i$ and $\mathbf{k}_s$ were real in deriving the result for $\widehat{\underline{\mathbf{H}}}$. This implies that $0 \leq K_{s,i} \leq k$, i.e., both k_{sz} and k_{iz} are purely real. However, we often need $\widehat{\underline{\mathbf{H}}}$ for all real values of K_s and K_i to compute the scattered waves in a general problem where evanescent waves are involved. In the following we will show that the relationship $(A23)$ between the scattering function and the far-field behavior of the scattered wave is still valid for all real values of $\mathbf{K}_{s,i}$

Define the Scattering Function for Complex Propagation Vector $\mathbf{k}_s$

When only K_s exceeds k, it can be shown that the derivation from $(A12)$–$(A16)$, and hence the results, do not change provided that we use $k_{sz} = \pm ik[(K_s/k)^2 - 1]^{1/2} \equiv ih$, where h is real. This can be seen as an analytic continuation in the complex k_{sz} plane from the point $k_{sz} = h$ to the point $k_{sz} = ih$ along the path $h\exp(i\theta)$ where θ runs from 0 to $\pi/2$. This is possible because, as previously discussed, the scattering function is analytic in k_{sz} except at the branch point $k_{sz} = 0$. The path of analytic continuation must not pass through the branch point or the branch cut. This branch cut, which is implicitly constrained by the definition of $g(K)$ in $(A5)$, can be chosen to lie either in the second or the fourth quadrant only.

Define the Scattering Function for Complex Propagation Vector $\mathbf{k}_i$

However, the technique of analytic continuation is not obvious in the case where $k_z(K_i)$ becomes purely imaginary since the $\mathbf{k}''$ integration in $(A12)$ may not collapse $\widehat{\underline{\mathbf{H}}}(\mathbf{k}', \mathbf{k}'')$ into $\widehat{\underline{\mathbf{H}}}(\mathbf{k}', \mathbf{k}_i)$. The main difficulty is that analytic continuation on the variable k_{iz} in $(A21)$ fails since the delta function is singular. The delta function is not strictly a function, and any operation on it must be properly carried out on a sequence of functions that approach it in the limit. The choice of this sequence is arbitrary.

The following sequence and its inverse Fourier transform suffice for our purposes:

$$\begin{aligned} \widehat{\psi}_\tau(k_z; k_{iz}) &= 2\pi\tau^{-1}\exp\{-\pi\tau^{-2}(k_z - k_{iz})^2\} \\ \psi_\tau(z; k_{iz}) &= \exp(-\tau^2 z^2/4\pi)\exp(ik_{iz}z) \end{aligned} \qquad \tau \text{ real, nonzero} \qquad (A31)$$

since in the limit $\tau \longrightarrow 0$ we have

$$\psi_\tau \longrightarrow \exp(ik_{iz}z), \quad \widehat{\psi}_\tau \longrightarrow 2\pi\delta(k_z - k_{iz}). \qquad (A32)$$

Note that both sequences are analytic in k_{iz} for $\tau \neq 0$. Thus they can be analytically continued from the real axis to the imaginary axis in the complex k_{iz} plane:

$$\begin{aligned} \psi_\tau(z; k_{iz} = i\epsilon_i h) &= \exp(-\tau^2 z^2/4\pi)\exp(-\epsilon_i h z) \\ \widehat{\psi}_\tau(k_z; k_{iz} = i\epsilon_i h) &= 2\pi\tau^{-1}\exp\{-\pi\tau^{-2}(k_z - i\epsilon_i h)^2\} \end{aligned} \qquad (A33)$$

where $\epsilon_i = \pm 1$ and $h = k|g(K_i)|$. Thus the incident wave in ($A20$, $A21$) can be approximated by the sequence

$$\mathbf{E}_{i,\tau}(\mathbf{r}) = \exp(i\mathbf{K}\cdot\rho)\,\psi_\tau(z;k_{iz}) \tag{A34}$$

$$\widehat{\mathbf{E}}_{i,\tau}(\mathbf{k}'') = (2\pi)^2\delta(\mathbf{K}''-\mathbf{K}_i)\,\widehat{\psi}_\tau(k_z'';k_{iz}) \tag{A35}$$

where k_{iz} assumes a purely imaginary value $i\epsilon_i h$.

Substituting ($A35$) into ($A13$) and performing the $\mathbf{k}''$ integration we obtain a sequence of scattered wave fields (cf. ($A14$)):

$$\begin{aligned}\mathbf{E}_{s,\tau}(\mathbf{r}) &= \frac{ik}{2}\iiint_V d\mathbf{r}'\iint\frac{d\mathbf{K}}{(2\pi)^2}\iiint\frac{d\mathbf{k}'}{(2\pi)^3}\\ &\quad\times\int_{-\infty}^{\infty}dk_z''\,\underline{\kappa}(\mathbf{K})\cdot\underline{\widehat{\mathbf{H}}}(\mathbf{k}',\mathbf{K}_i,k_z'')\cdot\mathbf{a}_i\,\tau^{-1}\exp\{-\pi\tau^{-2}(k_z''-i\epsilon_i h)^2\}\\ &\quad\times[g(K)]^{-1}\exp\{i(\mathbf{k}'\pm\mathbf{k}(\mathbf{K}))\cdot\mathbf{r}'\}\exp\{\mp i\mathbf{k}(\mathbf{K})\cdot\mathbf{r}\}.\end{aligned} \tag{A36}$$

The k_z'' integration can be evaluated by the method of steepest descent if $\underline{\widehat{\mathbf{H}}}$ is assumed to be analytic over the real and the imaginary axes of the complex k_z'' plane. The real k_z'' path of integration can be deformed into a path (C) which is essentially the same as the old path except for a portion near the origin where it is deformed to pass through the saddle point $i\epsilon_i h$. Most of the contribution to the k_z'' integral then comes from the neighborhood of this saddle point. In the limit of infinitesimal τ, $\tau^{-1}\exp\{-\pi\tau^{-2}(k_z''-i\epsilon_i h)^2\}$ becomes $\delta(k_z''-i\epsilon_i h)$ and $\mathbf{E}_{s,\tau}(\mathbf{r})$ approaches $\mathbf{E}_s(\mathbf{r})$ as given in ($A14$). If we repeat the calculations that follow Eq. ($A14$), we will obtain the same result listed in ($A23$).

Note that Eq. ($A34$) with $\tau = 0$ represents an incident wave that attenuates along the $\epsilon_i z$ direction but grows unbounded in the reverse direction. Such a wave does not possess a Fourier transform; however, $\mathbf{E}_{i,\tau}(\mathbf{r})$ with a nonvanishing τ does have a Fourier transform.

The analyticity of $\underline{\widehat{\mathbf{H}}}$ in the variable $\mathbf{K}_i$ can be inferred directly from the reciprocity principle:

$$\underline{\widehat{\mathbf{H}}}(\mathbf{k}(\mathbf{K}_s),\mathbf{k}(\mathbf{K}_i)) = \underline{\widehat{\mathbf{H}}}(-\mathbf{k}(\mathbf{K}_i),-\mathbf{k}(\mathbf{K}_s)). \tag{A37}$$

Consequently, the scattering function has the same behavior in both variables $\mathbf{K}_s$ and $\mathbf{K}_i$. It is generally analytic in $\mathbf{K}_{s,i}$ except on the circle $|\mathbf{K}_{s,i}| = k$. It can be analytically continued from purely real values of $k_{sz,iz}$ into purely imaginary values $k_{sz,iz} = \pm i(k^2 - K_{s,i}^2)^{1/2}$ where the choice of sign is dictated by the attenuation direction of each wave.

In the following we will study the general scattering function for two-dimensional problems and consider specific scatterers such as cylinders or perfect conducting planes. Some notations to be used are $\mathbf{r} = \mathbf{a}_x x + \mathbf{a}_z z = (r,\theta)$ where θ is the polar angle with respect to the z axis, and $\mathbf{k} = \mathbf{a}_x k_x + \mathbf{a}_z k_z = (k,\theta)$.

Determine the Scattering Function in Two Dimensions

Without loss of generality, we will show the procedure to obtain the scattering function $\underline{\widehat{\mathbf{H}}}(\mathbf{k}(k_{sx}), \mathbf{k}(k_{ix}))$ for all real values of k_{sx} and k_{ix} for an object located at the origin in two dimensions.

Let us assume that the problem of a unit-amplitude incident plane wave with real $\mathbf{k}_i$ scattering from this object can be solved analytically or numerically by some method such as the method of moments. Let us further assume that the solution for the scattered waves outside this two-dimensional scatterer can be written as a linear superposition of outgoing waves of the form

$$\mathbf{E}_s(\mathbf{r}) = \sum_{n=-\infty}^{\infty} \left[\mathbf{a}_x a_n + \mathbf{a}_z b_n\right] H_n^{(1)}(kr) \exp(in\alpha). \qquad (A38)$$

Here, a_n and b_n are the amplitudes of the nth normal mode, $H_n^{(1)}$ is the Hankel function of the first kind of order n, and $\alpha \equiv \theta_s - \theta_i$ is the angle of $\mathbf{k}_s$ with respect to $\mathbf{k}_i$ and is given by

$$\alpha = \pm \cos^{-1}(\mathbf{k}_s \cdot \mathbf{k}_i / k^2) \qquad (A39)$$

with the correct sign prescribed by $\alpha = \sin^{-1}(\mathbf{k}_s \times \mathbf{k}_i / k^2)$. The scattering function can be immediately inferred from relations ($A23$, $A38$) with the help of the asymptotic form of the Hankel function for large r as

$$\underline{\kappa}(k_{sx}) \cdot \underline{\widehat{\mathbf{H}}}(\mathbf{k}(k_{sx}), \mathbf{k}(k_{ix})) \cdot \mathbf{a}_i = \frac{4}{ik^2} \sum_{n=-\infty}^{\infty} \left[\mathbf{a}_x a_n + \mathbf{a}_z b_n\right] (-i)^n \exp(in\alpha), \qquad (A40)$$

where $-k \leq k_{sx,ix} \leq k$.

To derive $\underline{\widehat{\mathbf{H}}}$ for all real values of k_{sx} and k_{ix} we need to analytically continue the right-hand side of ($A40$) from the real axis to the imaginary axis of the complex k_{sz} and k_{iz} planes along a path in the first and the third quadrants. The angle α will become complex,

$$\alpha \equiv \alpha_r + i\alpha_i, \quad \alpha_r \text{ and } \alpha_i \text{ real}, \qquad (A41)$$

and the constants a_n, b_n, if dependent on $k_{sz}(k_{sx})$ and $k_{iz}(k_{ix})$, are assumed to be analytic in these variables so that they can be analytically continued. The complete expression for $\underline{\widehat{\mathbf{H}}}$ can be written formally as follows:

$$\begin{aligned} &\underline{\kappa}(k_{sx}) \cdot \underline{\widehat{\mathbf{H}}}(k_{sx}, k_{sz}(k_{sx}), k_{ix}, k_{iz}(k_{ix})) \cdot \mathbf{a}_i = \\ &\frac{4}{ik^2} \sum_{n=-\infty}^{\infty} \left[\mathbf{a}_x a_n(k_{sx}, k_{sz}(k_{sx}), k_{ix}, k_{iz}(k_{ix})) + \mathbf{a}_z b_n(k_{sx}, k_{sz}(k_{sx}), k_{ix}, k_{iz}(k_{ix}))\right] \\ &\times (-i)^n \exp(-n\alpha_i) \exp(in\alpha_r), \quad -\infty < k_{sx,ix} < \infty \qquad (A42) \end{aligned}$$

Our goal is to determine α_r and α_i for the case where either one or both of k_{sz}, k_{iz} are purely imaginary of the form $k_{sz} = i\epsilon_s|k_{sz}|$, $k_{iz} = \epsilon_i|k_{iz}|$ with the sign $\epsilon_{s,i} = \pm 1$ refers to the direction of attenuation along the $\pm z$ axis. In general, we can derive α_r and α_i from

$$\cos\alpha = k^{-2}\mathbf{k}_s\cdot\mathbf{k}_i \equiv \xi + i\eta, \quad \xi \text{ and } \eta \text{ real}, \tag{A43}$$

by making use of the identity

$$\cos^{-1}(\xi \pm i\eta) = \pm\Big\{ cos^{-1}s - i\ln(t + \sqrt{t^2-1})\Big\} \tag{A44}$$

where

$$s = \tfrac{1}{2}\sqrt{(\xi+1)^2+\eta^2} - \tfrac{1}{2}\sqrt{(\xi-1)^2+\eta^2}, \tag{A45}$$

$$t = \tfrac{1}{2}\sqrt{(\xi+1)^2+\eta^2} + \tfrac{1}{2}\sqrt{(\xi-1)^2+\eta^2}. \tag{A46}$$

(i) Compute α When Only k_{iz} Is Purely Imaginary

In this case we find

$$(\xi \pm 1)^2 + \eta^2 = (k_{ix} \pm k_{sx})^2/k^2, \tag{A47}$$

$$s = \cos\Big\{\pm\Big[\theta_s - \mathrm{sgn}(k_{sx})\pi/2\Big]\Big\}, \tag{A48}$$

$$t = |k_{ix}/k|, \tag{A49}$$

where $\mathrm{sgn}(x)$ is the sign of x. Thus,

$$\alpha_r = \cos^{-1}s = \theta_s - \mathrm{sgn}(k_{ix})\pi/2, \tag{A50}$$

$$\alpha_i = \pm\ln\frac{|k_{ix}| + \sqrt{k_{ix}^2 - k^2}}{k}. \tag{A51}$$

Here, the plus sign in $(A48)$ was chosen since it gives the correct interpretation of α_r as the angle between the real directions of propagation of the incident and scattered waves. The sign of α_i will be determined on the individual case basis for each normal mode n of the scattering function based on whether the mode is growing or is damped as $|k_{iz}|$ increases. Since $\widehat{\underline{\mathbf{H}}}(k_{sx}, k_{sz}, k_{ix}, i\epsilon_i|k_{iz}|)$ was defined with the signs $\epsilon_i = \pm 1$ denoting the $\pm z$ direction of attenuation, the four scattering functions are always damped. Taking into account the sign of the normal mode number n, we obtain the following results in connection with $(A42)$:

$$\begin{aligned} \alpha_r &= \mathrm{sgn}(k_{sx})\pi/2 - \theta_i, \\ \exp(in\alpha_i) &= \left(\frac{k}{|k_{ix}| + \sqrt{k_{ix}^2 - k^2}}\right)^{|n|}, \\ a_0 &= 0 = b_0. \end{aligned} \tag{A52}$$

Note that the sign of η in $(A43)$, which is related to the $\epsilon_{s,i}z$ direction of attenuation of the incident or scattered waves, does not play a role in determining a unique solution for α_i. (This is also true if we use $\sin\alpha$.) Had we used the formula

$$\alpha = \tan^{-1}\left[\frac{\mathbf{k}_i \times \mathbf{k}_s}{\mathbf{k}_i \cdot \mathbf{k}_s}\right] = \tan^{-1}\left[\frac{-k_{ix}k_{sz} + i\epsilon_i k_{sx}\sqrt{k_{ix}^2 - k^2}}{k_{ix}k_{sx} + i\epsilon_i k_{sz}\sqrt{k_{ix}^2 - k^2}}\right], \qquad (A53)$$

we would have obtained the result

$$\alpha_i = i \ln \frac{|k_{ix} - \epsilon_i\sqrt{k_{ix}^2 - k^2}|}{k^2}, \qquad (A54)$$

and the natural choice of the solution would have been

$$\exp(in\alpha_i) = \left(\frac{k}{|k_{ix} + \epsilon_i\sqrt{k_{ix}^2 - k^2}|}\right)^{|n|}, \quad -k \le k_{sx} \le k. \qquad (A55)$$

This solution has great appeal since it depends on the direction of attenuation (ϵ_i) and appears to be unique for each normal mode n. However, it must be discarded because of its unbounded growth in one direction along the k_{ix} axis. This peculiar behavior results from the fact that $\tan\alpha$, as a function of k_{ix} at a fixed value of $k_{sx} = 0$, has two real singularities, $k_{ix} = \pm k$ as seen from equation $(A53)$. Since the solution α can take on different character on different sides of the singularities, it is impropriate to use formula $(A53)$ to derive α_i.

(ii) Compute α When Only k_{sz} Is Purely Imaginary

In this case we obtain the same results as listed in $(A47\text{–}A51)$ except that the subscripts i, s are exchanged. The results are

$$\begin{aligned} \alpha_r &= \theta_s - \mathrm{sgn}(k_{ix})\pi/2, \\ \exp(in\alpha_i) &= \left(\frac{k}{|k_{sx}| + \sqrt{k_{sx}^2 - k^2}}\right)^{|n|}, \\ a_0 &= 0 = b_0. \end{aligned} \qquad (A56)$$

(iii) Compute α When Both k_{ix} And k_{sx} Are Purely Imaginary

In this case we have

$$
\begin{aligned}
|\xi \pm 1| &= \operatorname{sgn}(k_{sx}k_{ix})(\xi \pm 1), && (A57)\\
s &= \operatorname{sgn}(k_{sx}k_{ix}), && (A58)\\
t &= \operatorname{sgn}(k_{sx}k_{ix})\left(\frac{k_{sx}k_{ix} \pm \sqrt{k_{sx}^2 - k^2}\sqrt{k_{ix}^2 - k^2}}{k^2}\right). && (A59)
\end{aligned}
$$

After some algebra we obtain

$$
\begin{aligned}
\alpha_r &= \operatorname{sgn}(k_{sx})\pi/2 - \operatorname{sgn}(k_{ix})\pi/2,\\
\exp(in\alpha_i) &= \left(\frac{k}{|k_{ix}| + \sqrt{k_{ix}^2 - k^2}}\right)^{|n|}\left(\frac{k}{|k_{sx}| + \sqrt{k_{sx}^2 - k^2}}\right)^{|n|}, && (A60)\\
a_0 &= 0 = b_0.
\end{aligned}
$$

In the following we will apply the above results to an infinite cylinder, an infinite conducting plane, and an infinite conducting surface.

Scattering Function of an Infinite Cylinder

An infinitely long cylinder of radius a and refractive index m is assumed to lie along the y axis. The incident propagation vector $\mathbf{k}_i$ is assumed to be normal to the cylinder axis ($k_{iy} = 0$). We will consider two cases of polarization separately and make use of the results given in Chapter 8 of Bohren et al.

(i) Axial Polarization: For incident waves polarized along the cylinder axis we have the following results:

$$
\begin{aligned}
\mathbf{E}_{i\|}(\mathbf{r}) &= \mathbf{a}_y E_i \exp(i\mathbf{k}_i\cdot\mathbf{r}) = \mathbf{a}_y E_i \exp(ikr\cos\alpha), && (A61)\\
\mathbf{E}_{s\|}(\mathbf{r}) &\sim \mathbf{a}_y E_i\sqrt{\frac{2}{\pi kr}}\ \exp\{i(kr - 3\pi/4)\}\sum_{n=-\infty}^{\infty} c_n \exp(in\alpha), \quad r \to \infty, && (A62)\\
c_n &= c_{-n} = \frac{J_n(mka)J_n'(ka) - mJ_n'(mka)J_n(ka)}{J_n(mka)H_n^{(1)\prime}(ka) - mJ_n'(mka)H_n^{(1)}(ka)}, \quad n \geq 0, && (A63)
\end{aligned}
$$

where $\alpha = \theta_s - \theta_i$ is the angle of $\mathbf{k}_s$ from $\mathbf{k}_i$, J_n is the Bessel function of order n, and H_n is the Hankel function of the first kind of order n. Since the scattering function is produced by a unit-amplitude incident plane wave, we set E_i to unity and identify

$$
\underline{\boldsymbol{\kappa}}(k_{sx})\cdot\widehat{\mathbf{H}}(\mathbf{k}_s, \mathbf{k}_i)\cdot\mathbf{a}_y = \mathbf{a}_y\ H_{\|}(\mathbf{k}_s, \mathbf{k}_i). \qquad (A64)
$$

where, for real values of k_{iz} and k_{sz},

$$H_{\|}(\mathbf{k}_s, \mathbf{k}_i) = 4ik^{-2} \sum_{n=-\infty}^{\infty} c_n \exp(in\alpha) = 4ic_0k^{-2} + 8ik^{-2} \sum_{n=1}^{\infty} c_n \cos(n\alpha). \quad (A65)$$

Since c_n does not depend on k_{sz} or k_{iz}, we can analytically continue only α to imaginary values of k_{sz} or k_{iz} and set c_0 to zero to obtain

$$H_{\|}(\mathbf{k}_s, \mathbf{k}_i) = 8ik^{-2} \sum_{n=1}^{\infty} c_n \exp(in\alpha_i) \cos(in\alpha_r) \quad (A66)$$

where α_r and $\exp(in\alpha_i)$ are given by $(A52)$ if only k_{iz} is purely imaginary, $(A56)$ if only k_{sz} is purely imaginary, or $(A60)$ if both k_{iz} and k_{sz} are purely imaginary.

(ii) Transverse Polarization: The incident wave is assumed to be polarized perpendicular to the cylinder axis,

$$\mathbf{E}_{i\perp}(\mathbf{r}) = \mathbf{a}_i E_i \exp(i\mathbf{k}_i \cdot \mathbf{r}) = \mathbf{a}_i E_i \exp(ikr\cos\alpha), \quad (A67)$$

where $\mathbf{a}_i = \mathbf{a}_y \times \mathbf{k}_i/k = \mathbf{a}_{\theta_i}$ is a unit vector pointing in the direction of increasing θ_i. The results are summarized as follows:

$$\mathbf{E}_{s\perp}(\mathbf{r}) \sim \mathbf{a}_\theta E_i \sqrt{\frac{2}{\pi kr}} \exp\{i(kr - \pi/4)\} \sum_{n=-\infty}^{\infty} d_n \exp(in\alpha), \quad r \to \infty \quad (A68)$$

$$d_n = d_{-n} = \frac{mJ_n(mka)J_n'(ka) - J_n'(mka)J_n(ka)}{mJ_n(mka)H_n^{(1)\prime}(ka) - J_n'(mka)H_n^{(1)}(ka)}, \quad n \geq 0 \quad (A69)$$

$$\underline{\kappa}(k_{sx}) \cdot \underline{\widehat{\mathbf{H}}}(\mathbf{k}(k_{sx}), \mathbf{k}(k_{ix})) \cdot \mathbf{a}_i(\mathbf{k}(k_{ix})) = \mathbf{a}_s(\mathbf{k}(k_{sx}))\, H_\perp(\mathbf{k}(k_{sx}), \mathbf{k}(k_{ix})) \quad (A70)$$

$$\mathbf{a}_i(\mathbf{k}(k_{ix})) = \mathbf{a}_y \times \mathbf{k}(k_{ix})/k \quad (A71)$$

$$\mathbf{a}_s(\mathbf{k}(k_{sx})) = \mathbf{a}_y \times \mathbf{k}(k_{sx})/k \quad (A72)$$

where $H_\perp$ is given by the same expressions as $(A65, A66)$ with c_n replaced by d_n.

Note that the unit vector $\mathbf{a}_i$ or $\mathbf{a}_\theta$ in $(A67, A68)$ characterizes the direction of the total incident or scattered wave at a point $\mathbf{r}$. However, the unit vector $\mathbf{a}_i(\mathbf{k}(k_{ix}))$ or $\mathbf{a}_s(\mathbf{k}(k_{sx}))$ in $(A70)$ is the direction of each Fourier component of the incident or scattered wave. These vectors depend strictly on the propagation vector of each Fourier component and are defined by equations $(A71, A72)$ for real- or complex-valued vectors $\mathbf{k}_{i,s}$. When $|k_{sx,ix}| > k$, the unit vectors become complex and the corresponding evanescent Fourier components become elliptically polarized.

It is important to point out that the cylinder is azimuthally (θ) symmetric and thus the scattering function $\underline{\widehat{\mathbf{H}}}$ is expected to be even in k_{sx} for the case $\mathbf{k}_i = \pm\mathbf{a}_z k$. Our above results are consistent with this expectation and confirm that the solution unbounded in one direction of k_{sx} derived from $\tan\alpha$ is incorrect.

Scattering Function of an Infinite Conducting Plane

Consider a horizontal, infinite conducting plane located at the origin with its normal directed along the z direction. The incident wave is assumed to be propagating from above the surface. Since the tangential component of the total wave field must vanish on the conducting surface, we can obtain the following solution:

$$\mathbf{E}_i(\mathbf{r}) = \mathbf{a}_i E_i \exp(i\mathbf{k}_i\cdot\mathbf{r}) = \mathbf{a}_i E_i \exp\{i(\mathbf{K}_i\cdot\boldsymbol{\rho} + k_{iz}z)\} \tag{A73}$$

$$\mathbf{E}_s(\mathbf{r}) = \begin{cases} (-\mathbf{a}_\rho\mathbf{a}_\rho + \mathbf{a}_z\mathbf{a}_z)\cdot\mathbf{a}_i E_i \exp\{i(\mathbf{K}_i\cdot\boldsymbol{\rho} - k_{iz}z)\} & \text{above surface} \\ -\mathbf{E}_i(\mathbf{r}) & \text{below surface} \end{cases} \tag{A74}$$

(Recall that the scattered wave is defined as $\mathbf{E}_s \equiv \mathbf{E}_{total} - \mathbf{E}_i$.) Thus the total wave below the surface is identically zero as expected. Note that the above solution is valid in both two and three dimensions.

The scattering function can be immediately found by taking the two-dimensional Fourier transform of the above equations and setting E_i to unity. The two backward scattering functions are defined by the solution above the surface as

$$\underline{\boldsymbol{\kappa}}^+\cdot\underline{\widehat{\mathbf{H}}}^{+-}(\mathbf{K}_s,\mathbf{K}_i) = \underline{\boldsymbol{\kappa}}^-\cdot\underline{\widehat{\mathbf{H}}}^{-+}(\mathbf{K}_s,\mathbf{K}_i) = -\frac{8\pi^2 g(K_s)}{ik}\delta(\mathbf{K}_s - \mathbf{K}_i)(\underline{\mathbf{I}} - 2\mathbf{a}_z\mathbf{a}_z), \tag{A75}$$

while the two forward scattering functions are determined by the solution below the surface:

$$\underline{\boldsymbol{\kappa}}^+\cdot\underline{\widehat{\mathbf{H}}}^{++}(\mathbf{K}_s,\mathbf{K}_i) = \underline{\boldsymbol{\kappa}}^-\cdot\underline{\widehat{\mathbf{H}}}^{--}(\mathbf{K}_s,\mathbf{K}_i) = -\frac{8\pi^2 g(K_s)}{ik}\delta(\mathbf{K}_s - \mathbf{K}_i)\underline{\mathbf{I}}. \tag{A76}$$

Scattering Function of an Infinite Conducting Surface

For simplicity let us confine ourselves to the case where the surface height varies only in the x direction. Let $z = f(x)$ be the surface height variation about the $z = 0$ reference level. Since electromagnetic waves cannot penetrate a perfectly conducting surface, we assume that the incident wave is propagating toward the surface from above only, hence only the two scattering functions $\underline{\widehat{\mathbf{H}}}^{+-}$ and $\underline{\widehat{\mathbf{H}}}^{--}$ are meaningful.

Consider an arbitrary downgoing incident electromagnetic wave which is linearly polarized parallel to the surface (parallel polarization),

$$\mathbf{E}_{i\|}(\mathbf{r}) = \mathbf{a}_y E_i^-(\mathbf{r}), \tag{A77}$$

or parallel to the plane of incidence (vertical polarization):

$$\begin{aligned} \mathbf{E}_{i\perp}(\mathbf{r}) &= \mathbf{a}_i E_i^-(\mathbf{r}), & (A78)\\ \mathbf{a}_i &= \mathbf{a}_y \times \mathbf{k}_i/k. & (A79) \end{aligned}$$

The complete solution of the scattered waves for this general problem has been given in our recent report [1]. For our purposes it suffices to summarize the results therein as follows.

(i) Horizontal Polarization: The two-dimensional spectra of the upgoing (+) and downcoming (−) traveling scattered waves are given by

$$\begin{aligned} \widehat{E}_{sy}^+(k_{sx}) &= -\frac{1}{2}\int J_y(x')\frac{\exp\{-ikg(k_{sx})f(x')\}}{g(k_{sx})}\exp(-ik_{sx}x')dx', & (A80)\\ \widehat{E}_{sy}^-(k_{sx}) &= -\widehat{E}_{iy}(k_{sx}), & (A81) \end{aligned}$$

where $J_y(x)$ is the effective surface current satisfying the integral equation

$$\widehat{E}_{iy}^-(k_x) = \frac{1}{2}\int J_y(x')\frac{\exp\{ikg(k_x)f(x')\}}{g(k_x)}\exp(-ik_x x')dx'. \tag{A82}$$

By choosing a unit amplitude incident plane wave, $E_i(\mathbf{r}) = \exp(i\mathbf{k}_i\cdot\mathbf{r})$, we can identify the two scattering functions

$$\begin{aligned} \underline{\kappa}^+(k_{sx})\cdot\underline{\widehat{\mathbf{H}}}^{+-}(k_{sx},k_{ix})\cdot\mathbf{a}_y &= \mathbf{a}_y H_\|^{++}(k_{sx},k_{ix}), & (A83)\\ \underline{\kappa}^-(k_{sx})\cdot\underline{\widehat{\mathbf{H}}}^{--}(k_{sx},k_{ix})\cdot\mathbf{a}_y &= \mathbf{a}_y H_\|^{--}(k_{sx},k_{ix}), & (A84) \end{aligned}$$

where

$$\begin{aligned} H_\|^{++}(k_{sx},k_{ix}) &= \frac{2g(k_{sx})}{ik}\widehat{E}_{sy}^+(k_{sx}), & (A85)\\ H_\|^{--}(k_{sx},k_{ix}) &= \frac{2g(k_{sx})}{ik}\widehat{E}_{sy}^-(k_{sx}) = -\frac{4\pi^2 g(k_{sx})}{ik}\delta(k_{sx}-k_{ix}). & (A86) \end{aligned}$$

(ii) Vertical Polarization: The results can be summarized in our notation as follows:

$$\begin{aligned} \widehat{\mathbf{E}}_{i,s}(k_{ix,sx}) &= \mathbf{a}_{i,s}(k_{ix,sx})\widehat{E}_{i,s}(k_{ix,sx}) & (A87)\\ \mathbf{a}_{i,s}(k_{ix,sx}) &= \mathbf{a}_y \times \mathbf{k}_{i,s}(k_{ix,sx})/k & (A88) \end{aligned}$$

where

$$\widehat{E}_s^+(k_{sx}) = -\frac{1}{2}\int J_x(x')\left[g(k_{sx}) - \frac{k_{sx}}{k}\frac{df(x')}{dx'}\right] \times \frac{\exp\{-ikg(k_{sx})f(x') - ik_{sx}x'\}}{g(k_{sx})}dx', \quad (A89)$$

$$\widehat{E}_s^-(k_{sx}) = -\widehat{E}_i^-(k_{sx}), \quad (A90)$$

$$\widehat{E}_i^-(k_{ix}) = \frac{1}{2}\int J_x(x')\left[g(k_{ix}) + \frac{k_{ix}}{k}\frac{df(x')}{dx'}\right]\frac{\exp\{ikg(k_{ix})f(x') - ik_{ix}x'\}}{g(k_{ix})}dx'. \quad (A91)$$

Thus we can infer the scattering function for this case as

$$\underline{\kappa}^+(k_{sx})\cdot\underline{\widehat{\mathbf{H}}}^{+-}(k_{sx},k_{ix})\cdot\mathbf{a}_i(k_{ix}) = \mathbf{a}_s(k_{sx})H_\perp^{++}(k_{sx},k_{ix}), \quad (A92)$$

$$\underline{\kappa}^-(k_{sx})\cdot\underline{\widehat{\mathbf{H}}}^{--}(k_{sx},k_{ix})\cdot\mathbf{a}_i(k_{ix}) = \mathbf{a}_i(k_{sx})H_\perp^{--}(k_{sx},k_{ix}), \quad (A93)$$

where

$$H_\perp^{++}(k_{sx},k_{ix}) = \frac{2g(k_{sx})}{ik}\widehat{E}_s^+(k_{sx}), \quad (A94)$$

$$H_\perp^{--}(k_{sx},k_{ix}) = \frac{2g(k_{sx})}{ik}\widehat{E}_s^-(k_{sx}) = -\frac{4\pi g(k_{sx})}{k}\delta(k_{sx}-k_{ix}). \quad (A95)$$

Conclusion

In conclusion, we have derived the expression for the scattering function in terms of the far-field behavior or the two-dimensional spectrum of the scattered waves for a single object located at the origin. This result can generally be analytically continued to imaginary values of the k_z component of the incident and the scattered waves under the assumption that the scattering function is bounded.

References

[1] Charles L. Rino, Thomas L. Crystal, Alan K. Koide, and Hoc D. Ngo. Numerical simulation of acoustic and EM scattering from ocean surfaces. Final Report Project 1010, Vista Research, Inc., 1989.

[2] E. I. Thorsos. The validity of the perturbation approximation for rough surface scattering using a gaussian roughness spectrum. *J. Acoust. Soc. Am.*, 86(1), July 1989.

[3] Roger Dashen, Frank Henyey, and Dan Wurmser. Calculation of acoustic scattering off the ocean surface. Technical Report LJI-88-P-487, Center for Studies of Nonlinear Dynamics, La Jolla Institute, 1989.

[4] Robert J. Urick. *Principles of Underwater Sound.* New York: McGraw-Hill Book Company, 1983. Page 264.

[5] Alan Ellinthorpe, 1989.

[6] Serge Baldy. Bubbles in the close vicinity of breaking waves: Statistical characteristics of the generation and dispersion mechanism. *J. Geophys. Res.*, 93(C7), July 1988.

[7] Blair Kinsman. *Wind Waves: Their Generation and Propagation on the Ocean Surface.* New York: Dover Publications, Inc., 1984.

[8] G. B. Crawford and D. M. Farmer. On the spatial distribution of ocean bubbles. *J. Geophys. Res.*, 92(C8), July 1987.

[9] Phillip M. Morse and Herman Feshback. *Methods of Theoretical Physics–Part II.* New York: McGraw-Hill Book Company, Inc., 1953. Pages 1498-1501.

[10] C. L. Rino, H. D. Ngo, and K. A. Haycock. A spectral-domain method for multiple scattering in discrete random media. *IEEE Trans. on Ant. and Prop.*, 1989. Accepted for publication.

[11] V. Twersky. Multiple scattering of waves and optical phenomena. *J. Opt. Soc. Am.*, 52(2):145–171, 1962.

[12] P. A. Bobbert and J. Vlieger. Light scattering by a sphere on a substrate. *Physica*, 137(A):209–242, 1986.

[13] R. H. Lang. Electromagnetic backscattering from a sparse distribution of lossy dielectric scatterers. *Radio Science*, 16(1):15–30, 1981.

[14] Craig F. Bohren and Donald R. Huffman. *Absorption and Scattering of Light by Small Particles*. New York: John Wiley & Sons, 1983.